[American Journal of Science, Vol. 319, December, 2019, P. 846-902, DOI 10.2475/10.2019.02]

DILUTION AND PROPAGATION OF PROVENANCE TRENDS IN SAND AND MUD: GEOCHEMISTRY AND DETRITAL ZIRCON GEOCHRONOLOGY OF MODERN SEDIMENT FROM CENTRAL CALIFORNIA (U.S.A.)

MATTHEW A. MALKOWSKI*†, GLENN R. SHARMAN**, SAMUEL A. JOHNSTONE***, MARTIN J. GROVE*, DAVID L. KIMBROUGH§, and STEPHAN A. GRAHAM*

ABSTRACT. Integrated, multi-method provenance studies of siliciclastic sedimentary deposits are increasingly used to reconstruct the history of source-to-sink transport, paleogeography, and tectonics. Invariably, analysis of large-scale depositional systems must confront issues regarding how to best sample the system and adequately cope with the details of sediment mixing. Potential biases including variations in grain size, sediment flux, and mineral concentration may cause provenance tracking tools to misrepresent the contributions of source-areas that contribute to large drainage networks. We have acquired U-Pb detrital zircon data from modern sand and whole-rock geochemistry from mud sampled from the Sacramento-San Joaquin drainage of central California to elucidate conditions that can skew provenance trends along the course of a major river system. This drainage network is fed by headwaters that tap the Mesozoic pluton-dominated southern Sierra Nevada, the Paleozoic-Mesozoic wallrock and volcanic-dominated northern Sierra Nevada, the ultramafic-dominated eastern Klamath Mountains, and the intermediate to mafic Cascades volcanic arc. Analysis of the results indicates that detrital zircon provenance trends effectively record source variations for the southern, granite-dominated portion of the drainage network where contrasts in lithology and inferred zircon fertility are relatively minor. In these circumstances, mixture modeling of U-Pb detrital zircon data calibrated with a measure of zircon fertility approximates relative sediment flux contributed by individual drainages. Alternatively, in the northern parts of the system, source regions underlain by ultramafic and/or volcanic rocks are poorly represented, or entirely missing, in downstream detrital zircon records. In some cases, mud geochemistry data more faithfully represent sediment provenance trends.

Sampling performed at the confluence of the Sacramento, American, Mokelumne, and San Joaquin Rivers within the Sacramento-San Joaquin Delta region yields a detrital zircon age distribution that is indistinguishable from that of an independently established database of Sierra Nevada batholith crystallization ages. However, when the combined river flows along a recently established passage to the Pacific through the San Francisco Bay region, dredged sediment is found to be significantly contaminated by locally eroded material from the Franciscan Complex and other rocks that crop out within the Coast Ranges. Large variation of Zr concentrations measured throughout the Bay area document that significant hydrodynamic fractionation impacts sediment delivery through this segment of the system. The more Sierra Nevada-like detrital zircon age distribution yielded by a piston-core sample from the continental slope may be explained by either early-stage unroofing of the Coast Ranges or more efficient sand delivery from the delta to the Pacific by a free-flowing river driven by a low stand in sea level.

Key words: Central California, detrital zircon, dilution, geochemistry, modern sediment

* Department of Geological Sciences, Stanford University, Stanford California 94305
** Department of Geosciences, University of Arkansas, Fayetteville, Arkansas 72701
*** Geosciences and Environmental Change Science Center, U.S. Geological Survey, Denver, Colorado 80225
§ Department of Geological Sciences, San Diego State University, San Diego, California 92182
† Corresponding author: mamalkow@stanford.edu

INTRODUCTION

Provenance studies have been widely utilized to understand the evolution of orogenic belts and their associated basins (Dickinson, 1970; Bhatia, 1983; Graham and others, 1986; Ross and others, 1992). The ability to trace sediment routing pathways from "source-to-sink" is a first-order goal of such investigations (for example, Somme and others, 2009). The type of provenance information that can be extracted from sediment and/or sedimentary rocks depends on the grain-size of the sediment being studied (for example, cobbles vs. sand vs. mud) and the techniques employed (petrography, geochemistry, detrital geochronology). The extracted information is in turn subject to a range of environmental biases (Garzanti and others, 2009). Classic provenance methods such as conglomerate clast counts (Lawton, 1986; DeCelles, 1988; Horton and others, 2004), sandstone petrography (Graham and others, 1976; Ingersoll, 1978. 1983), and sediment geochemistry (Bhatia, 1983; McLennan and others, 1993; Draut and Clift, 2001; Clift and others, 2005) have all been successfully applied to characterize sedimentary provenance. Over the past 20 years, however, increased efficiency in the measurement of U-Pb detrital zircon age distributions has allowed this approach to outpace all other provenance methods employed (for example, Sircombe and Freeman, 1999; Fedo and others, 2003; Gehrels and Pecha, 2014). Over time, U-Pb measurements of detrital zircon have become increasingly coupled with trace element (Barth and others, 2013), Hf isotopic (Malkowski and Hampton, 2014; Anderson and others, 2016), O isotopic (Iizuka and others, 2013), and/or (U-Th)/He measurements (Reiners and others, 2005; Xu and others, 2017) to enhance interpretations.

Despite these advances, many potentially overlooked factors are capable of biasing the provenance signature of river sediment. This is especially true when all emphasis is placed upon a single, dense accessory mineral like zircon. Known factors include source lithology (and zircon fertility), weathering, sediment flux, and sampling/processing procedures (Moecher and Samson, 2006; Hietpas and others, 2011; Slama and Kosler, 2012; Malusa and others, 2013). Spatially variable exhumation rates throughout drainage networks also play a role (Garver and others, 1999; Bernet and others, 2004; Bernet and Garver, 2005). Despite improved understanding of these factors, considerable uncertainty remains regarding how effectively provenance information is relayed downstream in sediment dispersal systems (Kelley and Whetten, 1969; Whetten and others, 1969; Cawood and others, 2003; Amidon and others, 2005a, 2005b; Hietpas and others, 2011; Andersen and others, 2016).

Studies of modern rivers over the past two decades have provided valuable ground truth regarding the fidelity by which provenance information is transmitted from source-to-sink over time. Simply put, any factor that hinders accurate assessment of sediment provenance from a well-understood modern system is likely to be more problematic for ancient environments for which less is known. The modern sediment provenance of some of the Earth's great river systems has been examined including the Amazon (Mapes, ms, 2009; Mason and others, 2019), Colorado (Kimbrough and others, 2015), Indus (Alizai and others, 2011; Li and others, 2018), Lena (Prokopiev and others, 2008), Mississippi (Craddock and Kylander-Clark, 2013), Nile (Fielding and others, 2016), Yalu-Brahmaputra (Cina and others, 2009; Zhang and others, 2012; Carrapa and others, 2017), and Yangtze (He and others, 2013). The types of insights gained from such studies is well illustrated by a series of investigations carried out with the Frankland River that drains southwestern Australia. Cawood and others (2003) showed how detrital zircon age distributions originating from a cratonal source were systematically diluted as the Frankland River traversed an actively eroding accretionary margin. Building on this work, the Hf isotopic properties of detrital zircons were used to correct for the enhanced contribution of younger sediment from the margin (Dhuime and others, 2011). Further study based upon a comparison of detrital zircon populations between the Amazon and Frankland

Rivers highlighted how both variable erosion rates and zircon fertility influenced detrital zircon populations (Spencer and others, 2018).

As indicated above, there is a clear need to couple measurements of detrital zircon data sets with other observable parameters in well-understood systems to more rigorously assess the significance of the results for sedimentary provenance analysis. In this study, we integrate both detrital zircon geochronology and mud geochemistry to assess spatial variation in sediment provenance signatures in modern fluvial, estuarine, and deltaic environments throughout central California's Great Valley, San Francisco Bay area, and adjacent continental shelf and slope. The *ca.* 800 km long × 150 km wide Great Valley catchment is developed along the tectonically active California margin (fig. 1). The spatially variable lithology throughout the region implies a wide range in zircon concentration and sediment flux throughout the catchment basin. We have integrated detrital zircon (n = 28), shale geochemistry (n = 36), and other data presented in this paper to evaluate how variation in lithology, zircon concentration, sediment flux, tectonics, and a host of other factors bias sediment provenance trends throughout the San Joaquin – Sacramento River system. We employ mixture modelling to explore how effectively these variations can be quantitatively assessed.

BACKGROUND

Bedrock Geology

The bedrock geology surrounding California's Great Valley can be subdivided into three basement domains (fig. 1): (1) tectonic elements of the Jurassic–Cretaceous convergent margin (subduction complex, forearc basin, and magmatic arc) preserved within the Coast Ranges and Sierra Nevada mountain range of east-central California (Dickinson, 1971); (2) the Jurassic and older Klamath Mountain province of northwestern California; and (3) the late Cenozoic Cascades arc of northeastern California.

Central California is dominated by a triad of Jurassic–Eocene convergent margin tectonic elements (Dickinson, 1971) (fig. 1). The Great Valley is bounded to the west by the Franciscan Complex and the Coast Range ophiolite, an informally distinguished unit within the Coast Ranges (Ernst, 1970; Shervais and Kimbrough, 1985). The Franciscan Complex consists of Jurassic–Cretaceous metabasaltic and trench-derived metasedimentary rocks deposited along California's convergent margin (Hamilton, 1969; Dickinson, 1970; Ernst, 1970; McLaughlin and others, 1982, 2000; Dumitru and others, 2015; Wakabayashi, 2015). The Jurassic Coast Range ophiolite structurally overlies the Franciscan Complex and is stratigraphically below the informal Cretaceous Great Valley group, although the details of its origin remain controversial (Dickinson and others, 1996). California's Central Valley is filled by the Great Valley group and younger Cenozoic strata (Ojakangas, 1968; Ingersoll, 1978, 1979, 1982). Along the Great Valley's eastern margin, accreted Paleozoic-Mesozoic wallrocks of the Foothills metamorphic belt (Schweickert and Cowan, 1975) are intruded and/or faulted against plutons of the Sierra Nevada batholith.

The Sierra Nevada batholith (Hamilton, 1969; Bateman, 1992) is a composite batholith produced episodically by Cordilleran subduction-related magmatism from the late Permian through the Neogene (Irwin and Wooden, 1999; Irwin, 2003; Barth and others, 2011). The two most significant episodes of magmatic activity occurred during the Middle to Late Jurassic (175–155 Ma) and again during the middle Cretaceous (125–85 Ma) (Irwin and Wooden, 1999; Walker and others, 2002; Irwin, 2003; Ducea and Barton, 2007; Barton and others, 2011; Chapman and others, 2012; DeCelles and Graham, 2015). The extent of the middle Cretaceous batholith (*ca.* 125–85 Ma) controls the morphology of the modern northwest-southeast-trending Sierra Nevada mountain range. Plutons of this age exhibit west-east gradients in age, mineralogy, and geochemical and isotopic composition (DePaolo, 1981; Chen and Moore, 1982; Bateman, 1992). The western plutons are relatively mafic with elevated

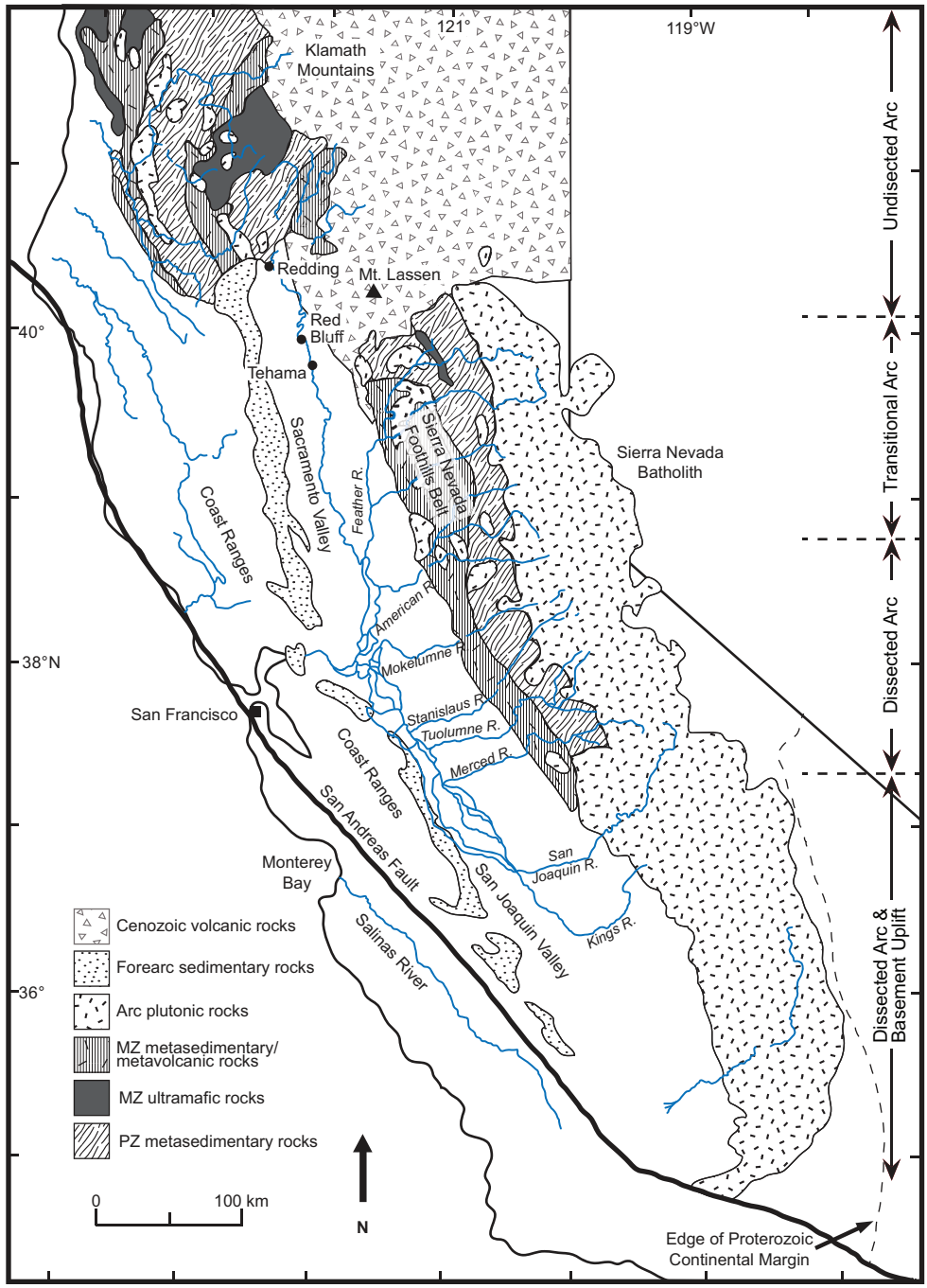

Fig. 1. Generalized geologic map of California showing primary source regions and rock types for Central Valley fluvial systems. Arc-provenance delineations are from Ingersoll and Eastmond (2007).

concentrations of FeO, MgO, and CaO, whereas plutons and volcanic cover in the east are more felsic with elevated concentrations of K_2O, Rb, U, and Th (Dodge and others, 1982; Ague and Brimhall, 1988). This major element zonation is mirrored by system-

atic variation in oxygen, strontium, and neodymium isotopes (Kistler and Peterman, 1973; DePaolo, 1981; Lackey and others, 2008).

The Klamath Mountains region of northern California represents a second basement assemblage tapped by the Great Valley drainage network (Irwin, 1981). The most distinctive feature of the province is the Ordovician Trinity peridotite, an informal name we adopt throughout the text following past work (Quick, 1981; Lindsley-Griffin, 1991) (fig. 1). It occurs as a large ultramafic massif that crops out over a broad region of the eastern Klamath Mountains (Quick, 1981; Lindsley-Griffin, 1991). The peridotite is associated with Neoproterozoic and early Paleozoic intrusions (Wallin and Metcalf, 1998). Tectonic sheets of late Paleozoic and Mesozoic metavolcanic and metasedimentary rocks both structurally underlie and were deposited atop the Trinity peridotite (Irwin, 1981). Collectively, the rocks were sutured to the continental margin and heavily intruded by plutons of the Jurassic magmatic arc (Irwin, 1981; fig. 1). Equivalents of the Paleozoic-Mesozoic volcanic and sedimentary cover overlying the Trinity peridotite in the eastern Klamath Mountains are also represented within the northern Sierra terrane of the Sierra Nevada region (Davis, 1969; Davis and others, 1980; Wright and Fahan, 1988; Wright and Wyld, 1994) (fig. 2). A robust population of 155 to 135 Ma ages in the some of the Great Valley group units reflects Late Jurassic – Early Cretaceous magmatism within the Klamath and northwestern Sierra Nevada region (DeGraaff-Surpless and others, 2002).

Late Cenozoic volcanics of the southern Cascades volcanic arc represent a third important lithology within the study area. The volcanic carapace of the arc covers a vast area of northeastern California between the Klamath Mountains and the northern Sierra Nevada (fig. 1). Volcanic rocks erupted from Mt. Lassen and Mt. Shasta lie within the watershed of the upper Sacramento River. These consist primarily of basalt, basaltic andesite, and andesite erupted over the past 3 Ma (Guffanti and Weaver, 1988; Guffanti, 1990; Hildreth, 2007; Clynne and Muffler, 2010).

Eroded plutonic, volcanic, and metamorphic rocks of the Sierra Nevada and Klamath provinces have been the primary sources of sediment to the Central Valley forearc basin since the Jurassic (Dickinson and Rich, 1972; Dickinson and others, 1979; Ingersoll, 1979, 1983, 2012; DeGraaff-Surpless and others, 2002; Cecil and others, 2010; Sharman and others, 2015). Linn and others (1992) highlighted isotopic and chemical variations in trace elements (for example ε_{Nd}, Th, U, La, Nb, Zr, Hf, Pb, Rb, Ni, and Cr) from upper Mesozoic forearc strata that yielded similar spatial trends observed in plutonic rocks of the Sierra Nevada.

The Great Valley – Sacramento-San Joaquin Delta – San Francisco Bay Drainage Network

Figure 2 shows the geometry of the modern drainage network. Two main rivers, the south-flowing Sacramento and the north-flowing San Joaquin, flow along the axis of the valley. The Sacramento River originates within the Klamath Mountains of northern California while the *ca.* 500 km long San Joaquin flows from the western slopes of the southern Sierra Nevada. The north-flowing San Joaquin River is fed by large tributaries (Kings, Merced, Tuolumne, and Stanislaus Rivers) that extend into the southern Sierra Nevada and drain the densely intruded Sierra Nevada batholith (fig. 2).

The south-flowing, *ca.* 700 km long Sacramento River has its headwaters in Trinity peridotite of the Klamath Mountains and the Mount Shasta area. South of Redding, major tributaries including the Feather River flow westward across accreted Paleozoic and Mesozoic wallrocks and plutonic rocks of the northern Sierra batholith. In similar fashion to the San Joaquin River, drainage networks flowing into the Sacramento River from the topographically lower Coast Ranges are much smaller than those on the eastern side of the northern Great Valley (fig. 2).

The Sacramento, American, Mokelumne, and San Joaquin Rivers all flow into the Sacramento-San Joaquin Delta (fig. 2). The delta is established at the former site of

Fig. 2. Central Valley drainage and sample location map.

Lake Corcoran, a middle Pleistocene lake that covered the central Great Valley and ponded against the Coast Ranges to the west (Frink and Kues, 1954). Since the past *ca.* 600 ka, topographic evolution via northwestward displacement of Coast Range blocks along the San Andreas Fault system has allowed the integrated river/estuarine system

to flow 80 km farther west, across the Coast Ranges and through San Francisco Bay to reach the Pacific Ocean (Sarna-Wojcicki and others, 1985).

METHODS

Following nomenclature of Ingersoll (1990, 2012; Ingersoll and others, 1993), we sampled both first-order (local drainages), second-order (rivers and streams) and third-order (big rivers, deltas, marine environments) depositional systems. River sediment was collected from the main trunks of the San Joaquin River and Sacramento River as well as the major tributaries of each (fig. 2). Note that additional dredge samples were analyzed throughout the greater San Francisco Bay area including the Golden Gate dune field, from the continental shelf, and from a piston core from the continental slope.

We aggregated subsamples collected along profiles oriented normal to the river axis to minimize hydraulic fractionation and grain-size biases of stream and river samples (Lawrence and others, 2011). Sediment was collected from point bar locations by traversing the river in the direction of the thalweg up to *ca.* 1-m water depth. This generally yielded 2 to 8 liters of aggregated sediment. The grain size fractions present in each sample varied significantly. Each bulk sample was divided into two aliquots intended for detrital zircon and sediment major and trace element geochemistry.

Detrital Zircon Analysis

The <500-micron portion of the sand-sized fraction was processed for detrital zircon analysis using standard hydrodynamic, magnetic, and density methods. Detrital zircons were mounted in epoxy, sectioned, and polished. U-Pb age distributions were measured using laser ablation-inductively coupled plasma-mass spectrometry (LA-ICP-MS). Measurements were undertaken at both the University of California, Santa Cruz (UCSC) and the University of Arizona Laserchron Center (ALC). Sharman and others (2013) detail the data reduction methods for results obtained at UCSC. Full data tables and additional details regarding analytical methods are presented in the data supplement (Appendix[1]) that accompanies this paper. The measured U-Pb age distributions are represented graphically by histograms superposed upon relative probability plots constructed using a kernel density estimator (KDE) (see Vermeesch, 2012). We also bin ages in pie charts and bar graphs produced using software described by Sharman and others (2018). We perform the K-S test to compare two samples to one another. We favor the interpretation that samples were derived from distinct distributions when the K-S test produces a p value less than 0.05.

Major and Trace Element Geochemistry

A second fine-grained fraction acquired for most samples was wet sieved using disposable sieve cloth to obtain the <63-micron portion (clay + silt fraction) for major and trace element geochemistry. The fine-grained fraction was rinsed with hydrogen peroxide to remove organic material and oven-dried. X-ray fluorescence (XRF) and ICP-MS samples were prepared from *ca.* 20-gram aliquots of the clay + silt fraction. Measurements were performed at Washington State University following the methods described by Johnson and others (1999) (see also the Appendix and Appendix 2 of the data repository[2]).

Zircon contains up to 45 weight percent Zr and is the main repository of Zr in the crust. An extensive LA-ICP-MS survey of Zr-bearing accessory minerals in common rock types performed by Bea and others (2006) has revealed that tens of parts per million (ppm) to a few thousand ppm of Zr may also reside in xenotime, titanite,

[1] http://earth.geology.yale.edu/%7eajs/SupplementaryData/2019/Malkowski.
[2] http://earth.geology.yale.edu/%7eajs/SupplementaryData/2019/Malkowski.

ilmenite, rutile, allanite, amphibole, clinopyroxene, garnet, magnetite, and other phases. Amidon and others (2005a) have demonstrated that bulk Zr concentration of sediment is a relatively accurate and therefore reliable proxy (±10%) for zircon fertility as long as there are no significant variations in grain size and morphology. Dedicated Zr geochemistry samples were collected from San Francisco Bay and other critical areas. These samples were processed and analyzed following methods described in Barnard and others (2013a). Zirconium concentrations were from the <63 microns split to minimize grain-size variability.

Sediment Mixture Modeling

The detrital zircon U-Pb age distribution of a given siliciclastic river sample is a function of the sources of igneous crystallization ages present within basement and sedimentary strata that crop out throughout the drainage catchment, the zircon concentration (or fertility) of each "source," and the sediment flux contributed by individual tributaries that tap these sources. Sediment mixture modeling and "unmixing" techniques offer promise for reconstructing and predicting relative detrital zircon contributions of sediment sources (Amidon and others, 2005a, 2005b; Fletcher and others, 2007; Cina and others, 2009; Kimbrough and others, 2015; Mason and others, 2017; Sharman and Johnstone, 2017). However, the large number of variables involved in these calculations makes it challenging to extract geologically meaningful interpretations. For example, Amidon and others (2005a, 2005b), Moecher and Samson (2006), and Dickinson (2008) have all highlighted the importance of zircon fertility bias in detrital zircon age populations and proportions. In particular, these workers have noted that a detrital source with a high concentration of zircon can overwhelm other detrital fluxes that may be supplying significant sediment contributions, but are low in zircon abundance.

In this study, we characterize 'offspring' distributions of U-Pb ages from the Sacramento and San Joaquin Rivers and their confluence as a weighted sum of inputs from their immediate upstream reaches and tributaries (the 'parents,' Amidon and others, 2005). We determine the mixing coefficients by minimizing the V_{max} (Saylor and Sundell, 2016) computed between the observed offspring and the mixed 'parents,' under the constraints that the mixing coefficients must each be between 0 and 1 and sum to unity (Amidon and others, 2005). We assess the allowable variability in equally likely mixing coefficients by conducting 10,000 iterations of a random sampling procedure, bootstrapping. For each iteration, we resample with replacement the parent and offspring samples and recompute the minimum V_{max} and associated mixing coefficients. We track the mixing coefficients and modelled mixed offspring for each iteration and highlight agreement between the modeled offspring mixture and observed offspring by recording the intervals that bound 95 percent of the mixed distributions. Further details of the calculations are presented in Appendix 1 at the end of this paper.

RESULTS

U-Pb Detrital Zircon Age Distributions

Figure 3 portrays the first-order variation of detrital zircon age distributions throughout the Great Valley drainage system. In order to provide a simplified framework for discussion that is based on available crystallization age present within northern and central California, we use pie diagrams and bin U-Pb zircon ages as follows: 3500 to 300, 300 to 135, 135 to 100, 100 to 85, 85 to 65, 65 to 23, 23 Ma-present.

3500 to 300 Ma Bin.—The highest abundance of detrital zircons with U-Pb ages in the 3500 to 300 Ma bin are supplied by Paleozoic metasedimentary units in the Klamath Mountains, the Northern Sierra terrane, and the western Foothills belt of the Sierra Nevada (fig. 3). Zircon of this age range is also recycled from Mesozoic sedimentary rocks (DeGraaff-Surpless and others, 2002; Surpless and others, 2006;

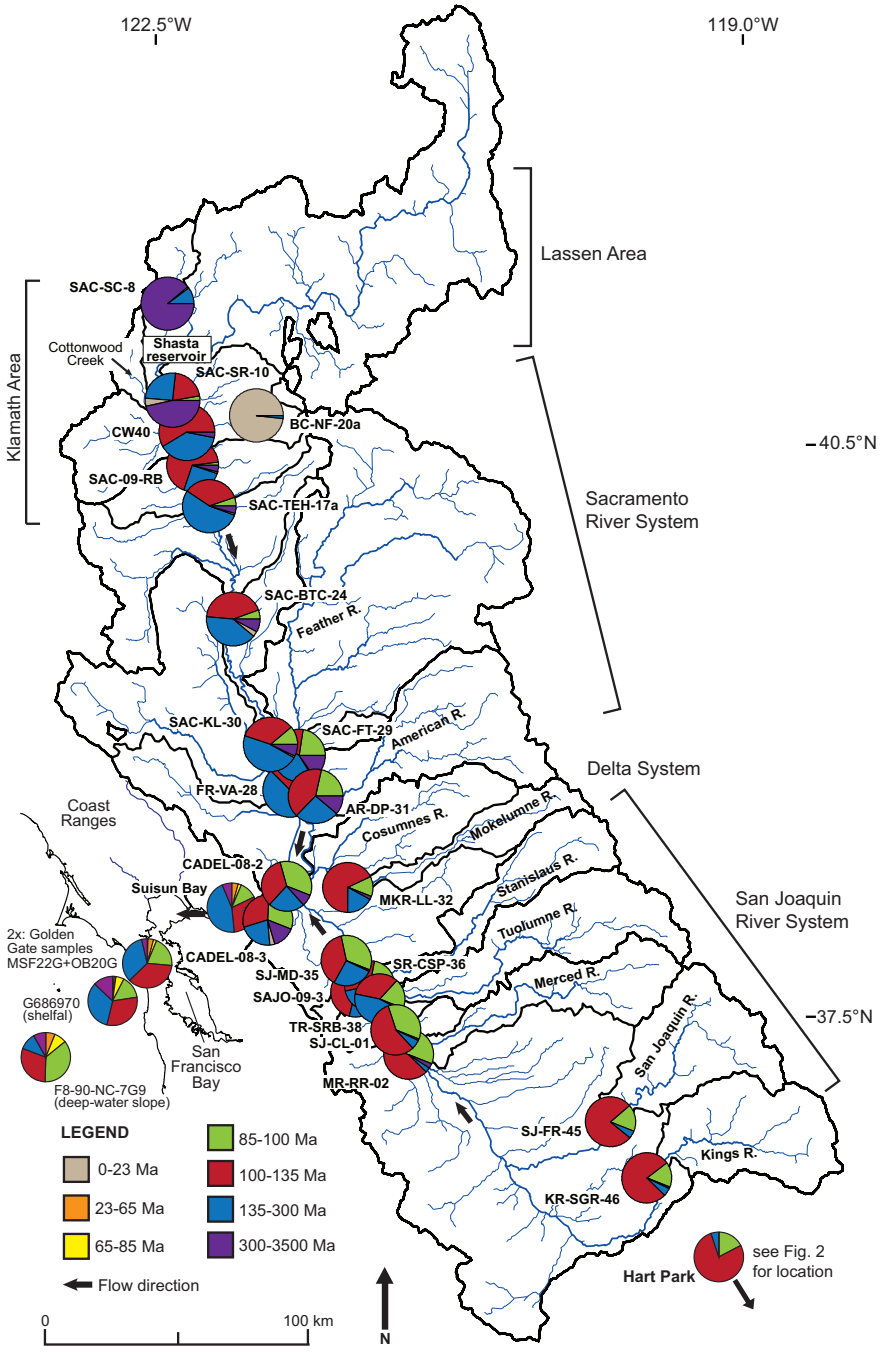

Fig. 3. Map of detrital zircon sample distributions and results shown as pie diagrams representing age populations discussed in the text.

Wright and Wyld, 2007; Surpless and Augsburger, 2009; Surpless, 2014). In some examples below, this broad 3500 to 300 Ma population is more usefully subdivided into Paleozoic and Proterozoic age groups.

300 to 135 Ma Bin.—Jurassic zircon account for most grains that fall into the 300 to 135 Ma bin. The NW-SE trending Jurassic magmatic arc extended across the entire study area. However, the highest concentrations of Jurassic plutons occur within the Klamath Mountains (Irwin, 1981; Wright and Fahan, 1988; Irwin and Wooden, 1999). Derivative Jurassic strata within the Klamaths (Wright and Wyld, 1994) and Western Sierra Nevada Foothills belt (Ernst and others, 2007) also contain significant Jurassic zircon. Finally, erosion of Cretaceous–Eocene strata also contributes both Jurassic and earliest Cretaceous detrital zircon (Degraff–Surpless and others, 2002; Wright and Wyld, 2007; Sharman and others, 2015).

135 to 100 Ma and 10 to 85 Ma Bins.—The primary source for middle Cretaceous detrital zircon is the Sierra Nevada batholith (Irwin, 2003; Chapman and others, 2012) and derivative Cretaceous strata within the Great Valley group, Coast Ranges, and Foothills belt (Degraff–Surpless and others, 2002; Sharman and others, 2015). Late Cretaceous (100–85 Ma) zircon is distinguished because it is derived from the youngest intrusive centers present within the Sierra Nevada batholith (Ducea, 2001; Irwin, 2003; Ducea and Barton, 2007). These are preferentially exposed in the southern and central segments of the Sierra Nevada.

85 to 65 Ma, 65 to 23 Ma, and 23 to 0 Ma Bins.—These bins typically account for a very minor proportion (<1%) of the detrital zircon carried by the Sacramento and San Joaquin Rivers and their tributaries but are more abundant (up to 5%) in samples from the Sacramento-San Joaquin Delta, San Francisco Bay, and the offshore shelf. Because Sierra Nevada magmatism was over by 85 Ma, this younger zircon is likely derived from reworking of sedimentary rocks that received extraregional sediment from either the Mojave (85–65 Ma) or Idaho-Nevada regions (65–23 Ma) or from younger local sources such as the southern Cascades volcanic arc and Coast Ranges volcanic centers (0–23 Ma; Cecil and others, 2010; Cassel and others, 2012; Dumitru and others, 2013; Sharman and others, 2013, 2015; Gooley and others, in press[3]). All of the above-mentioned Cenozoic age components can be contributed by erosion of Cenozoic strata exposed within the Coast Ranges (Gooley and others, in press[4]).

The following comparison discusses the detrital zircon age systematics of figure 3 in terms of three distinct geographic regions: (1) the San Joaquin River system; (2) the Sacramento River system; and (3) the Sacramento–San Joaquin Delta, San Francisco Bay, and the adjoining continental shelf. Figures 4, 5 and 6 provide more details for regions 1–3 including KDE plots, histograms, and bar graph proportions for specific samples.

San Joaquin River System

The two main headwater tributaries to the axial San Joaquin system, the Kings River and the upper San Joaquin River, are represented by samples KR-SGR-48 and SJ-FR-45, respectively (figs. 3 and 4). Detrital zircon age spectra from these rivers are similar. Each yields dominantly Early Cretaceous grains (77–78%) with subordinate Late Cretaceous (16–17%) and Jurassic (5%) zircon. The prevalence of middle Cretaceous zircon continues downstream in sample SJ-CL-01 and in the Merced River (MR-RR-02) (fig. 4). Sample SAJO-09-3 is downstream of the confluence of the Tuolumne and San Joaquin Rivers (fig. 3). While it continues to be dominated by Cretaceous zircon (44% Late Cretaceous vs. 33% Early Cretaceous), appreciable Jurassic zircon also appears (22%). In the Tuolumne River (TR-SRB-38), the abundance of Jurassic zircon grows to 45 percent and exceeds the proportions of Early and Late Cretaceous grains (34% and 19%, respectively). Farther downstream, the Stanislaus River (SR-CSP-36)

[3] Gooley, J. T., Grove, M., and Graham, S. A., in press, Tectonic evolution of the central California margin as reflected by detrital zircon composition in the Mount Diablo region *in* Sullivan, R., Sloan, D., and Unruh, J. R., editors, Geological Framework of Mount Diablo: Geological Society of America Special Paper.
[4] Ibid.

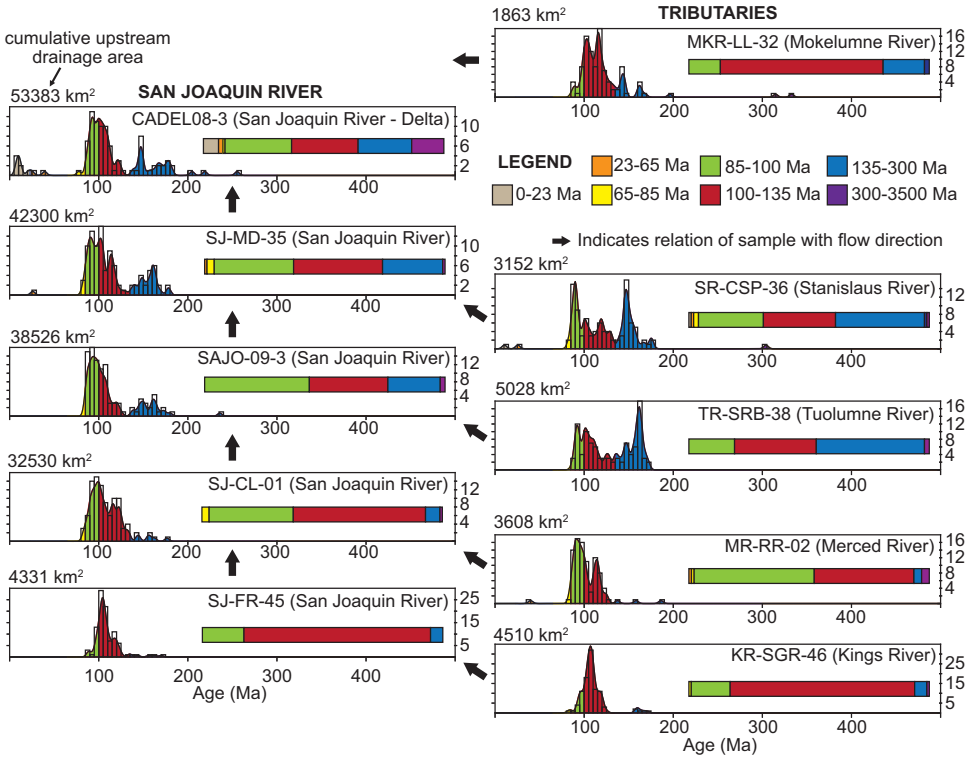

Fig. 4. Detrital zircon results from the San Joaquin River system and tributaries. Results are shown as histograms, kernel density estimated probability curves colored by population, and as colored-age proportion bar graphs. Note that histograms only show ages between 0–500 Ma.

is also characterized by subequal proportions of Jurassic, Early Cretaceous, and Late Cretaceous zircon (fig. 3). This appears to reflect contributions from both the Foothills belt and the Sierra Nevada batholith (fig. 1). The systematic change in detrital zircon provenance signature along the San Joaquin River represented by samples SJ-FR-45, SJ-CL-01, SAJO-09-3, through SJ-MD-35 mirrors these incremental contributions (fig. 4). Finally, the Mokelumne River drains directly into the delta region (fig. 3). Sample MKR-LL-32 is dominated by Early Cretaceous zircon (~68%) with lesser proportions of Jurassic (17%) and Late Cretaceous zircon (13%; fig. 4).

Sacramento System

Detrital zircon age spectra from the Sacramento River system are considerably more variable than those for the San Joaquin River (fig. 3). Beginning at the northern end, sample SAC-SC-8 was collected from Slate Creek, upstream of the Shasta reservoir (fig. 3). Note that we consider SAC-SC-8 to represent a tributary for the purposes of this study (fig. 5). Slate Creek drains the Trinity peridotite, overlying late Paleozoic volcanic and sedimentary cover, and younger Mesozoic terranes and plutons of the Klamath Mountains (fig. 1). Sample SAC-SC-8 is dominated by Paleozoic zircon (85%; ~300–500 Ma) with a small proportion (10%) of Jurassic grains present. A dramatic decrease in the proportion of Paleozoic zircon occurs south of Shasta reservoir (fig. 3). Sample SAC-SR-10 contains only 36 percent Paleozoic while the proportions of Jurassic and Early Cretaceous zircon increase to 25 percent and 17 percent, respectively (fig.

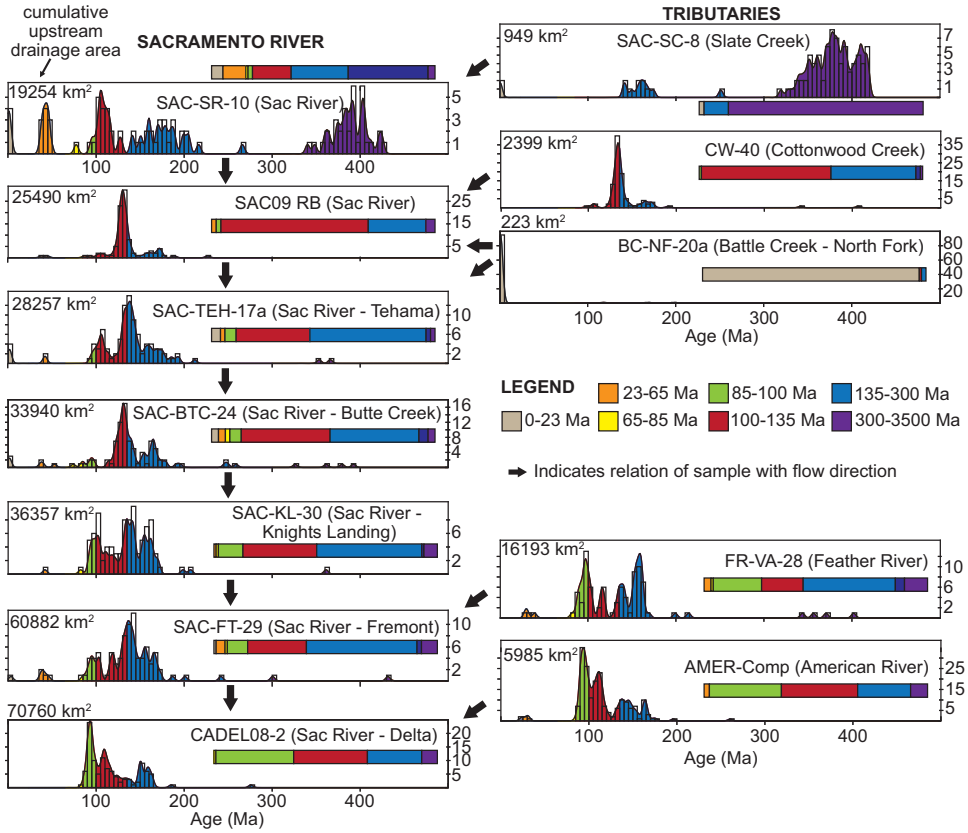

Fig. 5. Detrital zircon results from the Sacramento River system and tributaries. Results are shown as histograms, kernel density estimated probability curves colored by population, and as colored-age proportion bar graphs. Note that histograms only show ages between 0–500 Ma.

5). In similar fashion, the next downstream sample along the Sacramento River (SAC09) yields dominantly Early Cretaceous (66%) and Jurassic (~25%) grains with essentially no Paleozoic zircon present. The abundance of Jurassic and Early Cretaceous populations in SAC09 RB is also characteristic of a sample (CW-40) from its nearest upstream tributary, Cottonwood Creek (fig. 3). The proportions of Jurassic and Early Cretaceous zircon in CW-40 are 38 percent and 58 percent, respectively (figs. 3 and 5). Continuing down the Sacramento system, SAC-TEH-17A and SAC-BTC-24 are also dominated by Jurassic and Early Cretaceous zircon (figs. 3 and 5).

A similar downstream dilution in locally derived zircon exists east of the Sacramento River. The Battle Creek tributary drains the Mount Lassen area, the southernmost extent of the modern Cascade volcanic arc (figs. 1 and 3). Battle Creek enters the Sacramento River before Tehama (fig. 1). Sample BC-NF-20A consists entirely of *ca.* 500 ka zircon from the Lassen volcanic field (fig. 5). Young zircon from Lassen is sparse (4%) in SAC-TEH-17A, decreases downstream to 3 percent in SAC-BTC-24, and is absent in the next downstream sample, SAC-KL-30 (figs. 3 and 5).

By the point that the Feather River enters the Sacramento River near Knights Landing, there is essentially no indication of detrital zircon derived from either the Klamath Paleozoic or modern Cascade arc (fig. 3). The detrital zircon age distribution of Sacramento River sample SAC-KL-30 just north of the Feather River is similar to the

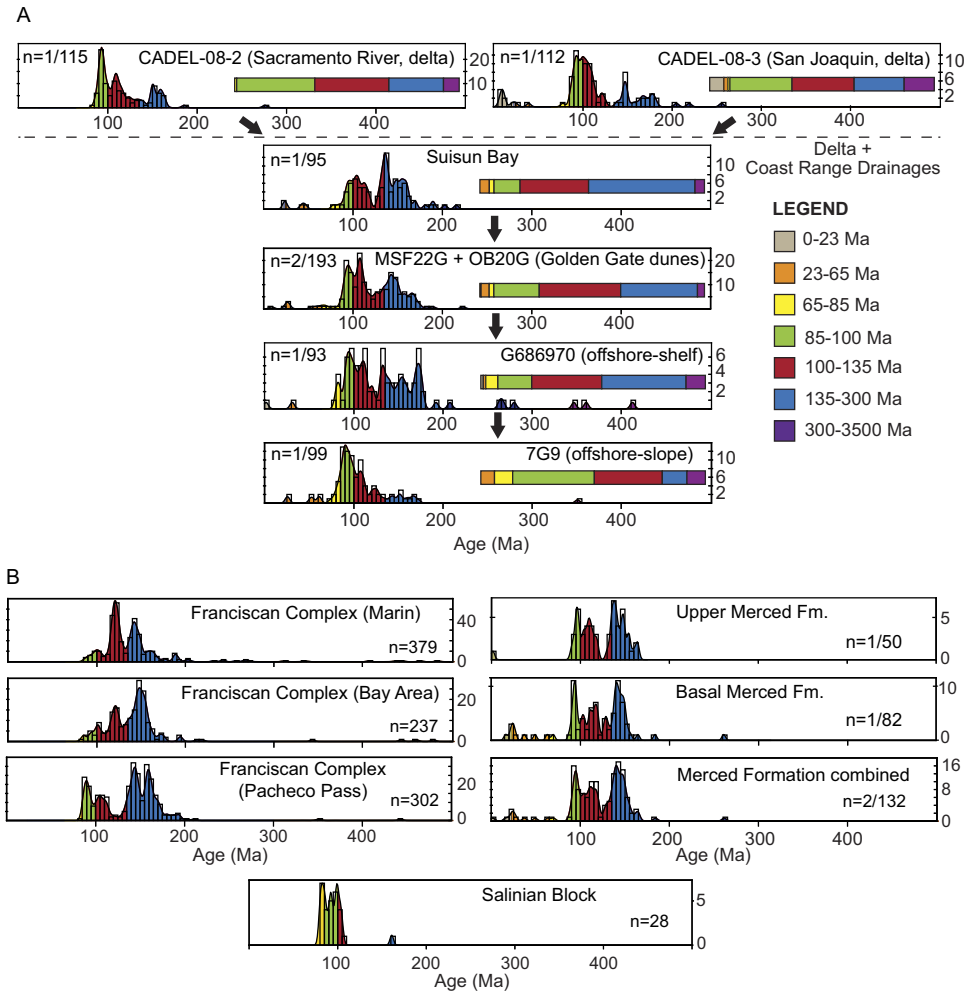

Fig. 6. (A) Detrital zircon results from the Sacramento–San Joaquin Delta and westward to offshore California. Results are shown as histograms, kernel density estimated probability curves colored by population, and as colored-age proportion bar graphs. (B) Detrital zircon spectra from local sources including the Franciscan Complex in the Coast Ranges, the coastal Merced Formation, and the Salinian block. Note that histograms only show ages between 0–500 Ma. Marin Franciscan Complex ages are compiled from Prohoroff and others (2012), Bay Area Franciscan ages from Snow and others (2010), Pacheco Pass Franciscan ages from Ernst and others (2009), Salinian block ages from Kistler and Campion (2001), and Merced Formation from Xiao and Grove (2012).

two upstream samples (SAC-BTC-24, SAC-KL-30) but now also contains a significant proportion (~11%) of Late Cretaceous zircon. The Feather River traverses the northern Sierra terranes and the Sierra Nevada batholith (fig. 1). Feather River sample FR-VA-28 contains 22 percent Late Cretaceous, 19 percent Early Cretaceous, 45 percent Jurassic, and 10 percent Proterozoic zircon (figs. 3 and 5). Feather River detrital zircon input into the Sacramento River is evident downstream in sample SAC-FT-29. It yields 9 percent Late Cretaceous, 26 percent Early Cretaceous, 50 percent Jurassic, and 7 percent Proterozoic zircon (fig. 5).

Like the Feather River, the American River drains the northern Sierra terrane, the central Sierran Foothills belt, and plutons of the Sierra Nevada batholith (fig. 1). It

joins the Sacramento River just as it reaches the Sacramento-San Joaquin Delta region. Sample AMER-Comp is a compilation of three closely spaced samples collected along the American River (fig. 2). The detrital zircon age distribution from the composite sample consists of 32 percent Late Cretaceous, 34 percent Early Cretaceous, 24 percent Jurassic, and 8 percent Proterozoic grains (figs. 3 and 5). Note that the 2 percent Paleogene zircon present is likely reworked from stream deposits from rivers that flowed across the Sierra Nevada during the Eocene (Cassel and others, 2012).

Sacramento-San Joaquin Delta to the Pacific Ocean

The Sacramento-San Joaquin Delta is formed at the confluence of the Sacramento, American, Mokelumne, and San Joaquin Rivers (fig. 3). Two detrital zircon samples represent the delta (CADEL08-3 and CADEL08-2). Sample CADEL08-3 was collected at the southern end of the delta. It contains 28 percent Late Cretaceous, 28 percent Early Cretaceous, 22 percent Jurassic, and 13 percent Proterozoic zircon (fig. 6). A readily detectable amount of Neogene zircon (~8%) is also present. Sample CADEL08-2 represents the northern end of the delta and contains a remarkably similar age distribution: 35 percent Late Cretaceous, 33 percent Early Cretaceous, 24 percent Jurassic (24%), and 7 percent Proterozoic zircon (fig. 6).

Prior to entering the San Francisco Bay, the combined Sacramento and San Joaquin Rivers flow through the Coast Ranges into Suisun Bay (fig. 3). Sample SUISUN BAY was dredged from the bay and consists of 14 percent Late Cretaceous, 31 percent Early Cretaceous, Jurassic (~47%), and 4 percent Proterozoic zircon (figs. 3 and 6). Cenozoic grains account for the remaining 4 percent. This represents a significant decrease in Late Cretaceous zircon relative to Early Cretaceous as well as an increase in Jurassic zircon relative to samples within the Sacramento-San Joaquin Delta (fig. 6). The reduction in the abundance of Late Cretaceous zircon is consistent with dilution of the delta detrital zircon provenance signature by sediment locally eroded from Early Cretaceous Great Valley and Franciscan Complex rocks present within the Coast Ranges.

Additional evidence for dilution of Sacramento/San Joaquin River sand by locally derived Coast Ranges sediment is provided by sands dredged from the Golden Gate dune field just west of San Francisco. A combined sample from the submarine dune field yielded 22 percent Late Cretaceous, 36 percent Early Cretaceous, and 34 percent Jurassic zircon (fig. 6). Similar to Suisun Bay, Proterozoic and Cenozoic ages are relatively minor with 3 percent and 4 percent, respectively. Sample G686970 is a sample dredged from the continental shelf west of the San Francisco Bay (fig. 2). It also contains only 20 percent Late Cretaceous zircon and is dominated by Early Cretaceous (31%) and Jurassic (38%) zircon (fig. 6). Proterozoic grains account for a little more than 5 percent of the population and there is a small proportion (3%) of Paleozoic grains.

Finally, the deep-water offshore culmination of the central California routing system is represented by sample F-8-90-NC-7G9, which was subsampled from the upper ~60 cm of a gravity core (fig. 3). The detrital zircon age distribution in this sample contains 44 percent Late Cretaceous, 30 percent Early Cretaceous, and 11 percent Jurassic U-Pb ages (fig. 6). Note that the enrichment of the sand from F-8-90-NC-7G9 in Late Cretaceous vs. Early Cretaceous zircon and the subordinate amount of Jurassic grains are more in line with the provenance signature measured for the Sacramento-San Joaquin Delta. About 4 percent Proterozoic and 8 percent Cenozoic zircon are also present in F-8-90-NC-7G9.

Whole-rock Major and Trace Element Geochemistry of River Mud

The whole-rock geochemistry of sediments results from competing influences of provenance, physical vs. chemical weathering, diagenesis, and sediment sorting (McLennan and others, 1990; McLennan and Taylor, 1991; McLennan and others,

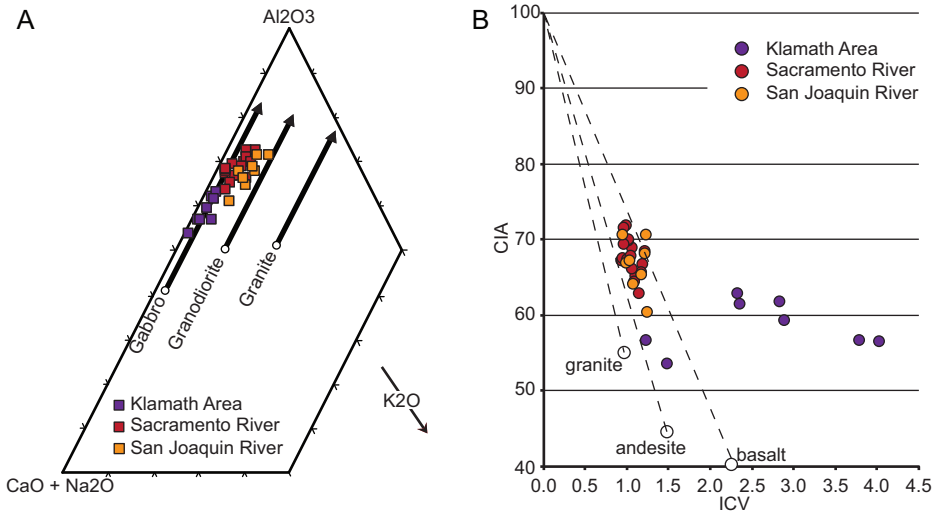

Fig. 7. Major element geochemistry comparisons of modern samples from the Central Valley. (A) A-CN-K diagram (after Nesbitt and Young, 1984, 1989) showing weathering trends for modern mud samples from the Central Valley. (B) Comparison of the chemical index of alteration (CIA) vs. index of compositional variability (ICV) in Central Valley mud compared with average compositions of granite, andesite, and basalt (after Cox and others, 1995).

1993; Cullers, 1994). In the case of modern sediment, post-depositional diagenesis is not an important factor. If the sediment analyzed is of the same grain size and chemical weathering is minor, the bulk chemical signatures of the source rock assemblages should persist in the sediments derived from them, rather than being altered during transport (see Basu and others, 2016 for discussion).

Major element geochemistry.—Element concentrations are reported in the data supplement (Appendix and data supplement, http://earth.geology.yale.edu/%7eajs/SupplementaryData/2019/Malkowski). A widely applied approach to assess chemical weathering trends is to plot the proportions of Al_2O_3, CaO + Na_2O, and K_2O on an A-CN-K ternary diagram (Nesbitt and Young 1982, 1984, 1989). Samples from this study define weathering trends expected for mafic to intermediate parent rocks (fig. 7A).

Klamath area samples plot along an average gabbroic weathering trend that is likely misleading (fig. 7A). While gabbro intrusions occur within the Trinity peridotite (Wallin and Metcalf, 1998; Metcalf and others, 2000), the dominant lithology present is ultramafic rock (Lindsley-Griffin, 1991). Chemical weathering of olivine and orthopyroxene in ultramafic rock produces an anomalous silica- and Cr-rich residual sediment. Large-scale chemical weathering of ultramafic rocks is thus capable of skewing geochemical estimates of source rock composition (Beinlich and others, 2018).

With the exception of the Klamath Mountains, the fact that host rocks within the study area are relatively fresh and proximal to the main river trunks, means that it is likely that the effects of chemical weathering are minor relative to the control of source rock composition. For example, Sacramento River samples south of the Klamath Mountains sensibly plot near the average gabbro trend but slightly closer to granodiorite. Similarly, San Joaquin River samples plot between the average gabbro and average granodiorite weathering trends (fig. 7A).

The degree of weathering can also be estimated by plotting the chemical index of alteration (CIA) vs. the index of compositional variability (ICV) (fig. 7B). Values of CIA are calculated from the ratio of the molecular proportions of Al_2O_3 to the sum

of Al_2O_3, K_2O, Na_2O, K_2O, and CaO*, which is then multiplied by 100 (Nesbitt and Young, 1982; McLennan and others, 1993). In our case, CaO* is determined by correcting for the mole proportion of apatite using P_2O_5 (McLennan and others, 1993; Fedo and others, 1995). Calculated CIA values are commonly below 50 in unweathered igneous rocks and approach 100 in residual clays (illite, kaolinite, montmorillonite). Mudrocks typically range between 70 to 75 (McLennan and others, 1993). Values of ICV provide a means to assess source rock type (Cox and others, 1995; Potter and others, 2005). This index is determined as the ratio of the sum of CaO, K_2O, Na_2O, Fe_2O, MgO, MnO, and TiO_2 over Al_2O_3. Non-clay silicate minerals low in Al (for example biotite, amphibole, pyroxene) contain higher ICV values (3–100); whereas Al-bearing residual clay minerals (kaolinite, illite, montmorillonite) yield low ICV values (0.03– 0.5; Cox and others, 1995).

The plot of CIA vs. ICV values for whole-rock mud samples from the Sacramento and San Joaquin Rivers is nearly indistinguishable (fig. 7B). Sediment from the Sacramento and San Joaquin River systems yields a cluster of CIA values between 60 to 72, which indicates less weathering than is typical for mudrocks (70–75 ppm, Taylor and McLennan, 1985; McLennan and others, 1993) (fig. 7B). The tightly clustered CIA vs. ICV array over an ICV range of 1.0 to 1.5 reflects an intermediate composition of the source region between basalt and andesite (fig. 7B). In contrast, highly scattered results are obtained for Klamath area sediments. Values for CIA range from 53 to 63 while ICV values scatter widely between 1 to 4 reflecting Al-poor, mafic to ultramafic sources.

Trace element geochemistry.—Relatively immobile trace elements such as Zr, V, Sc, Th, Cr, and Ni are useful provenance indicators (Bhatia and Crook, 1986; McLennan and others, 1990; Cullers, 1994). Numerous comparisons of the abundances and ratios of these elements have proven to be useful for distinguishing between basic vs. silicic rocks in the source region (Taylor and McLennan, 1985; Wronkiewicz and Condie, 1987, 1990). Concentrations of Cr and Ni are commonly elevated (>500 ppm) in ultramafic rocks. Consequently, monitoring Cr and Ni concentrations in fine-grained sediments is considered to offer one of the few reliable ways to detect mafic and ultramafic sources in a sediment dispersal system (Papavassiliou and Cosgrove, 1982; Garver and Scott, 1995; Garver and others, 1996). Note that as pointed out by Beinlich and others (2018), however, Cr abundances are artificially enhanced in sediments due to the incongruent nature of chemical weathering of ultramafic rocks.

Ultramafic rocks (for example, the informally named Trinity ophiolite) are widely exposed in the Klamath Mountains and to a lesser degree in the Sierran Foothills belt (fig. 1). Within only two exceptions, samples from Klamath Mountain drainages have concentrations of Cr and Ni in excess of 1000 ppm. These values are much higher than those measured for other samples in the Sacramento and San Joaquin systems (fig. 8A). Sacramento River samples typically contain *ca.* 100 ppm Ni and 100 to 300 ppm Cr. San Joaquin samples have even lower concentrations that range from 30 to 100 ppm for Ni and 80 to 100 ppm for Cr (fig 8A). Note that the concentrations of Cr and Ni reported by Surpless (2014) were appreciably higher for Early and Late Cretaceous mudstones of the Sacramento Basin than they are today (fig. 8B). Alternatively, those measured for equivalent age lithologies in the San Joaquin Basin yield similar, albeit more scattered values relative to the modern sediments (fig. 8B).

Incompatible trace elements such as Th and Zr are traditionally normalized to a more compatible element (Sc) as a way to indicate mafic vs. felsic sources (McLennan and Taylor, 1991; McLennan and others, 1993). A comparison of Th/Sc vs. Zr/Sc values measured from Great Valley river mud reveals a pronounced, southward increase from the Klamath Mountains south to the San Joaquin River and its tributaries in the southern and central Sierra Nevada batholith (fig. 9). This trend defines an evolution from intermediate compositions in the north (andesite and granodiorite) to

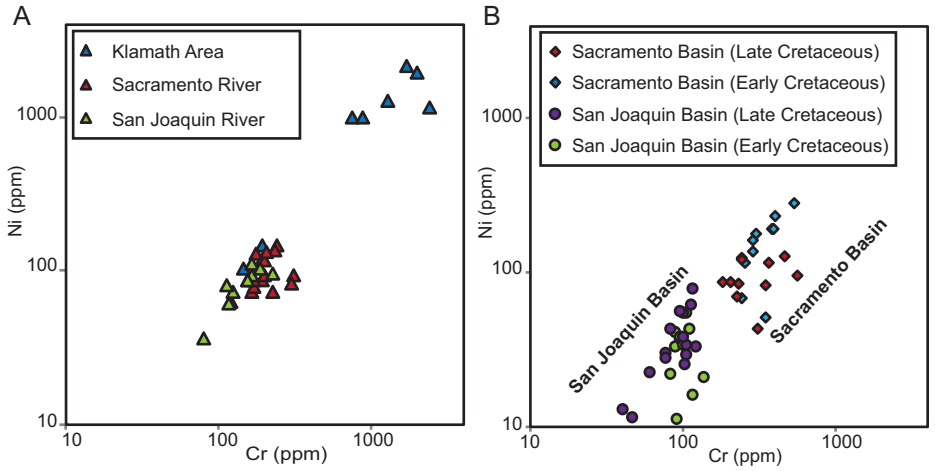

Fig. 8. Plots of Cr vs. Ni concentrations in modern Klamath and Central Valley samples (A) and from the Cretaceous Great Valley group (B). Data from Cretaceous samples from Surpless (2014).

more felsic, granitic compositions in the south (fig. 9A). First- and second-order stream samples from Klamath Mountains drainages lie close to andesitic values. Second-order stream samples in the Sacramento River system fall between andesite and granodiorite composition while San Joaquin samples are closer to granitic compositions (fig. 9A). These same trends are exhibited by Early Cretaceous and Late Cretaceous shales from the Great Valley group (Surpless, 2014; fig. 9B).

Vanadium–scandium ratios have been demonstrated to be particularly useful for revealing volcanogenic sediment (Ryan and Williams, 2007). For example, active continental margins (volcanic arcs) are characterized by high V/Sc while passive continental margin sediments have lower V/Sc values (Bhatia and Crook, 1986). Excluding the low-order drainages from the Klamath area, river mud samples from the Great Valley exhibit a highly correlated array of V vs. Sc concentrations. Values are lowest for the San Joaquin River system and highest for the Sacramento River system (fig. 10A). Note that the Klamath area mud samples define a separate array due to lower V concentrations between 67 to 119 ppm vs. Sc concentrations between 12 and 26 ppm. Note that mud sampled from Slate Creek has anomalously high V (197 ppm) (fig. 10A). San Joaquin Valley sediments have 13 to 21 ppm of Sc and 123 to 202 ppm of V whereas Sacramento Valley sediments have Sc concentrations from 21 to 27 ppm and 177 to 225 ppm of V. This trend may reflect an increased volcanic character for sediment entering the Sacramento River system that is derived from material eroded from the Cretaceous Great Valley group (Surpless, 2014) and/or Cenozoic volcanic rocks (Lassen Volcanics; fig. 1).

Rare earth elements (REEs) are valuable provenance indicators in fine-grained sediments because they are not fractionated by most sedimentary processes, are largely insoluble, and tend to concentrate in clays (Taylor and McLennan, 1985; Cullers and others, 1987; McLennan, 1989; McLennan and others, 1990; Condie, 1991; Taylor and McLennan, 1995; Potter and others, 2005). Rare-earth element concentrations from mud samples show a systematic north-south trend in the extent of fractionation between heavy (HREEs) and light rare earth elements (LREEs) (fig. 11). River mud from the Klamath Mountains region yields essentially unfractionated REE patterns consistent with an ophiolitic source (Gruau and others, 1991, 1995). River mud samples from the Sacramento River system are moderately enriched in LREEs while

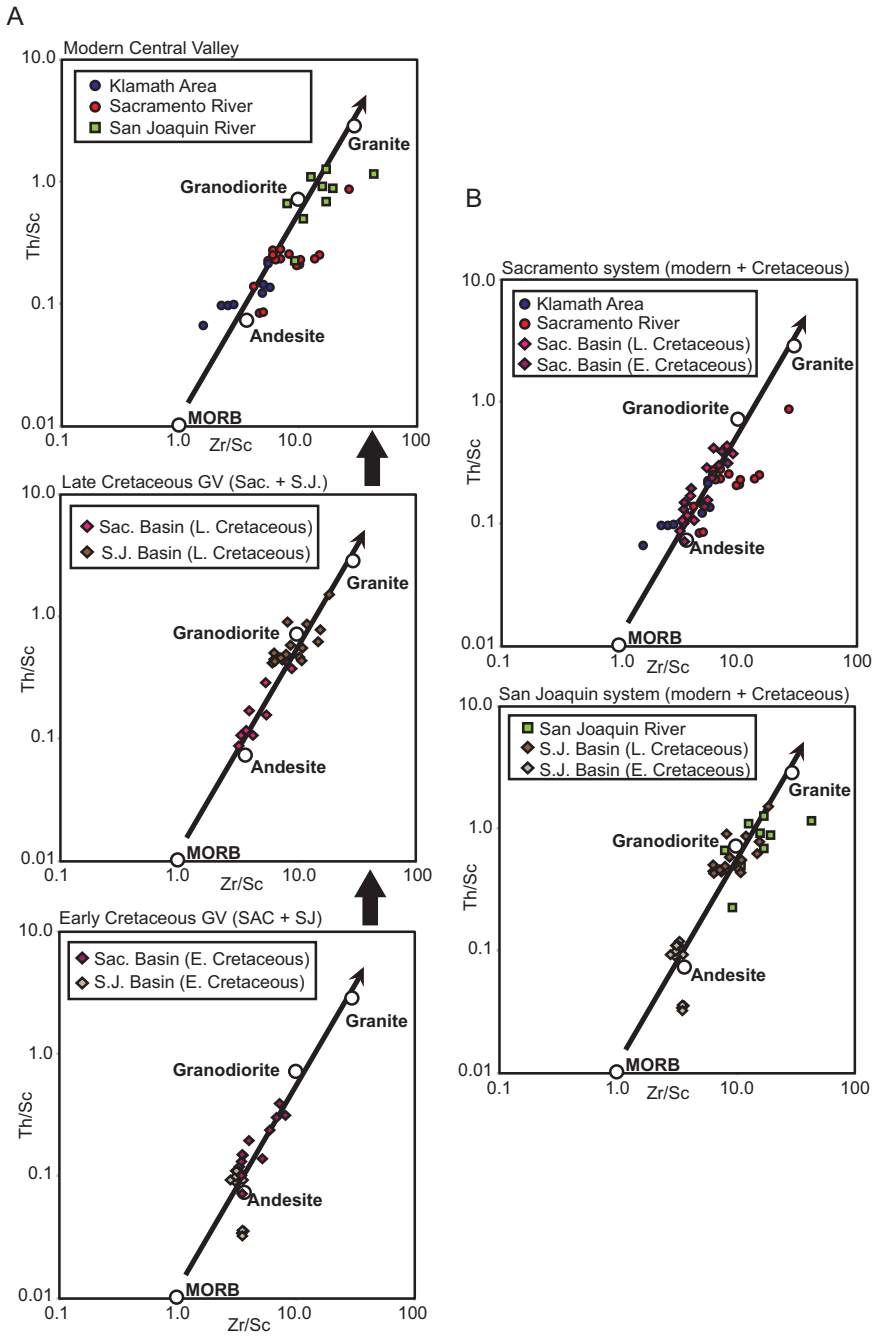

Fig. 9. Plots of Zr/Sc vs. Th/Sc in modern Central Valley sediment and the Cretaceous Great Valley group. (A) Comparisons of the Sacramento Basin/Valley with the San Joaquin Basin/Valley beginning the Early Cretaceous (lower plot), Late Cretaceous (middle plot), and modern systems (upper plot). (B) Plots comparing samples from the Sacramento system (upper plot) and the San Joaquin system (lower plot). Cretaceous Great Valley group data from Surpless (2014). Reference compositions of MORB, andesite, granodiorite, and granite are from Taylor and White (1966), Taylor and McLennan (1985), and Gale and others (2013). MORB is abbreviated for mid ocean ridge basalt.

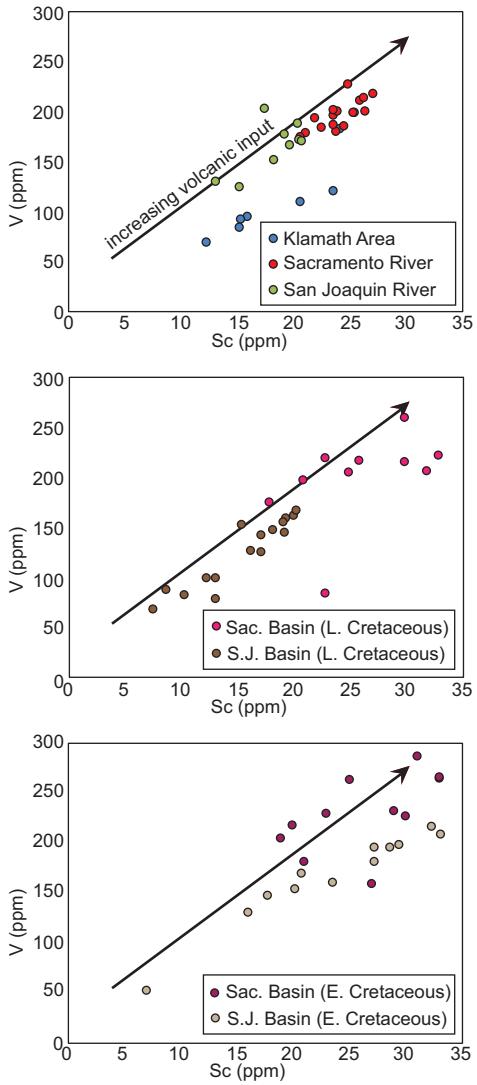

Fig. 10. Plots comparing the relative concentrations of Sc vs. V in samples from the modern Central Valley (upper plot), Upper Cretaceous Great Valley group (middle plot) and the Lower Cretaceous Great Valley group (lower plot). Increasing concentrations of Sc and V are suggestive of increased volcanic input from detrital sources (see text for discussion). Cretaceous Great Valley group data from Surpless (2014).

equivalent sediment from the San Joaquin River system exhibits significant enrichment in LREE (fig. 11).

Bulk zirconium.—Bulk Zr concentration provides a useful proxy for estimating the abundance of zircon. Whitmore and others (2004) examined the control of sediment grain size upon the mineralogy and geochemistry of river sediment and concluded that grain size did not significantly impact the abundance of zircon (fig. 12A). Accordingly, we use the Zr concentration of mud as a proxy for zircon concentration in the associated sand fraction. Results from the Great Valley reveal that San Joaquin River samples generally have higher Zr concentrations in river mud than do samples from the Sacramento River (figs. 12B and 12C). For example, Zr concentrations from San

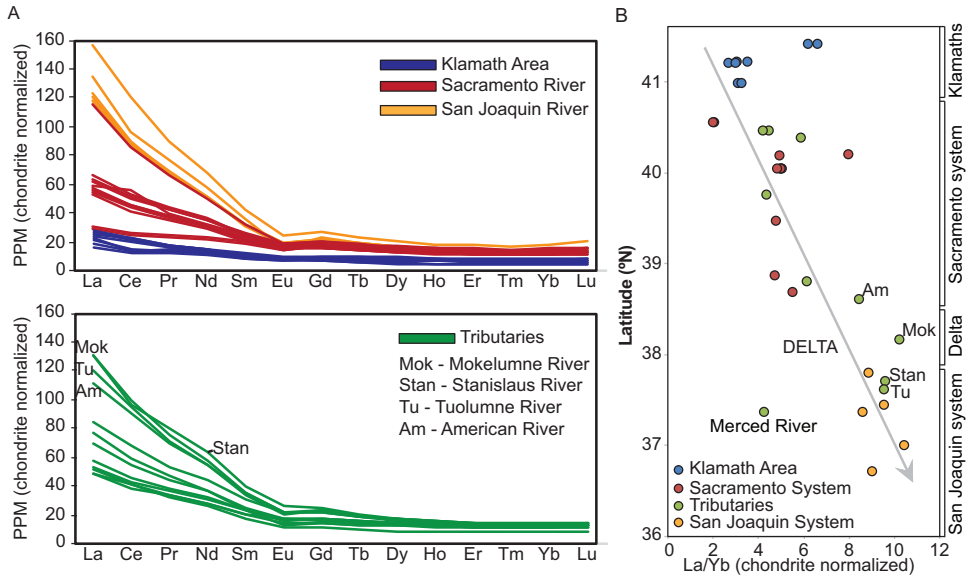

Fig. 11. Rare-earth element (REE) trends in modern mud samples from central California. (A) Spider charts showing the fractionation of light to heavy REEs in the main axial systems of the Sacramento and San Joaquin Rivers (upper chart) and concentrations in the major tributaries (lower chart). (B) La/Yb ratios plotted relative to location (latitude) in central California showing a general north to south increase in the amount of fractionation between light REEs (La) and heavy REEs (Yb).

Joaquin River mud commonly yield >200 ppm of Zr and range up to 850 ppm. Alternatively, river muds from the Sacramento River yield Zr concentrations between 100 to 200. Values as high as 547 and 297 ppm were measured near Red Bluff and Tehama, respectively (figs. 1 and 12C). River mud from the Klamath Mountains region yields Zr concentrations that are all below 100 ppm.

A higher density of sampling has been performed with samples dredged from the San Francisco Bay area and the adjacent continental shelf (fig. 12B). Zirconium concentrations from Suisun Bay range between 122 to 983 ppm while those from San Pablo Bay were all low (122–238 ppm) (figs. 12B and 12D). Alternatively, samples from the Golden Gate dune field consistently yielded much higher Zr concentrations between 639 and 4280 ppm (fig. 12D). In fact, 9 of 15 Golden Gate dune field samples contained in excess of 1000 ppm of Zr (fig. 12D). This enrichment of zircon is likely attributable to the concentration of zircon in the high surge environment immediately outboard of the constrictive Golden Gate entrance to San Francisco Bay. The Zr concentration measured from the gravity-core sample F-8-90-NC-7G9 from the offshore deep-water slope region is also somewhat elevated (398 ppm).

Mixture Modeling

The 2-component mixture modeling approach employed for predicting detrital zircon age distributions from the combined bedload of a tributary-trunk pair of streams is described in the background section with further details provided in Appendix 1 at the end of this paper. Calculations were carried out for seven tributary-trunk river combinations in the Central Valley for which there were available stream gauge data. Four out of the seven mixture combinations yielded a range of mixing coefficients that meet our criteria of a "good fit" ($V_{crit} >= V_{max}$), where Vcrit represents the 95th percentile of Vmax values observed when comparing two resampled versions

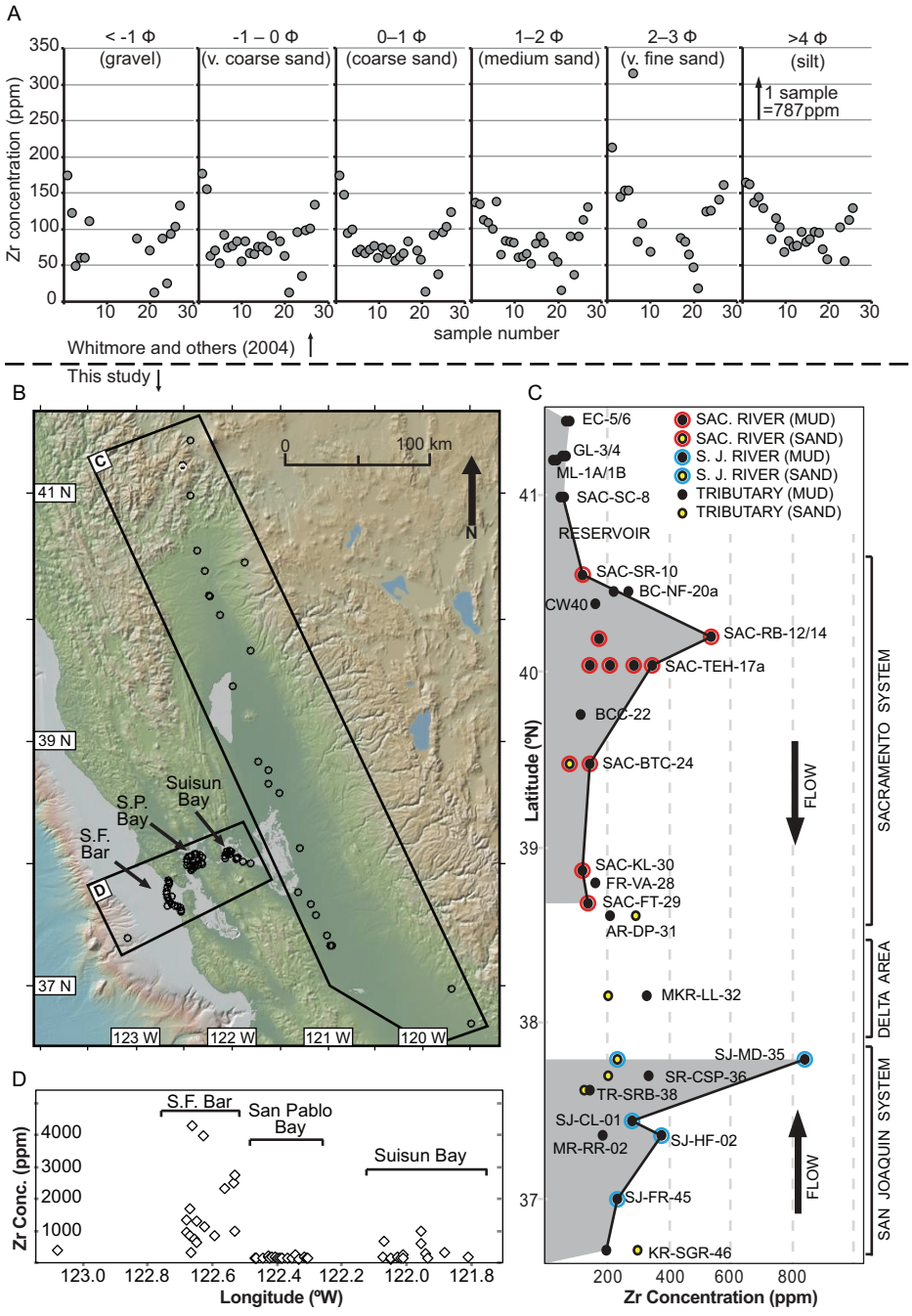

Fig. 12. Zr concentrations of modern sediment A) Comparison of Zr concentrations relative to grain size in river sediment from the New Guinea collisional zone. Data are from Whitmore and others (2004). (B) Map showing locations of mud geochemistry samples in the Central Valley and San Francisco Bay Area, central California. Basemap from GeoMapApp (v. 3.6.8). (C) Zr concentrations in Central Valley river sediment plotted relative to latitude as proxy for position along the Sacramento and San Joaquin Rivers. (D) Zr concentrations in the San Francisco Bay region and westward. Note the consistently high (>1000 ppm) concentrations associated with mud samples along the San Francisco bar outside of the Golden Gate dune field.

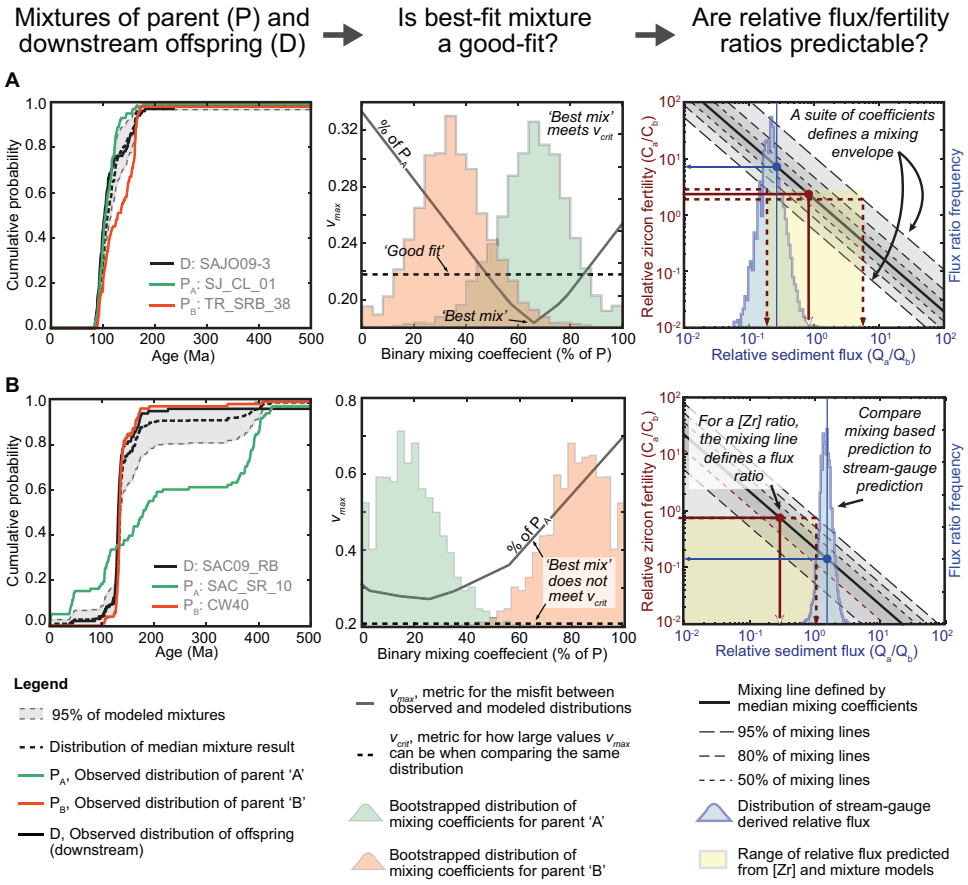

Fig. 13. Results of detrital zircon mixture modelling from two exemplary confluences in the study area. (A) Results of the Tuolumne River to the San Joaquin River; (B) result of the Cottonwood Creek into the Sacramento River. Left column shows the parents (P_A and P_B) and downstream offspring (D) Cumulative density functions (CDFs) and the distribution and mean of bootstrapped mixtures. Middle column shows histograms of the bootstrapped mixing coefficients for the two parents (green: Parent A, red: parent B). The left axis shows how V_{max} depends on the first parent, given the original observed DZ samples. Horizontal dashed line represents a tolerable value of Vmax (V_{crit}); values above this do a poor job characterizing the offspring. Solid gray line delineates the best-fit mixture coefficient of parent A. Right column highlights the tradeoffs between relative sediment flux and zircon fertility. Shaded region highlights the possible combinations of relative fluxes and relative zircon concentration predicted by 95% of the bootstrapped mixing coefficients. Maroon dashed lines show the expected ratio of fluxes given the observed variability in relative Zr concentration. Blue histogram shows an expectation for the relative bedload flux of the two parent streams based on predictions of sediment flux. Blue lines delineate the median sediment flux ratio calculated for parent A relative to parent B. Example A reflects detrital zircon population mixing of P_A and P_B with mean [Zr] (C_a/C_b) slightly *overestimating* mean relative sediment flux (Q_a/Q_b). Example B reflects detrital zircon population mixing of P_A and P_B with mean [Zr] (C_a/C_b) slightly *underestimating* mean relative sediment flux (Q_a/Q_b).

of the offspring data. Alternatively, in the other three mixtures, it is unlikely that any mixture of the samples from the two parent streams can describe the observed offspring. Figure 13 shows results from two representative calculations. For each set of calculations, the bootstrapped range of modeled distributions and mixing coefficients are highlighted in the two left columns of figure 13. We will comment further upon the significance of these results in the Discussion section.

The third column in figure 13 illustrates the relationship between relative sediment flux and Zr concentration. These plots highlight the codependence of these

two important quantities. In all cases where the relative concentration/flux ratio range can be defined by a best-fit mixture, a single calculated concentration ratio predicts the estimated flux at least within one order of magnitude (table 1). Likewise, in such cases, allowing for the range of Zr concentrations and the range of 95 percent of the mixture iterations results in overlap between the predicted sediment flux and calculated sediment flux for all mixtures, albeit with variable degrees of overlap (table 1).

DISCUSSION

A primary goal of studying the provenance characteristics of a modern major river system is to assess the extent to which key characteristics of its source region(s) are recorded with high fidelity. Similarly, it is also crucial to determine which types of provenance signals are intrinsically difficult to detect. While the catchment area of the combined Sacramento-San Joaquin River system is dwarfed by those of the Amazon, Colorado, Indus, Lena, Mississippi, Nile, Yalu-Brahmaputra, Yangtze, and other great rivers of the world, the lithologic variability of the Great Valley catchment rivals that of any other river system on Earth (fig. 1). Below, we explore how provenance signatures of geologically distinct source regions are blended and preserved (or disappear) along the course of the Sacramento and San Joaquin Rivers. We also focus on how the integrated river bed load of the Central Valley drainage system has been further modified along its recently established course from the Sacramento-San Joaquin Delta through the tectonically active Coast Ranges to the Pacific Ocean.

Evaluation of Anthropogenic Influences

Anthropogenic influences cannot be ignored within the Central Valley drainage system. The Sacramento and San Joaquin River systems have been significantly impacted by a variety of anthropogenic modifications over the past two centuries (fig. 2). These changes include channelization and levee construction within the Sacramento–San Joaquin Delta coupled with water diversion for both agricultural purposes and urban development in California's Mediterranean climate. Levee construction and reduced river flow through the delta region have certainly impacted the character of sediment delivery to San Francisco Bay and the Pacific Ocean (Krone; 1979; Wright and Schoellhamer and others, 2004; Ganju and Schoellhamer, 2010).

The construction of dams in the headwaters of many tributary streams to regulate California's water system over the past 50 to 100 years is also of considerable concern to this study (fig. 2). Dams trap large volumes of sediment and reduce sediment mobilizing flows during spring runoff. To mitigate this problem, we collected the majority of our samples downstream of major dams. The only exception to this practice was intentional sampling north of Shasta reservoir to document the nature of sediment directly delivered from the ultramafic and mafic rocks that dominate the southeastern Klamath Mountains. Reliance upon downstream samples increases the likelihood that comparisons between tributary and trunk stream samples will not be significantly affected by dams in the headwater regions. For example, although dams retain sediment, the river segment immediately downstream will be sediment deficient and erode its bed or channel margins to establish a new equilibrium sediment load (Porterfield and others, 1978; Smith and Perez-Arlucea, 2008; Schoellhamer and others, 2012; Nittrouer and Viparelli, 2014). Thus, dams enhance downstream erosion of sediments that were deposited prior to dam construction, thereby reflecting pre-dam provenance characteristics.

A third potentially problematic anthropogenic impact upon sediment transport is the hydraulic gold mining that occurred in the Foothills belt in the northern Sierra Nevada during the late 1800s (Gilbert, 1917; Brice, 1977). Hydraulic mining significantly enhanced sediment supply from the Eocene auriferous gravels prior to dam construction (Gilbert, 1917; Alpers and others, 2005). While the resulting pulse of

TABLE 1

Summary of Mixture Modeling Results

Sample	Best-fit (bootstrapped) mixtures: Avg (P50)	P2.5-P97.5	Vmax (P50)	Vmax (P2.5-P97.5)	Vcrit	Best-fit vs. good fit mixtures: P (V_50)	P (V_2.5)	P (V_97.5)	P (Vmix<Vself)	Drainage area (km^2)	Zr concentration (ppm): Min	Max	Avg	Zr-Predicted Qs ratio (Pa/Pb): Avg[1] (P50)	Min[2]	Max[2]	SG-Estimated Qs ratio (Pa/Pb): Avg (P50)	P2.5	P97.5
Pa: CADEL08-2	0.82	0.28 - 100.0								70760	81	333	207						
Pb: CADEL08-3	0.18	0.0 - 0.72								53383	136	584	360						
D: Suisun Bay	NA		*0.317*	0.221-0.422	*0.23*	0	0.06	0	*0.01*					7.923	0.159	-	4.091	2.142	7.094
Pa: SAC_SR_10	0.175	0.0 - 0.44								19254	127	129	128						
Pb: CW40	0.825	0.56 - 100.0								2399	170	170	170						
D: SAC09 RB	NA		*0.294*	0.184-0.407	*0.21*	0	0.22	0	*0.02*		180	547	363.5	0.282	0	1.962	1.568	0.974	2.497
Pa: SAC_FT_29	0.095	0.0 - 0.46								60882	146	146	146						
Pb: AR Comp.[3]	0.905	0.54 - 100.0								5985	220	300	260						
D: CADEL08-2	NA		**0.156**	0.108-0.23	**0.21**	0.36	0.74	0.01	**0.32**					0.187	0	1.662	0.878	0.408	1.952
Pa: MKR_LL_32	0	0.0 - 0.53								1863	213	335	274						
Pb: SJ_MD_35	100	0.47 - 100.0								42300	239	851	545						
D: CADEL08-3	NA		*0.296*	0.209-0.389	*0.21*	0	0.05	0	*0.01*					0	0	0.207	0.114	0.067	0.183
Pa: SR_CSP_36	0.265	0.0 - 0.62								3152	214	343	278.5						
Pb: SAJO09-3	0.735	0.38 - 100.0								38526	244	244	244						
D: SJ_MD_35	NA		**0.152**	0.103-0.232	**0.22**	0.46	0.86	0.03	**0.45**					0.316	0	0.499	0.223	0.162	0.306
Pa: SAC_KL_30	0.815	0.28 - 100.0								36357	131	131	131						
Pb: FR_VA_28	0.185	0.0 - 0.72								16193	168	168	168						
D: SAC_FT_29	NA		**0.178**	0.119-0.265	**0.22**	0.28	0.86	0.01	**0.29**					5.650	0.499	-	12.591	6.661	29.372
Pa: SJ_CL_01	0.655	0.345 - 0.91								32530	287	387	337						
Pb: TR_SRB_38	0.345	0.09 - 0.655								5028	136	151	143.5						
D: SAJO09-3	NA		**0.225**	0.142-0.322	**0.22**	0.03	0.46	0	**0.1**					0.808	0.185	6.884	0.270	0.107	0.681

Pa - parent stream A; Pb - parent stream B; D - offspring stream (downstream of Pa-Pb confluence); SG - stream gauge.

Bolded black values highlight instances where Vmax exceeds Vcrit (best-fit is a good fit); Italicized values indicate instances where the best fit is not a good fit.

[1] Using average Zr concentration as a proxy for zircon concentration and the average best-fit mixing coefficients.

[2] Using the Min (or Max) ZrB/ZrA ratio with the average best-fit mixture.

[3] American River Compilation: = AMER1+AMER2+AR_DP_31.

Vmax (P50): The median best-fitting Vmax value of the 10,000 permutations of resampled parents and offspring.

Vcrit: The 95th percentile of Vmax values from comparison of resampled versions of the offspring distribution. This provides a measure of how large values of Vmax might be just as the result of sampling a small number of grains.

p(V_50): How frequently do Vmax values from self-comparison experiments of the offspring data exceed the median median Vmax value from mixture models.

p(V_2.5): How frequently do Vmax values from self-comparison experiments of the offspring data exceed the lower 2.5th percentile of Vmax value from mixture models.

p(V_97.5): How frequently do Vmax values from self-comparison experiments of the offspring data exceed the upper 97.5th percentile of Vmax value from mixture models.

p(Vmix > Vself): How frequently a resampled mixture model predicts a Vmax value that is larger than the resampled self comparison. That is, how frequently does random sampling produce Vmax values larger than the difference observed in the mixture model.

sediment may have biased downstream sediment provenance, there are ways to test for this. For example, we would predict enhanced abundances of distinctive Eocene zircon for samples proximal to the Feather, Yuba, Bear, and American Rivers where mining activity was concentrated (Cecil and others, 2010; Cassel and others, 2012). In extra-regional Eocene deposits, the concentration of Eocene zircon is variable but can be as high as 10 percent (Dumitru and others, 2013; Sharman and others, 2013, 2015). Given that we observe only trace quantities of Eocene zircon in any of our samples and since it can be reworked naturally from Coast Ranges strata of this age (Dumitru and others, 2013; Sharman and others, 2013, 2015), we conclude that hydraulic mining artifacts have not compromised data we have collected from the lower Sacramento River system.

In summary, while the effects of these anthropogenic modifications on the results presented herein are difficult to quantify and assess in detail, the precautions we have taken and the screening tests we have performed indicate that the first-order provenance characteristics of sediment transport by modern Central Valley rivers likely closely approximate those of the Holocene (that is pre-anthropogenic) drainage network.

Downstream Propagation vs. Dilution of Provenance Trends in the Sand Fraction

This section focusses upon the evolution of the detrital zircon U-Pb age provenance signature along three major legs of the drainage network: (1) San Joaquin River, (2) Sacramento River, and (3) the combined flow of these rivers from the Sacramento-San Joaquin Delta through the Coast Ranges and San Francisco Bay to the Pacific Ocean. Figure 14 illustrates how the provenance signature along each of these legs evolves relative to the distribution of pluton crystallization ages predicted for the composite Sierra Nevada batholith based upon a database of zircon U-Pb ages compiled by Chapman and others (2012).

San Joaquin River.—Of the trunk rivers in the Central Valley, the San Joaquin River behaves in the simplest and most predictable manner (figs. 3 and 4). Downstream changes in the detrital zircon age distribution measured at various points along the San Joaquin River system closely mirror changes in tributary input. As expected, measured age distributions are strongly influenced by the Sierra Nevada batholith and the western Foothills belt. For example, the proportion of Late Cretaceous zircon doubles in response to sediment mixing at the confluence of the San Joaquin and Merced Rivers (figs. 3 and 4). The abrupt increase in Late Cretaceous zircon propagates to the next major downstream tributary, the Tuolumne River, which carries a significant Jurassic population (45%) as it transects a section of the Foothills belt in the western Sierra Nevada range. Here again, mixing is inferred simply by the observation that Jurassic ages are a minor proportion (6%) in upstream samples of the San Joaquin River, but jump to 21 percent after the confluence with the Tuolumne River which transports a significant proportion of Jurassic zircon. The provenance signature of the San Joaquin River continuously evolves downstream until it is statistically indistinguishable from the Sierra Nevada batholithic age distribution in the delta region (fig. 14).

Sacramento River.—In contrast to the San Joaquin River, the Sacramento River drainage carries sediment derived from much more heterogenous sources (figs. 1, 3, and 5). Our measurements document an abrupt downstream dilution in detrital zircon age populations associated with a major ultramafic massif (Trinity peridotite and late Paleozoic cover) and an important late Cenozoic volcanic center (Mount Lassen). For example, detrital zircon samples from the northern Sacramento River (SAC-SC-8 and SAC-SR-10) record Paleozoic, Jurassic, and Early Cretaceous sources in the Klamath Mountains. However, the next downstream sample in the Sacramento River, SAC09–RB, is dominated by Early Cretaceous zircon and failed to yield any Paleozoic ages (fig. 5). Instead, the measured age spectrum strongly resembles that of the Cottonwood Creek tributary, from the west. These data highlight an unexpectedly rapid dilution of the upstream Klamath Mountains by a seemingly minor tributary. As

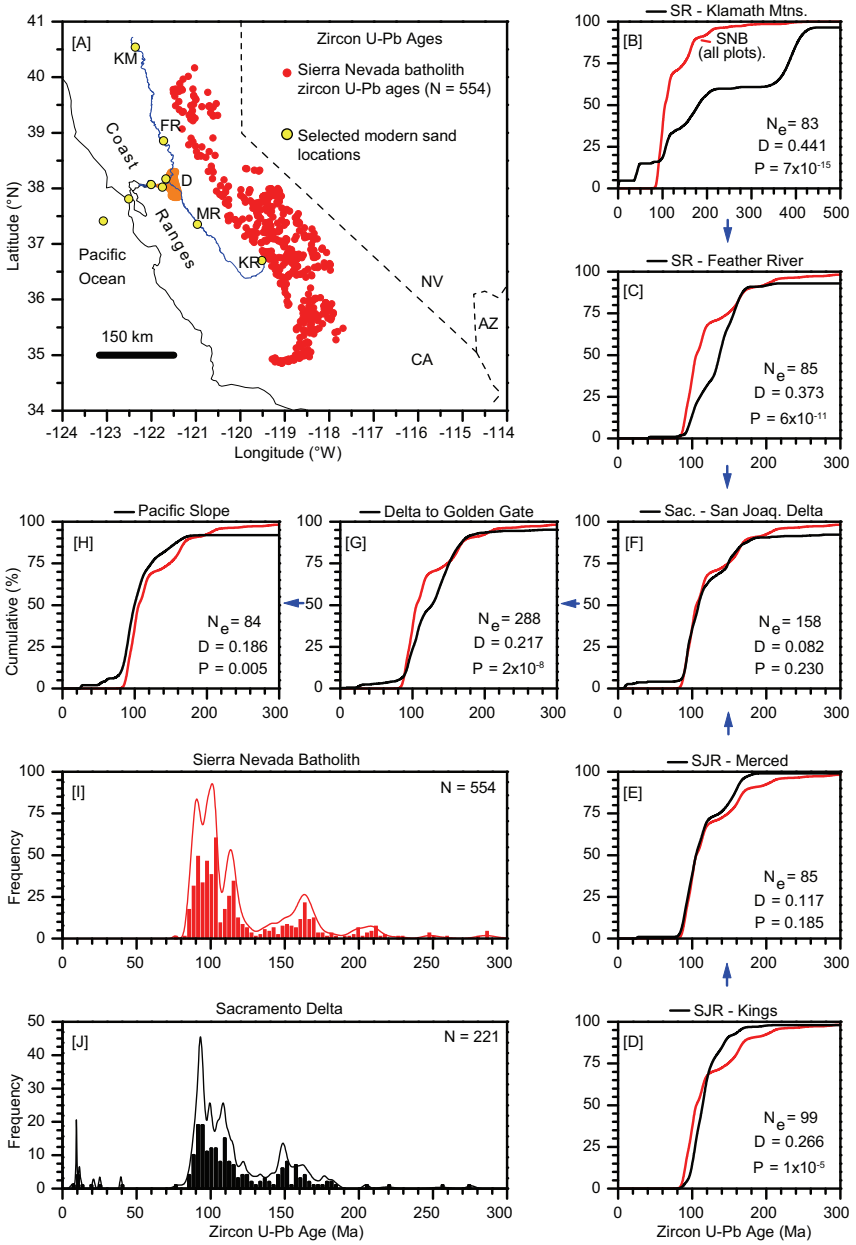

Fig. 14. Comparison of detrital zircon age distributions from the Great Valley drainage system. The Sierra Nevada batholith (SNB) is represented using a compilation of zircon U-Pb crystallization ages from Chapman and others (2012). Note that results from Salinia, the White-Inyo Range, and the Mojave Desert region have been omitted. Conventional K-S test results (Press and others, 2007) show effective sample size $N_e = [N_1N_2/(N_1+N_2)]$. D = maximum separation of cumulative age distributions. P = probability of derivation from same distribution. Null hypothesis is negated for $P < 0.05$. (A) Geographic distribution of SNB zircon U-Pb crystallization age sample localities. (B) SNB vs. sample SAC_SR_10 (north of Redding). (C) SNB vs. sample SAC_KL_30 (south of Feather River). (D) SNB vs. samples KR_SGR_46. (E) SNB vs. MR_RR_02. (F) SNB vs. CADEL08_2 and CADEL08_3. (G) SNB vs. SUISON, OB20_G, and MSF22_G. (H) SNB vs. 7G9. (I) Histogram and probability density curve of SNB U-Pb zircon ages used in calculations. (J) Histogram and probability density curve of combined U-Pb zircons age distribution for samples CADEL08_2 and CADEL08_3.

discussed later in the paper, this dilution likely results from a significant contrast in zircon concentration/fertility bias against peridotite sources.

A second important observation from the northern Sacramento Valley occurs where the Sacramento River flows past the extensively exposed Mt. Lassen volcanic province (fig. 1). The Lassen Volcanics are mafic–intermediate in composition (Guffanti and others, 1990). The Battle Creek sample (BC-NF-20a) primarily carries *ca.* 500 ka grains associated with Quaternary volcanism near Mount Lassen (Clynne, 1990; Coble and others, 2017) (fig. 5). Although this source is aerially extensive (fig. 1), there is scarce evidence that the volcanic edifice exists in the nearest downstream sample in the Sacramento River. Late Quaternary zircon is completely absent in samples located farther downstream (figs. 3 and 5).

Whole-rock analyses indicate that the *ca.* 500 ka ("Brokeoff phase") of the southern Cascades volcanics contains upwards of 200 ppm Zr (Bullen and Clynne, 1990). Moreover, sediment transported by Battle Creek exclusively drains Lassen Volcanics and yields Zr concentrations greater than 200 ppm. This value is higher than that measured for upstream samples from the Sacramento River (for example, SAC-SR-10; fig. 12). Thus, the most likely explanation for the paucity of Lassen age zircon in Sacramento River sand is that zircon primarily resides in rock fragments or occurs as very small grains (for example, Moecher and Samson, 2006; Sack and others, 2011). This example thus highlights that fine-grained, mafic-to-intermediate volcanic sources extensively exposed within a river catchment can be very poorly represented in the downstream detrital zircon population (figs. 1, 2, and 3). The observation bears significantly upon interpretations of the presence vs. absence and proportions of populations for reconstructing paleogeography and drainage divide migration (Degraaff-Surpless and others, 2002; Moecher and Samson, 2006).

The Sacramento River provenance signature begins to converge to that of the Sierra Nevada batholith south of Tehama (figs. 1, 3, and 5) but remains distinguishable from it below the confluence with the Feather River (fig. 14). It is only within the Sacramento-San Joaquin Delta where the Sacramento, American, Mokelumne, and San Joaquin Rivers all converge where the modern sand detrital zircon provenance signature becomes indistinguishable from the Sierra Nevada batholith (fig. 14).

Sacramento-San Joaquin Delta to the Pacific Ocean.—Tectonic processes including the uplift of the Coast Ranges (Unruh and others, 2007) and development of the modern San Andreas Fault system (Atwater, 1989) have periodically blocked the Central Valley drainage system from reaching the Pacific during the Pliocene and Pleistocene (Sarna-Wojcicki and others, 1985). The most recent blockage occurred during the middle Pleistocene when the fluvial system ponded against the Coast Ranges to form Lake Corcoran, a large lake that covered the central part of the Central Valley including the delta region (Frink and Kues, 1954). Over the past *ca.* 600 ka, differential northwestward displacement of Coast Range blocks along various faults of the San Andreas system have produced a topographic configuration that has permitted an integrated river/estuarine system to flow west through the Coast Ranges to San Francisco Bay and the Pacific Ocean (Sarna-Wojcicki and others, 1985). The present geomorphological disequilibrium character of the broader San Francisco Bay region is caused by fault-produced chokepoints at the Carquinez Straight between Suisun and San Pablo bays, a similar constriction between San Pablo Bay and San Francisco Bay, and at the Golden Gate between San Francisco Bay and the Pacific Ocean (figs. 2 and 3).

Because the drainage network through the Coast Ranges and into San Francisco Bay has apparently only been operative for the past *ca.* 600 ka (Sarna-Wojcicki and others, 1985), the nature of sand transport through this tectonically active area is of great interest. The detrital zircon age distribution measured from sand dredged from Suisan Bay is depleted in Late Cretaceous zircon and enriched in Early Cretaceous and

Jurassic grains relative to the two samples within the Sacramento-San Joaquin Delta region (fig. 6). A similar relationship is exhibited by sands dredged from the Golden Gate dune field immediately offshore of San Francisco Bay (fig. 6). Great Valley group and Franciscan accretionary complex rocks that crop out within the Coast Ranges surrounding the San Francisco Bay area generally contain little Late Cretaceous zircon but are highly enriched in Early Cretaceous and Jurassic grains (fig. 6, Ernst and others, 2009; Snow and others, 2010; Prohoroff and others, 2012) (fig. 6). Hence the change in provenance signature is consistent with significant dilution of Central Valley river sand by material locally eroded from the Coast Ranges and delivered to Suisun Bay by Coast Ranges tributaries such as the Napa River (Rosenbauer and others, 2013; Wong and others, 2013). An aggregated detrital zircon age distribution formed from modern sand samples from Suisun Bay and the Golden Gate dune field is statistically distinct from the Sierra Nevada batholith reference distribution (fig. 14).

Additional data from the late Pliocene-Pleistocene Merced Formation also bear upon this issue. The Merced Formation crops out in a 3 km wide, northwest-southeast trending belt that extends for a distance of 25 km across the northern San Francisco Peninsula (Clifton and Hunter, 1987; Ingram and Ingle, 1998). The Merced trough has been bounded to the southwest by the active segment of the San Andreas Fault over the past *ca.* 1 m.y. (McLaughlin and others, 2007) and has thus captured locally derived sediment in the Bay area. Heavy mineral studies of the Merced Formation indicate that the lower two-thirds of the formation contains sediment derived from local Coast Ranges sources (Hall, ms, 1965). A dramatic change in heavy mineral provenance is reported to occur ca. 100 m below the stratigraphic position of the 500 Ka Rockland tuff (Coble and others, 2017). Abundant fine volcanic rock fragments, hornblende, and other mafic plutonic minerals apparently derived from the Sierra Nevada and the southern Cascade Range characterize the shallowest third of the Merced Formation.

Xiao and Grove (2012) analyzed detrital zircon samples from the erosional base of the Merced Formation (that is atop the Franciscan Complex at Mussel Rock) and at the stratigraphic level of the Rockland tuff. Results for these samples are presented in figure 6. The basal Merced sample contains 17 percent Late Cretaceous, 32 percent Early Cretaceous, and 35 percent Jurassic zircon. Also present are 11 percent Cenozoic grains and 5 percent Proterozoic (fig. 6). The stratigraphically higher sample expected to yield Sierra Nevada provenance also yields 18 percent Late Cretaceous, 34 percent Early Cretaceous, and 46 percent Jurassic zircon along with 2 percent Cenozoic grains (fig. 6). An aggregate age distribution from the two Merced samples is statistically indistinguishable from the San Francisco Bay area modern sands from Suisun Bay and the Golden Gate dune field ($P = 0.32$). As anticipated, the Merced, modern sand from Suisun Bay, and the Golden Gate dune field are distinguished from the composite delta age distribution and the Sierra Nevada batholith reference at 95 percent confidence when the K-S test is applied.

The fact that the Merced Formation is enriched in Early Cretaceous and Jurassic zircon and contains appreciable Cenozoic zircon at its stratigraphically lowest horizons is consistent with an unroofing sequence produced by progressive erosion of the Coast Ranges. This is supported by detrital zircon results reported by Dumitru and others (2013) and Gooley and others (in press) for the Mount Diablo area of the Coast Ranges where Eocene through Miocene strata yield measurable proportions of Eocene, Oligocene, and Miocene zircon in addition to a high percentage of Late Cretaceous grains that is comparable to that yielded by our modern delta samples (fig. 6). As the Coast Ranges are eroded more deeply, Franciscan and Great Valley strata that contain low concentrations of Late Cretaceous zircon begin to contribute more extensively to the sediment load moving through the San Francisco Bay area from the Sacramento-San Joaquin Delta to the Pacific Ocean.

Within the above context, it is interesting to consider the results we obtained from the deep-water slope sample (gravity-core F-8-90-NC-7G9; figs. 3 and 6). The age distribution of this sample is more similar to that of the Sacramento-San Joaquin Delta and the Sierra Nevada reference than any of the modern sand samples from Suisun Bay, and the Golden Gate dune field. Interestingly, it also contains readily detected (8%) Cenozoic zircon. This young zircon coupled with the similarity of the age distribution of F-8-90-NC-7G9 to the Sierra Nevada reference curve (fig. 14) suggests that deposition of F-8-90-NC-7G9 may have occurred early in the development of the river system before the Coast Ranges were as deeply eroded as they are today. Alternatively, the more Sierra Nevada-like provenance signature of F-8-90-NC-7G9 could also be explained by more efficient sand delivery from the delta to the shelf during one of the four major low stands of sea level that have occurred over the past 500 ka (Rohling and others, 1998). A low sea level stand would have promoted a free-flowing river through the San Francisco Bay area and Golden Gate region. Under such conditions, a larger sediment flux from the delta might be expected to be less contaminated by locally derived Coast Ranges sediment than a more sluggish river ponded within the San Francisco Bay area during high stands of sea level (that is, the current situation). While it is also possible that Cretaceous zircon were supplied by local erosion of the Salinian Block west of the San Andreas Fault, this explanation cannot account for Jurassic and Early Cretaceous zircon in the age distribution of F-8-90-NC-7G9 that are not contributed by local Salinian basement such as that exposed on the Farallon Islands (Kistler and Champion, 2001) (fig. 6).

Comparison of the Modern Sands with Cretaceous-Cenozoic Great Valley Sandstones

Compilations of zircon ages from bedrock and detrital samples are commonly used as a means of constraining arc evolution, especially with regard to the evolution of magmatic arcs (for example, Barth and others, 2013; DeCelles and Graham, 2015; Paterson and Ducea, 2015). Cretaceous to Eocene detrital zircon trends have been discussed by Jacobson and others (2011) and Sharman and others (2015) in terms of progressive erosion of the middle Cretaceous batholith and the response of the drainage network to Laramide flat subduction throughout the California arc-forearc system. Detrital zircon data from the Eocene Sacramento Basin are sparse but suggest significant variations in detrital populations between the Eocene and modern manifestations of the basin (fig. 15). The Eocene record of the Sacramento Basin is characterized by a mix of locally derived Jurassic and Cretaceous zircon with extraregionally derived early-to-middle Cenozoic grains from tectonically and volcanically active areas in Idaho and northern Nevada (Dumitru and others, 2013; Gooley and others, in press). Alternatively, the detrital zircon population present within the modern Sacramento Basin is more similar to its Cretaceous counterpart in that it is dominated by Jurassic and Early Cretaceous ages (fig. 15).

The modern San Joaquin Basin differs from the Eocene in that it carries significantly more zircon of Early Cretaceous (135–100 Ma) age at the expense of Late Cretaceous and Jurassic zircon that is more abundant in Eocene rocks (fig. 15). The increase in proportion of Early Cretaceous ages between the Eocene to present in the San Joaquin Basin may be the result of rejuvenated Pliocene–Quaternary rock uplift rates in the southern Sierra Nevada that are believed to be related to removal of mantle lithosphere (Saleeby and others, 2012, 2013).

Mixture Modeling, Sediment Flux, and Zr Concentration

Detrital zircon provenance analysis can only be regarded as a quantitatively rigorous exercise to the extent that a meaningful approach is applied to accurately combine age distributions representing different sources that contribute sediment to a depositional system. The simplest test of mixture modeling for provenance purposes is to predict the

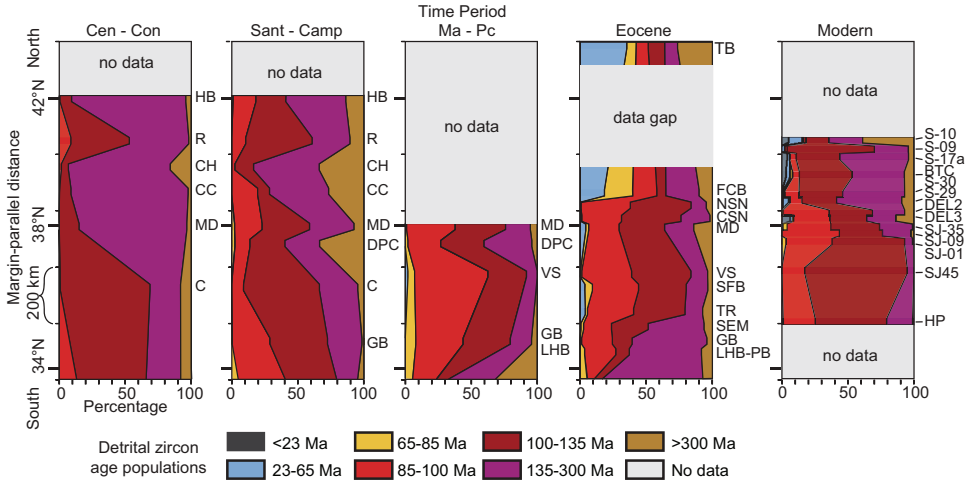

Fig. 15. Spatial and temporal comparison of detrital zircon data from the Central Valley between Late Cretaceous to the present. BTC – SAC-BTC-24; C – Coalinga; CC – Cache Creek; CH – Chico; CSN – Central Sierra Nevada; DPC – Del Puerto Canyon; FCB – Franciscan Coastal belt; GB – Gualala block; HB – Hornbrook basin; LHB – La Honda basin; MD – Mount Diablo; NSN – northern Sierra Nevada; PB – Pilarcitos block; R – Redding; S-09 – SAC-09-RED BLUFF; S-10 – SAC-SR-10; S-17a – SAC-THE-17a; S-30 – SAC-KL-30; SEM – San Emigdio Mountains; SFB – San Francisco Bay; TB – Tyee basin; TR – Transverse Ranges; VS – Vallecitos syncline; (Modified from Sharman and others, 2015).

age distribution that results from pooled sediment contributed by two parent streams. As indicated in the Results section, our efforts to quantitatively model sediment mixing within the Central Valley drainage network produced variable results in that downstream age distributions produced by parent streams could be predicted in only four of seven cases attempted. Below we consider the factors that influenced this outcome.

Variations in Zircon Concentration

Previous studies (for example, Whitmore and others, 2004) have demonstrated that sediment grain size need not intrinsically bias Zr concentrations (and inferred zircon fertility) (fig. 12A). Nevertheless, Zr concentrations measured in this (fig. 12B) and other studies (Amidon and others, 2005a; Moecher and Samson, 2006) document significant local and regional variability in zircon fertility that complicate quantitative modeling of zircon U-Pb age distributions. Collectively, these results highlight the susceptibility of large-scale drainages with lithologically heterogenous sediment routing systems to biased results in zircon provenance studies.

Based upon Zr concentrations (fig. 12A), the concentration of zircon within river sand of the San Joaquin River system is expected to be higher than it is for the Sacramento system (fig. 12B). This reflects derivation of sediment from the granite-dominated southern Sierra Nevada in the San Joaquin Basin relative to the Sacramento Basin (fig. 1). Calc-alkaline plutons such as those that form the Sierra Nevada batholith typically yield sediment with Zr concentrations significantly greater than 100 ppm (Moecher and Samson, 2006). In comparison, the mafic- and ultramafic-dominated Klamath Mountains samples consistently yielded sediment with the zirconium well below 100 ppm (fig. 12B). This bias goes a long way in explaining why there is no readily detectable trace of detrital zircon clearly derived from the Klamath Mountains or Mount Lassen in the Sacramento-San Joaquin Delta (fig. 5).

Relative flux ratios for each of the trunk-tributary mixtures are presented in Table 1. Without direct measurements of bedload from each gauging station, it is difficult to

determine how accurate each calculation is. However, in one example where independent estimates of sediment flux are available, our calculated flux ratio of 4.85 between the Sacramento (CADEL08-2) and San Joaquin Rivers (CADEL08-3) prior to entering Suisun Bay agrees with sediment discharge data collected at nearby gauges. These data indicate that the Sacramento River delivers 5 times more sediment than the San Joaquin River (Wright and Schoellhamer 2005; Schoellhamer and others, 2012). However, when the Sacramento River's higher sediment flux (table 1) is weighted with the overall lower concentration of Zr in its bedload (fig. 12C), the amount of zircon that ends up being contributed to the delta by the Sacramento and San Joaquin Rivers ends up being more equal than would be estimated from sediment load alone.

Hydrodynamic fractionation of zircon during sediment transport.—In addition to zircon fertility variations in source lithology, detrital zircon is also susceptible to hydrodynamic fractionation during sediment transport (Garzanti and Ando, 2007; Lawrence and others, 2011; Ibañez-Mejia, 2018). Samples from the Golden Gate dune field demonstrate that detrital zircons can fractionate and accumulate in fine-grained sediments that yield Zr concentrations greater than 4000 ppm. Although there is a wide range (639 – 4280 ppm) of Zr concentrations, samples generally exceed 1000 ppm of Zr. Therefore, although Zr concentrations may be an appropriate proxy for zircon fertility, extensive sampling is likely required to effectively characterize a system. Consequently, collecting only a single data point for a given source or tributary will likely prove insufficient for quantifying the fertility or concentration of that source. Further research is needed to establish robust methods for characterizing zircon grain concentrations using bulk Zr concentrations of sediment.

Below, we examine two cases that illustrate how well mixing coefficients derived from our calculations reflect the estimated relative flux of sediment.

Confluence of the San Joaquin River with the Tuolumne River.—Figure 13A provides an example of an apparently successful modeling effort (for example where $V_{crit} > V_{max}$). The San Joaquin River downstream of the Tuolumne River (fig. 13A) is well described by a narrow range of mixtures of its parents (~20–50% Tuolumne River). Given the expected variability in relative Zr concentration (C_a/C_b), these mixing coefficients predict the expected relative sand flux of the two input rivers (fig. 13A).

While the mixing coefficients and measured Zr concentrations do reproduce our estimates of the relative flux of parent sources, the predicted flux ratios produced by our calculations can span orders of magnitude. Figure 13A illustrates our most tightly constrained example. This occurs because the primary difference in the age distributions of the two parents is a complementary contrast in the proportions of ~100 to 150 Ma zircon (fig. 13A). In addition, the range of relative Zr concentration (C_a/C_b) is also narrowly constrained in this example to be between ~2 to 3 (fig. 13A). Yet despite this favorable confluence of measured quantities, the model is still not able to predict which of the two known parents contributes a greater flux of sediment (Q_a/Q_b could be either greater or less than unity). This uncertainty exists because the greater contribution of Parent A (SJ_CL_01) needed to 'pull' the cumulative density function (CDF) upward between ages of 100 to 150 Ma is offset by the greater Zr concentration of this parent (fig. 13A). In all other cases we considered, mixing coefficients, and therefore predicted fluxes, were less well constrained.

Confluence of the Sacramento River with Cottonwood Creek.—Figure 13B provides a case where the offspring populations cannot be reproduced from their parents. Despite the apparent failure of the calculations, we suggest that the example provides a case where relative mixing coefficients may still provide useful information. Mixing of the Sacramento River (SAC_SR_10) and Cottonwood Creek (CW40) samples fails to reproduce the offspring (SAC09-RB) in part because the parents contain >250 Ma zircon that is not detected in the offspring. Moreover, the offspring contains >500 Ma zircon that was not

detected in either of the parents (fig. 13B). We speculate that the above-mentioned inconsistencies in the age distributions of samples are likely due to undersampled populations within parent detrital zircon samples (n = 92–115 in this study).

While the failure of the above-mentioned calculations to reproduce the age distribution of the offspring could be resolved by more detailed sampling, it is important not to overlook that the calculation produces a clear and important result when only the <200 Ma portion of the age distributions is considered. Sample SAC09-RB is very well described by CW40, but also needs a small proportion of 0 to 100 Ma ages contained in SAC_SR_10 (fig. 13B). Thus, while the mixing of CW40 and SAC_SR_10 cannot reproduce the overall age distribution of SAC09-RB, the 'better' fits produced by mixture modeling tightly constrain the proportions that CW40 and SAC_SR_10 must contribute. Thus, even in cases where mixing of the parents cannot quantitatively account for the offspring, the modeling process may provide valuable insight. In this case, the example (fig. 13B) drives home the rapid downstream dilution of Klamath-derived detritus in the Sacramento River by tributaries that feed into the main river trunk.

In summary, successful modeling of sediment mixing in modern systems requires considerably more sampling and/or analyses to characterize the detrital zircon age distributions carried by the contributing streams and to assess the extent of downsediment homogenization. Accurate long-term measures of sediment flux are needed as well as a robust method to assess zircon concentration. All of the important tributary inputs must be characterized. While these steps can generally be taken in modern systems, it is much more difficult to know how to implement them in ancient systems where sampling opportunities are limited by available exposures.

Inferring relative sediment flux on the basis of mixing coefficients shows promise, but uncertainty in best-fit mixing coefficients and zircon concentration result in relatively imprecise relative Qs predictions (table 1). Additional research is needed to assess the best methods for determining zircon concentration in modern rivers, including the variability in Zr concentration in sediment that can occur at local scales. Additionally, more direct means of determining bedload sediment flux would allow for tighter constraints on how well flux ratios can predict Zr concentration and vice versa. Additional challenges are faced by studies of ancient sediments, for which records of source-area zircon fertility are not available but could significantly impact preserved zircon populations (for example, due to the presence of high-Zr granitoids) (Moecher and Samson, 2006; Samson and others, 2018).

Downstream Propagation vs. Dilution of Provenance Trends in the Mud Fraction

Given that geochemical trends of the clay and silt fraction from second and third order drainages are generally expected to represent the composition of their respective source regions, it is of interest to assess how the provenance signature of the mud fraction varies throughout the Central Valley drainage network. Regional scale plots of Th/Sc to Zr/Sc (fig. 9), Sc to V (fig. 10), and REE fractionation trends (fig. 11) all reflect the progressive north-south and east-west variations in arc dissection and crustal composition (mafic vs. felsic) predicted from figure 1.

Along-stream variation of the trace element composition of river mud is best addressed in the northern part of the Sacramento River. Trace element measurements of Cr and Ni from shales and mudstones have been employed to detect ultramafic source regions within ancient systems (Bhatia, 1983; McLennan and others, 1993; Draut and Clift, 2001; Clift and others, 2005). Our results from the northern Sacramento River system suggest that the utility of this approach should be viewed with caution. For example, greatly elevated concentrations of chromium and nickel are observed in river mud from the Klamath Mountain region (fig. 8A). However, the concentrations of Cr and Ni abruptly drop to regional background levels in river mud samples south of Redding. River mud sampled south of Redding consistently yields Cr

and Ni values that cluster around 100 ppm regardless of whether they were sampled from the Sacramento or San Joaquin Basins (fig. 8A). The rapid dilution of these trace elements from their Klamath Mountains source parallels the dilution seen in Klamath detrital zircon south of Redding (fig. 5).

The apparent rapid dilution of Cr and Ni in Sacramento River mud could be an anthropogenic artefact produced by Shasta Dam. Shasta reservoir sequesters a considerable quantity of fine-grained sediment. However, as previously discussed, sediment available downstream of the dam should still represent upstream sources. This is evident in the detrital zircon trends (mainly Paleozoic sources) observed in sand that were able to propagate south of the Shasta Dam as they are likely available for recycling in downstream Holocene deposits.

Insights into downstream dilution of trace element concentrations can also be addressed with data available from the Cretaceous Great Valley group (Surpless, 2014). Figure 8B shows that the highest concentrations of Cr and Ni from Cretaceous strata occur within the Early Cretaceous sector of the Great Valley group. This is a sensible result given the more abundant mafic and ultramafic sources in the Klamath Mountains and northern Sierran foothills relative to the San Joaquin Basin (Surpless, 2014). However, figure 8B also shows that higher concentrations of Cr and Ni decrease in Late Cretaceous shale from the Sacramento sector of the Great Valley group to values that are similar to modern levels.

Interestingly, the opposite trend occurs in the San Joaquin sector of the Great Valley group. Early Cretaceous Cr and Ni concentrations are lower than the values measured for Late Cretaceous strata while modern Cr and Ni concentrations are the highest. Collectively, these relationships suggest that Cr and Ni produced by exhumation and erosion of the granitic Sierra Nevada batholith has swamped out signals derived from other sources.

Other trace element results suggest relatively small changes in the geochemistry and lithology of Central Valley sources since the Late Cretaceous. For example, figure 9B shows that there has been a subtle decrease in Th/Sc relative to Zr/Sc between Cretaceous shales and modern river mud in the Sacramento sector. Alternatively, both Th/Sc and Zr/Sc have systematically increased over time in the San Joaquin sector with the greatest change occurring between the Early and Late Cretaceous (fig. 9B). Variation of V relative to Sc over time exhibits a somewhat different relationship (fig. 10). In the Early Cretaceous, Values of V and Sc are highest in both the Sacramento and San Joaquin sectors. In the Late Cretaceous, the two basins differentiate with respect to the concentrations of V and Sc. Concentrations of these elements remain high in the Sacramento sector of the Central Valley basin while those in the San Joaquin sector of the Central Valley decline. We interpret this as a differentiation in the amount of volcanic input (Surpless, 2014). This likely reflects greater denudation of the southern Sierra Nevada and elimination of the coeval volcanic cover (Saleeby and others, 2013). Finally, differentiation between the Sacramento and San Joaquin Basins is readily apparent in the modern system as a result of development of the Cascades volcanic arc at the northern end of the Central Valley forearc basin (fig. 10).

CONCLUSIONS

The geochemical and detrital zircon provenance trends that we have documented in modern river sediment from California's Central Valley demonstrate that different provenance techniques, applied to sand and mud facies, are able to record downstream propagation and/or dilution of source region provenance to varying degrees. We conclude the following:

(1) Where variations in lithology (and thus zircon fertility) are minimal, detrital zircon provenance trends clearly propagate and effectively record sources and tributaries (for example, the San Joaquin River system).

(2) In contrast, spatially extensive exposures of low zircon fertility ultramafic and mafic rocks within the southeastern Klamath Mountains are poorly represented or entirely missing from detrital zircon age distributions along the Sacramento River. For example, zircon-rich sand carried by a minor tributary (Cottonwood Creek) overwhelms the zircon age distribution carried by the bed load of the main Sacramento River trunk near Red Bluff, roughly 125 km downstream of Shasta Dam. Similarly, elevated concentrations of Ni and Cr contained within fine-grained sediment eroded from ultramafic rocks of the Klamaths are rapidly diluted to regional concentrations a short distance away from the Klamath source.

(3) Mafic volcanic sources with widespread spatial distribution are also underrepresented downstream. For example, a tributary (Battle Creek) draining Mount Lassen of the Cascade volcanic arc is dominated by *ca.* 500 Ma zircon. However, when Battle Creek enters the Sacramento River, the 500 ka age component is rapidly diluted downstream. In contrast with the Klamath Mountains case, however, evidence of the existence of the mafic to intermediate Lassen Volcanics is propagated downstream in measurements of vanadium vs. scandium acquired from river mud samples.

(4) Two samples collected within the Sacramento-San Joaquin Delta at the confluence of the San Joaquin, Mokelumne, American, and Sacramento Rivers yield a pooled detrital zircon U-Pb age distribution that is statistically indistinguishable at 95 percent confidence from the distribution of crystallization ages independently measured from the composite Sierra Nevada batholith (n= 554; Chapman and others, 2012). In contrast, samples collected along either the Sacramento or San Joaquin Rivers generally fail K-S test comparisons with the model Sierra Nevada batholith age distribution.

(5) The present course of the merged river from the delta to the Pacific is thought to have been active only over the past *ca.* 600 ka. Detrital zircon age distributions measured from samples dredged at Suisun Bay, the Golden Gate dune field, and on the continental shelf are enriched in Early Cretaceous and Jurassic zircon that appears to have been locally eroded from Franciscan Complex and other Early Cretaceous rocks of the Coast Ranges. Similar age distributions measured for the Tertiary–Quaternary Merced Formation on the San Francisco Peninsula appear to be reworked from the Franciscan Complex and younger Coast Ranges strata.

(6) Measurements of Zr concentration from fine-grained sediments dredged from Suisun Bay and San Pablo Bay (50–500 ppm) are much lower than those found in the higher energy Golden Gate dune field (San Francisco bar) outboard of San Francisco Bay (up to 4000 ppm). These relationships document complex sediment processing as sediment is transported from San Francisco Bay to the continental slope.

(7) The detrital zircon age distribution measured from a piston-core sample from the continental slope yields a Sierra Nevada batholith-like age distribution that also includes appreciable Cenozoic zircon apparently derived from erosion of Coast Ranges strata. The distinct character of this sediment's age distribution relative to those measured from the San Francisco Bay area can be explained by deposition during the early stages of an unroofing sequence that preferentially reworked Cenozoic Coast Ranges strata that more strongly resemble the Sierra Nevada batholith than the underlying Franciscan Complex. Alternatively, more efficient sediment transport from the Sacramento-San Joaquin Delta to the Pacific Ocean enabled by a free-flowing river to the

Pacific Ocean during a low-stand of sea level could have largely preserved the Sierra Nevada batholith provenance signature.

(8) We performed mixture modeling from seven tributary-trunk river combinations in the Central Valley. Independent stream-gauge-derived predictions of relative bedload flux were used to assess differences in zircon concentration based on measurements of zirconium concentration from river mud samples. In all cases, our median estimate is within an order of magnitude of the predicted relative bedload flux. However, uncertainties in the best mixture coefficients and the observed zirconium concentration yield a wide range of relative sediment flux predictions, many of which are well outside expected ranges. In addition, "best-fit" mixture models do not provide a satisfactory description of the observed downstream population for a significant fraction of tributary-trunk combinations. At best, results from this study suggest that mixture modeling of detrital geochronologic data coupled with a statistically robust quantification of source lithology (zircon fertility) can provide a reasonable approximation of relative sediment flux within drainages.

(9) Continuing efforts to better quantify zircon concentration, assess the potential influence of hydrodynamic fractionation, and measured bedload will lead to improved reconstruction of relative sediment flux in modern and possibly ancient sediment routing systems.

ACKNOWLEDGMENTS

We thank Jeremy Hourigan and the University of California Santa Cruz (UCSC) as well as George Gehrels, Mark Pecha, and staff at the Arizona Laserchron Center for assistance with U-Pb detrital zircon LA-ICPMS analyses. We also acknowledge Charles Knaack, Laureen Wagoner, Richard Conrey and the rest of the staff at the Washington State GeoAnalytical Laboratory for help with geochemical analyses. Trevor Dumitru contributed significantly with heavy mineral separations, zircon mount preparation, data acquisition at UCSC, and through many fruitful discussions. We thank Renee Takesue and Patrick Barnard for providing access to sediment geochemistry data from the San Francisco Bay region. Funding sources for this work include the industrial affiliates of the Stanford Project on Deep-water Depositional Systems as well as the McGee–Levorsen Graduate Research Grants awarded to Malkowski. Reviews by Kathy Surpless, Ray Ingersoll, Bob McLaughlin, and Associate Editor John Garver resulted in significant improvements to the manuscript. Any use of trade, firm, or product names is for descriptive purposes only and does not imply endorsement by the U.S. Government.

APPENDIX 1

We characterize "offspring" distributions of U-Pb dates, D, from the Sacramento and San Joaquin Rivers and their confluence as a weighted sum of inputs from their immediate upstream reaches and tributaries (the 'parents', P_a and P_b, Amidon and others, 2005b

$$D = \phi_a P_a + \phi_b P_b. \quad (1)$$

We determine the mixing coefficients, ϕ_a and ϕ_b, by minimizing the V_{max}, a measure of the separation between cumulative distribution functions (Saylor and Sundell, 2016), computed between the observed offspring and the mixed 'parents', under the constraints that the mixing coefficients must each be between 0 and 1 and sum to unity ($\phi_b = 1 - \phi_a$, Amidon and others, 2005b). The distributions of zircon U-Pb dates we estimate from samples of $\sim 10^2$ grains are not perfect records of the true distribution of zircon ages in a stream, a different collection of $\sim 10^2$ grains from the same sample would likely yield a slightly different distribution. To characterize how the uncertainty

in mixing coefficients results from these sampling effects, we calculate a distribution of mixing coefficients with a random sampling procedure, bootstrapping, using an approach similar to that of Sundell and Saylor (2017). In each of 10,000 iterations, we construct synthetic distributions by resampling with replacement the zircon U-Pb dates from the parent and offspring samples. For each synthetic distribution, we recompute the minimum V_{max} and associated mixing coefficients. We highlight agreement between the modelled offspring mixture and observed offspring by plotting the intervals that bound 95% of the mixed synthetic distributions.

Our bootstrapping procedure produces an uncertainty estimate on the best-fitting mixture coefficients, a range of the proportions of parent distributions that when combined most closely represent an offspring distribution. However, the best mixing coefficients do not necessarily provide a satisfactory description of the observed offspring distribution. We characterize 'good' fits with the value V_{crit}. V_{crit} is intended to assess how large V_{max} may get due to random sampling from the same distribution and is again defined through a bootstrapping procedure. In each of 10,000 iterations, we resample with replacement two copies of the same offspring distribution, compute the V_{max} between these copies, and then assign V_{crit} to be the 95th percentiles of these values.

We are rarely interested in the relative contribution of detrital zircon ages the mixing coefficients provide, but instead an estimate of the relative sediment contributions of different sources. We describe the contribution of zircon from a stream, ϕ_a, as the product of its sediment flux, $Q_a[L^3t^{-1}]$, and the concentration of zircon grains in that flux, $c_a[L^{-3}]$,

$$\phi_a = c_a Q_a. \tag{2}$$

The ratio of fluxes is then inversely proportional to the ratio of zircon concentration:

$$\frac{Q_a}{Q_b} = \frac{c_b \phi_a}{c_a \phi_b}. \tag{3}$$

Estimating the Relative Flux of Parent Tributaries

When combined with knowledge of zircon concentrations, the mixture model theoretically provides estimates of relative sediment flux, but independent measures of sediment flux are rarely available to compare with these estimates. We attempt to evaluate the mixture model derived relative flux estimates using U.S. Geological Survey (USGS) gauging station data and an empirical sediment transport relation. In constructing a prediction for Q, it is not our intention to be able to predict perfectly the sediment flux. Rather, we seek to be able to construct a reasonable estimate for the ratio of sediment flux a river received from two upstream tributaries as a means of comparison to mixture modeling. We acknowledge that the parameters and sets of equations we have chosen for these individual relations likely provide inadequate descriptions of individual natural systems. However, we believe that the ratio of fluxes obtained from this approach provides a useful estimate of the relative transport capacity of two parent reaches given the history of streamflow observed from each.

For simplicity, we focus on the relative contribution of sediment from bedload and estimate sediment transport with the Meyer-Peter-Mueller (1948) bedload transport equation,

$$q^* = C(\tau^* - \tau_c^*)^b, \tag{4}$$

where q^* is the dimensionless volume bed-load transport rate per unit channel width, τ^* is the dimensionless boundary shear stress acting on the bed, τ_c^* is the critical Shields number, and C and b are empirically derived coefficients. Following Wong and Parker

(2006), we use 4.93, 1.6, and 0.047 for C, b, and τ_c^*, respectively. We relate q^*, the dimensionless flux per unit bed area, to the total flux for a channel, q [L^3t^{-1}] with

$$q = Wq^*D\sqrt{Dg\left(\frac{\rho_s}{\rho_f} - 1\right)} \tag{5}$$

Here, W [L] is the width of the channel, D [L] is the diameter of sediment grains (here, 0.2 mm), g [L^2t^{-1}] is the acceleration due to gravity, and $\rho_{s,f}$ [ML^{-3}] are the densities of sediment and water (here 1,000 and 2,650 kg/m^3, respectively). We estimate τ^* from USGS gauging stations that report channel area, WH [L^2], channel width, W [L], and velocity U [Lt^{-1}] as

$$\tau^* = \frac{\tau_b}{Dg(\rho_s - \rho_f)}. \tag{6}$$

The basal shear stress, τ_b, is related to velocity by way of a coefficient of friction, C_f (Chaudhry, 2008),

$$\tau_b = \rho_f C_f U^2. \tag{7}$$

We estimate C_f with a form of the Manning-Strickler relation (Parker, 1991),

$$C_f^{-\frac{1}{2}} = \alpha_r\left(\frac{H}{n_k D_{s90}}\right)^{\frac{1}{6}}. \tag{8}$$

We take $H = WH/W$, where WH is the cross-sectional area reported in the USGS gauging station data at a given day. We take n_k as 2 following Kamphuis (1974) and from the observation that most samples were collected from sand-bedded streams, we use 0.4 mm for the 90th percentile of surface sediment (D_{s90}). For simplicity, we use a constant value of α_r of 8.1; this value was suggested by Parker (1991) for gravel-bed streams, which is not strictly accurate for all streams in this study, but provides a starting point for our comparison of relative flux.

The different gauging stations used here record observations of streams at different intervals and for different duration. In addition, different streams spend different durations of time at flow stages so low no transport occurs. To account for these effects, we integrate fluxes calculated over the course of a year and characterize the potential variability in the relative flux by randomly resampling a yearly series of daily discharges. We again use a bootstrapping procedure with 5,000 iterations to characterize the uncertainty in flux estimates derived from gauge measurements, particularly for those stations with a sparse record of gauging. In each iteration, we resample with replacement the gauge station record and from this resampled record construct a kernel density estimate of log-transformed τ^* values. We then draw 365 samples from this kernel density estimate, assigning each a width based on a nearest-neighbor interpolation between values of τ^* and channel width. We sum the fluxes estimated from these 365 τ^* and W pairs as an estimate of the yearly flux and compare these yearly estimates of sediment flux from parent tributaries. (See Appendix 2 for a detailed description of this procedure, http://earth.geology.yale.edu/%7eajs/SupplementaryData/2019/Malkowski)

APPENDIX 2

ANALYSIS OF USGS GAUGING STATION MEASUREMENTS

Gauging station data from different tributaries provide highly variable characterizations of the channel flow parameters necessary to characterize τ^* (fig. A2-1). Some stations have long records with decadal gaps, neighboring stations are rarely sampled at the same time and often at very different intervals, and in general large gaps are

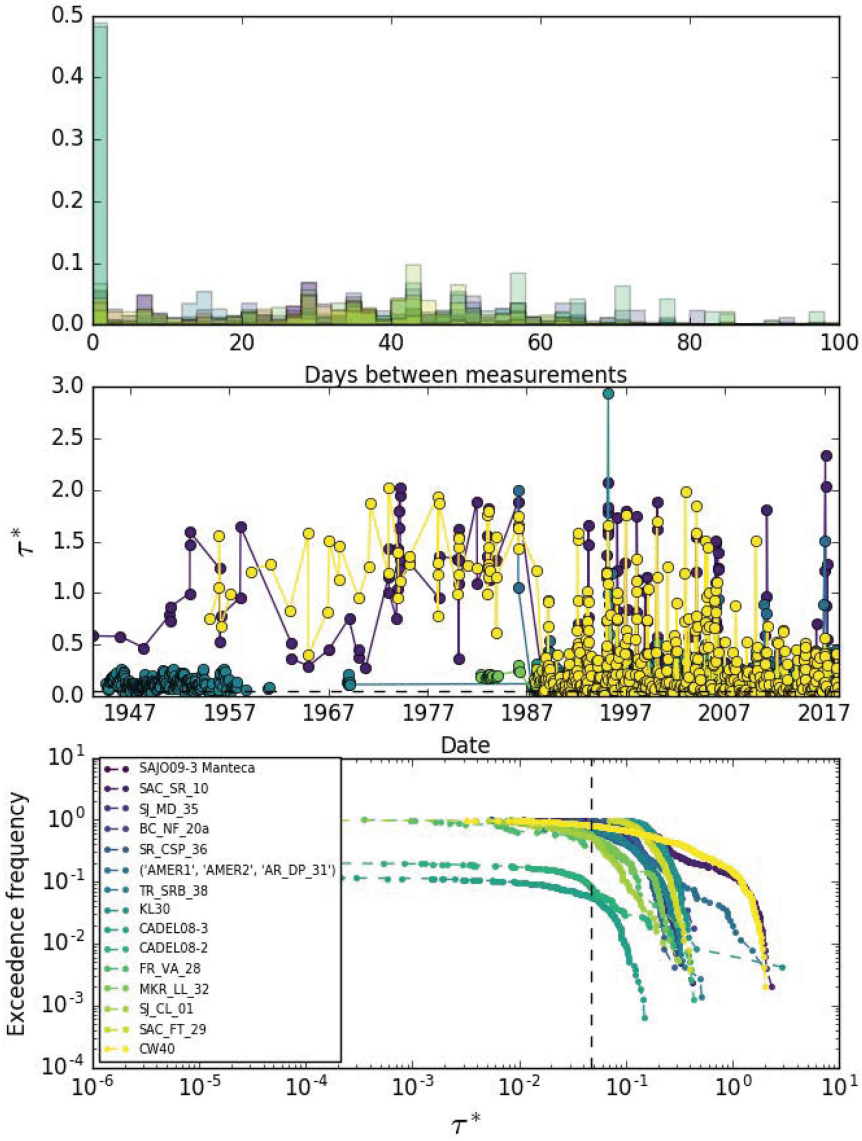

Fig. A2_1. Observations from US Geological Survey Gauging Stations. Top panel shows histograms of the sampling interval at individual gauge sites, highlighting that some stations have much more frequent observations than others. Middle panel shows the time series of computed τ^* values, highlighting the differences in the length of recorded observations and the large gaps present in some systems. Bottom panel shows how often observations of τ^* exceed a given value in the datasets. Dashed black lines in middle and bottom panels highlight τ_c^*.

present in all the hydrographs. In addition, different stations spend different proportions of time above the stage necessary for transport so on any given day the ratio of fluxes may be zero or infinite despite the fact that both streams contribute sediment over longer periods of time (fig. A2-1). To address these issues we compute a series of annual average fluxes from each parent stream by sampling from a probability distribution of τ^* values determined for each stream (fig. A4-2). We estimate probabil-

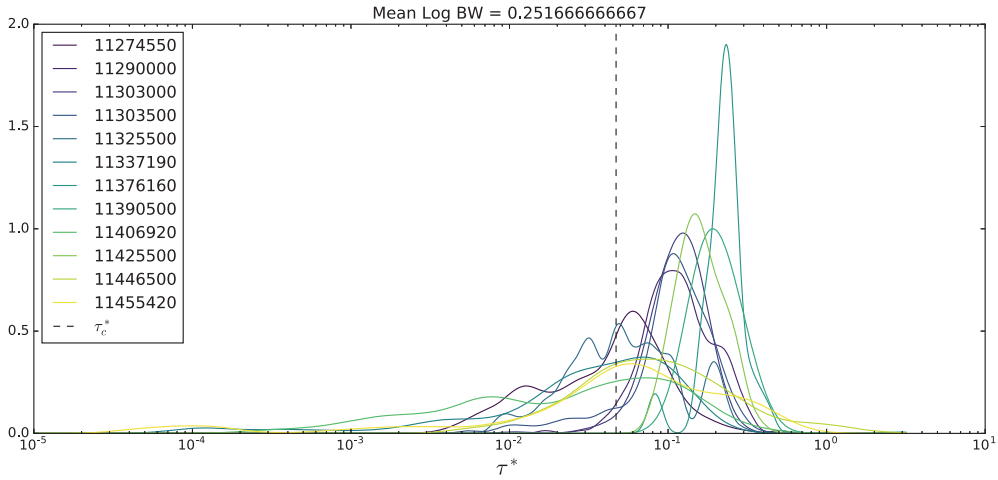

Fig. A2_2. Kernel density estimates of τ* for each parent stream. Vertical black line shows τ_c*. We used an adaptive KDE bandwidth in these examples, but rely on the mean, log bandwidth of 0.25 when constructing flux predictions.

ity distributions from kernel density estimates (KDE) of log-transformed τ*, which we construct with a gaussian kernel with a 0.25 (log-transformed) bandwidth. This was the mean of the best bandwidths determined from a search for the optimal bandwidth (VanderPlas, 2016). We drew 365 samples from these probability distributions of daily τ* measurements, used them to calculate *q*, and summed these 365 values to estimate the flux for a year. We repeated this process 10,000 times; reconstructing the probability distribution of τ* each time by resampling the original measurements with replacement (in this way we hope to characterize the greater uncertainty associated with sparse stream records).

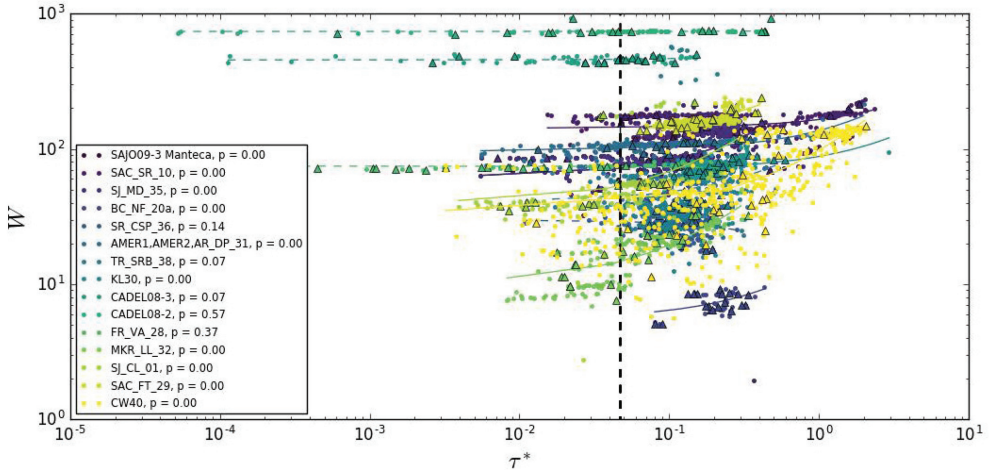

Fig. A2_3. Relationship between τ* and W for the parent streams. Dashed and solid lines show linear regression to the data, and are plotted as solid when the p value for the hypothesis that slopes are 0 was less than 0.05. Twenty small triangles associated with each dataset show a random sample of τ* drawn from KDE of probabilities (fig. A4_2) and assigned a value of W based on nearest neighbor sampling.

To compute q for each river we must account for the rivers width, W. The widest rivers show values of W that are essentially invariant with τ^*, but this is not the case for the smallest rivers (fig. A2-3). To account for the correlations between τ^* and W and the noise present in the data we assign a value of W to each random sample of τ^* drawn from the KDE of probability based on a nearest neighbor interpolation (fig. A-4-3). We plot the histogram of the ratios of the 10,000 random estimates of flux for the two parents as a point of comparison with mixing coefficients and relative Zr concentrations.

APPENDIX 3

U-Pb Zircon Geochronology by LA-ICPMS at the University of Arizona Laserchron Center

(Also available at www.laserchron.org)

Zircon separates were obtained from each sample for U-Pb geochronology following standard heavy mineral separation procedures of crushing, grinding, Gemini table, Frantz magnetic separation, and heavy liquids. A large fraction of the zircon grains (100's to 1000's) were mounted in epoxy with a Sri Lanka (SL) zircon standard. Mounts were sanded, polished, imaged, and cleaned prior to isotopic analysis.

U-Pb geochronology of zircons was conducted by laser ablation multicollector inductively coupled plasma mass spectrometry (LA-MC-ICPMS) at the Arizona LaserChron Center (ALC) (Gehrels and others, 2006, 2008). The analyses involve ablation of zircon with a New Wave UP193HE Excimer laser using a spot diameter of 30 microns. The ablated material is carried in helium into the plasma source of a Nu HR ICPMS, which is equipped with a flight tube of sufficient width that U, Th, and Pb isotopes are measured simultaneously. All measurements are made in static mode, using Faraday detectors with 3x1011 ohm resistors for ^{238}U, ^{232}Th, ^{208}Pb-^{206}Pb, and discrete dynode ion counters for ^{204}Pb and ^{202}Hg. Ion yields are ~0.8 mv per ppm. Each analysis consists of one 15-second integration on peaks with the laser off (for backgrounds), 15 one-second integrations with the laser firing, and a 30 second delay to purge the previous sample and prepare for the next analysis. The ablation pit is ~15 microns in depth.

For each analysis, the errors in determining ^{206}Pb/^{238}U and ^{206}Pb/^{204}Pb result in a measurement error of ~1-2% (at 2-sigma level) in the 206Pb/238U age. The errors in measurement of ^{206}Pb/^{207}Pb and ^{206}Pb/^{204}Pb also result in ~1–2% (at 2-sigma level) uncertainty in age for grains that are >1.0 Ga, but are substantially larger for younger grains due to low intensity of the 207Pb signal. For most analyses, the cross-over in precision of ^{206}Pb/^{238}U and ^{206}Pb/^{207}Pb ages occurs at ~1.0 Ga. ^{204}Hg interference with ^{204}Pb is accounted for measurement of ^{202}Hg during laser ablation and subtraction of ^{204}Hg according to the natural ^{202}Hg/^{204}Hg of 4.35. This Hg correction is not significant for most analyses because our Hg backgrounds are low (generally ~150 cps at mass 204). Common Pb correction is accomplished by using the Hg-corrected ^{204}Pb and assuming an initial Pb composition from Stacey and Kramers (1975). Uncertainties of 1.5 for ^{206}Pb/^{204}Pb and 0.3 for ^{207}Pb/^{204}Pb are applied to these compositional values based on the variation in Pb isotopic composition in modern crystal rocks.

Inter-element fractionation of Pb/U is generally ~5%, whereas apparent fractionation of Pb isotopes is generally <0.2%. In-run analysis of fragments of a large zircon crystal (generally every fifth measurement) with known age of 563.5 ± 3.2 Ma (2- sigma error) is used to correct for this fractionation. The uncertainty resulting from the calibration correction is generally 1-2% (2-sigma) for both ^{206}Pb/^{207}Pb and ^{206}Pb/^{238}U ages. Concentrations of U and Th are calibrated relative to our Sri Lanka zircon, which contains ~518 ppm of U and 68 ppm Th. Uncertainties shown at the 1-sigma level, and include only measurement errors. Analyses that are >20% discordant (by comparison of ^{206}Pb/^{238}U and ^{206}Pb/^{207}Pb ages) or >5% reverse discordant (in italics) are not considered Further.

APPENDIX 4

ANALYTICAL METHODS FOR ICP-MS ANALYSES OF MUD AND SAND SAMPLES TAKEN DIRECTLY FROM THE WASHINGTON STATE GEOANALYTICAL FACILITIES WEBPAGE AT:

https://environment.wsu.edu/facilities/geoanalytical-lab/technical-notes/

ICP-MS METHOD

Trace Element Analyses of Rocks and Minerals by ICP-MS

Introduction.—Inductively coupled plasma-mass spectrometry (ICP-MS) is well established as a rapidand precise method for the determination of the rare earth elements (REEs) and trace elements in geologic samples – Lichte and others, (1987), Jarvis (1988), Longerich and others, (1990). However, complete sample digestion is required for accurate results. Mixed acid open-vial digestions on a hotplate work well for basaltic and most ultramafic samples, but may fail to completely decompose many trace mineral phases found in more silicic samples. These resistant phases, such as zircon, garnet, and tourmaline, may contain a significant percentage of the total trace elements in a given sample. High-pressure bombs are effective at achieving complete digestion, but are cumbersome, slow, and labor intensive. Fusion with a flux may require large dilutions to avoid unacceptably high levels of total dissolved solids. We have developed a combination fusion-dissolution method that effectively decomposes refractory mineral phases and removes the bulk of unwanted matrix elements. The procedure consists of a low-dilution fusion with di-Lithium tetraborate followed by an open-vial mixed acid digestion. This method allows us to analyze 14 REEs and 13 additional trace elements in a wide range of geologic samples without having to make assumptions as to the presence or absence of resistant mineral phases. The dissolution with HF after the Lithium-tetraborate fusion quantitatively removes silica and more than 90% of the flux as gaseous fluorides, leaving clear, stable solutions for analysis on the ICPMS.

Experimental.—The Flux used for the fusion is di-Lithium-tetraborate (Spectromelt® A-10, EM Science, Gibbstown, NJ). Reagents are HNO3 69-70% (Fisher ACS plus grade), HF 48-52% (Baker ACS reagent grade), HClO4 67-71% (Fisher Trace Metal Grade), and H2O2 (Baker ACS Reagent). The HF is further purified before use by sub-boiling distillation in a teflon still. All water used is >18 M deionized water from a Nanopure analytical grade water system (Barnstead/Thermolyne). Powdered samples are mixed with an equal amount of lithium tetraborate flux (typically 2g), placed in a carbon crucible and fused at 1000 °C in a muffle furnace for 30 minutes. After cooling, the resultant fusion bead is briefly ground in a carbon-steel ring mill and a 250 mg portion is weighed into a 30 ml, screw-top Teflon PFA vial for dissolution. The acid dissolution consists of a first evaporation with HNO3 (2ml), HF (6 ml), and HClO4 (2 ml) at 110 °C. After evaporating to dryness, the sample is wetted and the sides of the vial are rinsed with a small amount of water before a second evaporation with HClO4 (2 ml) at 160 °C. After the second evaporation, samples are brought into solution by adding approximately 10 ml of water, 3 ml HNO3, 5 drops H2O2, 2 drops of HF and warmed on a hot plate until a clear solution is obtained. The sample is then transferred to a clean 60 ml HDPE bottle diluted up to a final weight of 60g with de-ionized water. Solutions are analyzed on an Agilent model 4500 ICP-MS and are diluted an additional 10X at the time of analysis using Agilent's Integrated Sample Introduction System (ISIS). This yields a final dilution factor of 1:4800 relative to the amount of sample fused. Instrumental drift is corrected using Ru, In, and Re as internal standards. Internal standardization for the REEs uses a linear interpolation between In and Re after Doherty (1989) to compensate for massdependant differences in the rate and degree of instrumental drift. Isobaric interference of light rare earth oxides on the mid- heavy REEs can be a significant source of error in ICP-MS analysis, so tuning is optimized to keep the CeO/Ce ratio below 0.5%. Correction factors used to compen-

sate for the remaining oxide interferences are estimated using two mixed-element solutions. The first contains Ba, Pr, and Nd, and the second Tb, Sm, Eu, and Gd. Standardization is accomplished by processing duplicates of three in-house rock standards interspersed within each batch of 18 unknowns. Concentrations, oxide- and drift corrections are then calculated offline using a spreadsheet.

Results.—Long term precision for the method is typically better than 5% (RSD) for the REEs and 10% for the remaining trace elements. Analyses of USGS and international rock standards show good agreement with consensus values. (Table 1).

APPENDIX 5

TABLE A5_1

Detrital Zircon samples from the Central Valley and San Francisco Bay Region

Sample_ID	Unit	Latitude	Longitude	# Grains	Lab
SAC_SC_8	Sacramento River (Slate Creek)	40.9746	-122.4291	92	UC Santa Cruz
SAC_SR_10	Sacramento River (South Redding)	40.5406	-122.3605	98	UC Santa Cruz
SAC09 RB	Sacramento River	40.2620	-122.2220	97	LaserChron (UofA)
SAC_TEH_17a	Sacramento River (Tehama Bridge)	40.0282	-122.1179	100	UC Santa Cruz
BTC24	Sacramento River	39.4644	-121.9931	98	UC Santa Cruz
KL30	Sacramento River (Knight's Landing)	38.8531	-121.7257	100	UC Santa Cruz
SAC_FT_29	Sacramento River (I-5 bridge)	38.6722	-121.6240	99	UC Santa Cruz
CADEL08-2	Sacramento River	38.1701	-121.6694	115	LaserChron (UofA)
CW40	Cottonwood Creek	40.3771	-122.2839	100	UC Santa Cruz
BC_NF_20a	Battle Creek (north fork)	40.4476	-121.8677	99	UC Santa Cruz
FR_VA_28	Feather River (before Sacramento)	38.7879	-121.6227	97	UC Santa Cruz
AR_DP_31	American River (Discovery Park)	38.6016	-121.5038	97	UC Santa Cruz
AMER1	American River (near confluence with Sac)	38.5983	-121.5068	56	LaserChron (UofA)
AMER2	American River (upstream from I-5 bridge)	38.6004	-121.5037	58	LaserChron (UofA)
SJ_FR_45	San Joaquin River	36.9922	-119.7142	98	UC Santa Cruz
MR_RR_02	San Joaquin River (Merced Bridge)	37.3507	-120.9625	94	UC Santa Cruz
SJ_CL_01	San Joaquin River (Crow's Landing)	37.4302	-121.0142	100	UC Santa Cruz
SAJO09-3	San Joaquin River	37.6400	-121.2170	101	LaserChron (UofA)
SJ_MD_35	San Joaquin River (West of Manteca)	37.7882	-121.3076	100	UC Santa Cruz
CADEL08-3	San Joaquin River	38.0196	-121.7511	112	LaserChron (UofA)
KR_SGR_46	King's River	36.6995	-119.5108	99	UC Santa Cruz
TR_SRB_38	Tuolumne River	37.6028	-121.1310	100	UC Santa Cruz
SR_CSP_36	Stanislaus River	37.6941	-121.1810	100	UC Santa Cruz
MKR_LL_32	Mokolumne River (Lodi Lake)	38.1501	-121.2961	99	UC Santa Cruz
Suisun Bay	Suisun Bay	38.0690	-122.0050	95	LaserChron (UofA)
OB20-G	Golden Gate submarine dune field	37.8072	-122.5058	96	LaserChron (UofA)
MSF22-G	Golden Gate submarine dune field	37.8072	-122.5058	97	LaserChron (UofA)
G686970	Offshore SF Bay (Shelf)	37.6780	-122.6665	93	UC Santa Cruz
X7G9	Offshore SF Bay (Upper slope)	37.4113	-123.0790	99	UC Santa Cruz
Hart Park	Kern River	35.4521	-118.9084	107	LaserChron (UofA)

Samples with borders are presented as combined data in this study.

APPENDIX 6

http://earth.geology.yale.edu/%7eajs/SupplementaryData/2019/Malkowski

APPENDIX 7

Table A7_1

Central valley normalized major element results (weight %) by XRF with sample locations

Sample ID	Lat	Lon	type	SiO_2	TiO_2	Al_2O_3	FeO*	MnO	MgO	CaO	Na_2O	K_2O	P_2O_5	LOI 900 (%)	LOI 550 (%)	Total
ML-1A	41.19122	-122.51098	mud	68.01	0.379	12.74	5.38	0.086	6.50	5.00	1.32	0.36	0.236	4.73	12.86	17.59
ML-1B	41.19122	-122.51098	mud	69.63	0.417	13.47	4.93	0.080	4.96	4.49	1.32	0.48	0.218	4.41	15.44	19.85
GL-3	41.21173	-122.51187	mud	58.12	0.386	8.70	8.48	0.142	19.64	2.44	1.14	0.76	0.196	6.45	16.48	22.93
GL-4-W	41.21173	-122.51187	mud	54.12	0.396	9.10	8.33	0.114	23.59	2.99	0.85	0.42	0.106	6.45	4.49	10.94
EC-5	41.40755	-122.43223	mud	55.96	0.517	11.30	12.43	0.264	14.62	2.90	1.40	0.48	0.129	4.68	12.42	17.10
EC-6	41.40755	-122.43223	mud	56.24	0.492	11.37	12.54	0.285	14.60	2.55	1.33	0.47	0.120	5.22	11.17	16.39
SAC-SC-8	40.97458	-122.42908	mud	53.82	0.527	13.85	9.97	0.274	16.32	2.99	1.44	0.67	0.145	5.89	6.58	12.47
SAC-SC-8-W	40.97458	-122.42908	mud	54.26	0.550	13.55	11.16	0.266	14.75	3.20	1.45	0.65	0.170	5.11	4.27	9.38
SAC-SR-9-W	40.54063	-122.36052	mud	60.31	0.777	17.83	11.67	0.095	3.63	2.10	2.43	0.92	0.236	2.58	5.40	7.98
SAC-SR-10	40.54063	-122.36052	mud	61.33	0.787	17.60	10.78	0.103	3.45	2.17	2.71	0.85	0.215	2.64	9.32	11.96
SAC-RB-12-W	40.18542	-122.23293	mud	64.24	0.948	16.88	8.46	0.273	2.55	2.62	1.62	2.12	0.297	2.28	4.31	6.59
SAC-RB-14	40.17575	-122.22890	mud	63.58	0.848	17.51	9.29	0.206	2.85	2.18	1.83	1.43	0.261	3.12	9.81	12.93
SAC-TEH-17A-W	40.02815	-122.11792	mud	60.76	1.057	17.94	10.14	0.122	3.46	3.06	1.82	1.36	0.275	3.08	5.51	8.59
SAC-TEH-17A	40.02815	-122.11792	mud	62.18	0.897	18.14	8.98	0.134	3.17	2.92	1.92	1.39	0.261	2.86	9.30	12.16
SAC-TEH-17B	40.02815	-122.11792	mud	63.97	0.918	17.09	8.42	0.099	3.04	2.97	1.96	1.29	0.244	2.28	9.39	11.67
SAC-TEH-18	40.02815	-122.11792	mud	62.92	0.985	17.11	8.64	0.154	3.35	3.32	1.99	1.28	0.250	2.48	8.20	10.68
BC-NF-19-W	40.44762	-121.86768	mud	58.24	1.301	21.37	9.22	0.125	2.84	3.82	1.89	0.94	0.259	2.61	6.39	9.00
BC-NF-20A	40.44762	-121.86768	mud	58.24	1.320	21.21	9.43	0.210	2.77	3.86	1.77	0.91	0.283	3.28	18.55	21.83
SJ-CL-01	37.43022	-120.01417	mud	63.48	0.925	18.16	7.81	0.167	2.87	2.22	1.76	2.39	0.220	3.14	7.13	10.27
SJ-HF-02-W	37.34953	-120.97513	mud	63.52	0.971	17.44	8.15	0.151	2.66	2.30	2.37	2.17	0.263	2.60	4.00	6.60
MR-RR-02-W	37.35072	-120.96248	mud	67.61	0.793	15.77	7.63	0.179	2.46	2.21	1.88	1.19	0.279	3.19	4.30	7.49
F8-90-NC-7G9	37.41133	-123.07900	mud	58.79	0.839	15.36	6.70	0.056	3.89	2.21	9.14	2.68	0.341	14.52	n/a	
F2-89-NC-G6869®	37.67802	-122.66647	mud	47.20	0.835	11.90	5.70	0.053	4.76	2.66	24.26	2.23	0.398	30.77	n/a	
SAC-CW-48	40.37707	-122.28392	mud	63.13	0.931	18.38	8.54	0.072	3.29	1.72	1.80	1.80	0.348	8.93	n/a	
SAC-KL-30	38.85310	-121.72572	mud	62.58	0.910	18.35	8.21	0.209	3.65	2.00	1.99	1.75	0.351	8.13	n/a	
FR-VA-28	38.78788	-121.62267	mud	62.45	1.055	18.95	8.96	0.132	3.02	2.60	1.23	1.33	0.269	8.11	n/a	
BCC-22	39.74865	-121.80120	mud	61.86	0.993	18.76	8.63	0.175	2.94	3.86	1.50	0.78	0.499	11.23	n/a	
SAC-FT-29	38.67215	-121.62395	mud	62.62	0.995	18.41	8.40	0.242	3.57	2.30	1.64	1.55	0.262	9.66	n/a	
SJ-MD-35	37.78818	-121.30762	mud	57.88	1.131	18.66	11.61	0.394	3.13	2.99	1.55	2.04	0.605	12.40	n/a	
SJ-FR-45	36.99223	-119.71417	mud	64.70	0.908	17.90	7.85	0.134	2.28	1.85	1.48	2.47	0.414	10.81	n/a	
KR-SGR-46	36.69947	-119.51080	mud	63.46	0.834	15.99	7.94	0.338	3.38	3.74	2.03	1.70	0.598	9.69	n/a	
AR-DP-31	38.60163	-121.50380	mud	67.64	0.941	16.28	7.19	0.187	2.42	2.26	1.16	1.67	0.253	7.30	n/a	
SAC-BTC-24	39.46443	-121.99312	mud	62.88	0.946	18.03	8.44	0.168	3.38	2.27	2.06	1.55	0.269	9.50	n/a	
MKR-LL-32	38.15005	-121.29613	mud	60.54	1.063	19.51	8.12	0.183	2.35	3.21	2.32	2.33	0.372	7.55	n/a	
TR-SRB-38	37.60282	-121.13097	mud	61.19	0.864	16.99	11.48	0.213	2.59	2.44	1.62	1.80	0.809	9.84	n/a	
SR-CSP-36	37.69413	-121.18100	mud	59.33	1.245	18.46	10.29	0.180	2.83	3.14	2.04	1.92	0.560	9.49	n/a	
SJ-MD-35S	37.78818	-121.30762	sand	71.71	0.562	13.99	3.21	0.072	1.45	3.67	3.01	2.24	0.088	1.38	n/a	
MKR-LL-32S	38.15005	-121.29613	sand	72.98	0.484	13.45	3.28	0.066	1.15	3.45	2.82	2.23	0.080	1.29	n/a	
KR-SGR-46S	36.69947	-119.51080	sand	69.54	1.348	12.19	5.88	0.154	2.18	4.40	2.53	1.68	0.094	0.71	n/a	
SAC-BTC-24S	39.46443	-121.99312	sand	71.78	0.571	13.51	4.60	0.074	2.86	2.62	2.55	1.34	0.097	3.77	n/a	
AR-DP-31S	38.60163	-121.50380	sand	81.93	0.600	7.93	3.91	0.066	1.42	1.90	0.89	1.28	0.063	2.18	n/a	
TR-SRB-38S	37.60282	-121.13097	sand	73.22	0.504	12.79	3.73	0.077	1.67	3.39	2.36	2.17	0.082	1.89	n/a	
SR-CSP-36S	37.69413	-121.18100	sand	65.77	0.925	16.02	5.31	0.102	2.37	4.27	3.01	2.06	0.159	3.22	n/a	

TABLE A7_2

Central valley trace element results (ppm)

XRF Sample ID	Ni	Cr	Sc	V	Ba	Rb	Sr	Zr	Y	Nb	Ga	Cu	Zn	Pb	La	Ce	Th	Nd	U	Cs	As >/=
ML-1A	149	196	24	119	91	12	61	36	15	2.1	9	41	55	123	6	10	1	6	0	0	5
ML-1B	105	148	21	109	110	14	63	45	14	2.6	10	43	59	96	5	10	1	6	0	1	0
GL-3	1272	1291	12	67	155	25	80	61	14	3.2	7	28	84	64	10	13	2	8	2	1	1
GL-4-W	1958	2026	15	83	106	18	69	72	17	3.0	9	22	82	35	4	14	3	9	1	2	0
EC-5	1161	2413	16	94	204	16	227	87	9	2.7	12	32	92	49	8	16	2	7	2	2	4
EC-6	2164	1747	15	91	205	18	203	75	8	3.1	10	37	87	28	7	19	3	10	2	2	15
SAC-SC-8	1002	769	24	182	319	22	75	60	16	3.4	13	82	145	19	6	19	2	9	1	4	20
SAC-SC-8-W	988	878	26	197	323	23	87	69	18	5.7	12	84	149	22	10	18	4	4	1		
SAC-SR-9-W	86	156	27	216	543	29	123	127	31	3.6	19	326	710	55	10	21	4	14	1	9	83
SAC-SR-10	74	166	25	197	600	25	123	129	29	4.1	17	262	720	73	11	21	2	14	2	2	52
SAC-RB-12-W	63	121	21	177	999	96	207	547	30	14.0	19	62	132	24	38	68	17	29	15	3	12
SAC-RB-14	106	185	24	185	563	52	165	180	29	8.1	19	109	290	20	22	42	5	20	1		
SAC-TEH-17A-W	93	316	25	225	801	48	227	354	28	9.0	20	76	174	19	23	40	7	22	2	11	61
SAC-TEH-17A	87	174	22	192	861	45	227	152	24	6.9	17	70	166	16	19	36	5	19	3	14	53
SAC-TEH-17B	73	229	21	174	587	41	223	217	23	6.5	15	71	161	34	15	37	5	19	1	18	23
SAC-TEH-18	84	301	24	199	561	40	235	297	24	6.8	17	72	170	36	20	32	5	17	2	12	28
BC-NF-19-W	87	194	26	209	459	34	271	277	26	8.4	20	65	105	14	18	40	7	22	3	5	8
BC-NF-20A	79	171	24	195	395	30	238	228	25	6.8	17	59	100	10	16	31	4	18	4	1	0
SJ-CL-01	73	125	18	150	887	107	206	287	28	13.4	20	51	124	19	39	72	16	30	10	4	6
SJ-HF-02-W	61	120	21	170	952	96	195	387	28	13.6	19	57	126	19	38	70	18	32	15	3	14
MR-RR-02-W	96	228	21	169	533	41	163	196	27	6.8	16	92	271	15	18	38	5	21	2	2	18
F8-90-NC-7G9	84	236	16	124	419	78	171	398	19	9.6	15	39	121	9	27	44	7	19	5		
2-89-NC-G6869	52	290	13	104	245	41	167	306	14	7.0	9	13	51	4	15	35	2	14	3		
SAC-CW-48	146	244	24	178	663	59	158	170	25	8.4	18	64	121	19	22	46	6	22	3		
SAC-KL-30	128	181	25	183	656	68	147	131	24	6.4	18	88	227	16	17	38	6	21	1		
FR-VA-28	135	237	27	199	643	49	153	168	29	9.0	20	99	131	42	25	58	8	28	2		
BCC-22	95	201	26	213	381	29	224	121	22	5.1	17	62	103	20	13	31	4	18	2		
SAC-FT-29	134	212	23	183	604	60	152	146	25	7.6	18	83	166	19	19	42	6	20	3		
SJ-MD-35	93	169	20	166	901	93	249	851	30	14.5	19	55	139	39	45	92	21	38	10		
SJ-FR-45	37	80	13	129	692	109	169	244	26	13.1	20	40	135	83	43	81	17	33	12		
KR-SGR-46	111	166	15	123	669	68	201	208	27	11.7	16	44	122	35	35	71	16	30	20		
AR-DP-31	104	189	19	175	748	62	196	220	29	10.7	18	58	103	24	35	76	10	32	4		
SAC-BTC-24	117	203	24	200	806	52	179	150	27	7.6	18	109	217	22	18	44	6	24	3		
MKR-LL-32	46	84	17	158	926	97	318	335	26	13.7	21	65	184	41	43	81	17	34	4		
TR-SRB-38	81	115	18	202	1476	78	274	151	27	10.6	17	52	133	44	38	79	12	33	22		
SR-CSP-36	87	159	20	187	847	81	319	343	29	12.6	19	63	130	28	42	78	13	37	11		
SJ-MD-35S	23	86	11	73	711	66	385	239	17	9.0	15	8	45	15	15	41	9	21	3		
MKR-LL-32S	13	39	9	75	783	55	382	213	16	10.2	14	13	59	17	23	45	9	21	2		
KR-SGR-46S	27	286	18	125	498	44	256	306	31	18.1	12	7	61	11	42	79	21	34	6		
SAC-BTC-24S	79	203	14	119	503	38	229	88	15	5.1	12	43	126	9	13	24	3	13	1		
AR-DP-31S	40	288	9	104	473	37	167	300	11	6.1	9	19	49	9	12	23	4	11	2		
TR-SRB-38S	30	130	11	86	731	63	336	136	15	7.1	13	12	52	13	20	39	8	19	4		
SR-CSP-36S	41	125	13	116	733	72	482	214	18	11.0	17	21	82	15	22	48	10	23	3		

TABLE A7_3

Central valley rare-earth element trace element results (ppm) by ICPMS

Sample ID	La	Ce	Pr	Nd	Sm	Eu	Gd	Tb	Dy	Ho	Er	Tm	Yb	Lu
ML-1A	4.99	9.82	1.46	6.45	1.66	0.52	2.04	0.35	2.24	0.48	1.38	0.20	1.24	0.20
ML-1B	5.71	10.89	1.62	7.12	1.81	0.56	2.11	0.35	2.24	0.48	1.34	0.20	1.26	0.20
GL-3	6.66	11.87	1.69	7.06	1.70	0.47	1.87	0.32	2.08	0.46	1.31	0.19	1.27	0.22
GL-4-W	6.83	11.13	1.80	7.63	1.89	0.57	2.22	0.38	2.49	0.54	1.54	0.23	1.49	0.24
EC-5	8.19	17.59	2.18	8.90	1.88	0.58	1.78	0.28	1.67	0.34	0.92	0.14	0.89	0.14
EC-6	8.41	18.22	2.18	9.01	1.98	0.58	1.72	0.27	1.63	0.33	0.89	0.13	0.85	0.14
SAC-SC-8	7.22	16.33	1.97	8.32	2.15	0.62	2.38	0.43	2.73	0.58	1.60	0.25	1.55	0.25
SAC-SC-8-W	7.94	17.71	2.14	9.02	2.32	0.68	2.53	0.45	2.90	0.62	1.72	0.25	1.64	0.27
SAC-SR-9-W	9.59	21.00	3.02	13.67	3.94	1.08	4.54	0.82	5.31	1.14	3.22	0.48	3.13	0.51
SAC-SR-10	8.97	20.16	2.89	12.95	3.74	1.04	4.36	0.78	5.03	1.11	3.07	0.45	2.97	0.50
SAC-RB-12-W	35.80	69.28	8.03	29.91	6.15	1.39	5.34	0.86	5.20	1.07	2.94	0.45	3.02	0.51
SAC-RB-14	18.10	44.72	4.74	19.62	4.79	1.23	4.51	0.74	4.57	0.94	2.56	0.38	2.46	0.41
SAC-TEH-17A-W	19.68	41.65	5.19	20.98	4.74	1.26	4.52	0.76	4.68	0.98	2.68	0.41	2.65	0.45
SAC-TEH-17A	17.22	37.23	4.56	18.50	4.21	1.15	4.11	0.69	4.13	0.87	2.38	0.35	2.29	0.35
SAC-TEH-17B	16.31	33.42	4.34	17.59	4.02	1.11	3.89	0.65	3.93	0.83	2.27	0.34	2.20	0.35
SAC-TEH-18	16.92	36.11	4.48	18.26	4.21	1.14	3.99	0.67	4.10	0.87	2.39	0.36	2.35	0.39
BC-NF-19-W	17.88	37.06	4.66	19.15	4.40	1.23	4.34	0.73	4.56	0.97	2.69	0.41	2.67	0.45
BC-NF-20A	15.15	33.09	4.03	16.51	3.87	1.08	3.82	0.64	4.06	0.87	2.37	0.36	2.42	0.39
SJ-CL-01	37.91	72.19	8.31	30.76	6.05	1.35	5.32	0.86	4.99	1.03	2.78	0.41	2.67	0.43
SJ-HF-02-W	37.17	71.65	8.32	30.61	6.20	1.40	5.36	0.85	5.23	1.06	2.89	0.44	2.90	0.49
MR-RR-02-W	16.43	34.06	4.40	18.24	4.48	1.20	4.54	0.75	4.62	0.98	2.72	0.40	2.60	0.41
F8-90-NC-7G9	23.97	47.37	5.79	21.55	4.41	0.98	3.87	0.61	3.86	0.80	2.24	0.34	2.32	0.38
2-89-NC-G6869	15.90	33.13	3.97	15.49	3.39	0.78	2.88	0.46	2.79	0.57	1.61	0.25	1.72	0.28
SAC-CW-48	21.50	44.54	5.44	21.82	4.93	1.31	4.64	0.75	4.68	0.95	2.61	0.38	2.45	0.40
SAC-KL-30	17.66	37.04	4.63	18.68	4.41	1.21	4.40	0.72	4.64	0.94	2.61	0.39	2.50	0.42
FR-VA-28	25.90	54.88	6.47	26.42	5.85	1.58	5.54	0.89	5.55	1.13	3.08	0.45	2.83	0.45
BCC-22	14.80	31.32	4.07	16.88	4.04	1.26	4.09	0.67	4.27	0.88	2.38	0.36	2.26	0.37
SAC-FT-29	20.72	43.21	5.31	21.58	4.87	1.37	4.74	0.77	4.82	0.97	2.71	0.40	2.53	0.40
SJ-MD-35	48.37	97.27	10.85	40.39	8.05	1.71	6.73	1.05	6.24	1.27	3.53	0.54	3.65	0.62
SJ-FR-45	41.75	76.94	9.26	34.15	6.82	1.12	5.73	0.86	5.15	1.02	2.78	0.41	2.68	0.42
KR-SGR-46	36.40	70.38	8.07	30.09	5.93	1.31	5.39	0.85	5.10	1.04	2.88	0.42	2.70	0.44
AR-DP-31	34.23	72.65	8.42	32.29	6.76	1.64	5.89	0.91	5.39	1.10	2.96	0.43	2.72	0.42
SAC-BTC-24	19.21	40.02	5.18	21.28	5.17	1.40	5.04	0.83	5.08	1.08	2.90	0.42	2.70	0.42
MKR-LL-32	40.59	80.34	9.20	34.55	6.91	1.61	5.75	0.87	5.18	1.03	2.73	0.42	2.67	0.42
TR-SRB-38	37.33	76.52	8.58	32.47	6.55	1.53	5.84	0.88	5.34	1.06	2.87	0.42	2.63	0.41
SR-CSP-36	40.63	77.64	9.73	37.71	7.69	1.88	6.48	0.96	5.67	1.15	3.01	0.45	2.84	0.45
SJ-MD-35S	20.41	41.35	5.15	19.77	4.25	1.03	3.49	0.55	3.16	0.64	1.78	0.27	1.73	0.27
MKR-LL-32S	21.22	43.74	5.49	20.83	4.39	1.03	3.54	0.54	3.21	0.62	1.69	0.26	1.64	0.25
KR-SGR-46S	39.52	80.53	9.86	37.03	7.79	1.40	6.51	1.04	6.13	1.21	3.31	0.49	3.13	0.47
SAC-BTC-24S	11.04	21.25	2.84	11.33	2.67	0.79	2.56	0.43	2.75	0.56	1.51	0.23	1.51	0.25
AR-DP-31S	13.75	26.87	3.39	12.97	2.75	0.66	2.37	0.36	2.19	0.45	1.24	0.18	1.26	0.20
TR-SRB-38S	19.29	38.60	4.71	17.71	3.65	0.91	3.17	0.51	2.94	0.58	1.59	0.23	1.49	0.22
SR-CSP-36S	25.09	48.04	6.14	23.63	4.73	1.29	3.94	0.60	3.45	0.67	1.74	0.26	1.65	0.27

TABLE A7_4

Locations and Zr concentations for samples in San Francisco Bay region

Field No.	Sample Description	Latitude	Longitude	Zr (PPM)
SS-01	Suisun Bay	38.0694439	-122.07081	161
SS-03	Suisun Bay	38.1229127	-122.00881	140
SS-04	Suisun Bay	38.1214949	-122.04879	122
SS-07	Suisun Bay	38.1266262	-122.02718	162
SS-08	Suisun Bay	38.1228319	-122.00884	251
RMP-43(SU-43)	Suisun Bay	38.0994483	-122.04658	146
RMP-51(SU-48)	Suisun Bay	38.1044167	-122.01752	140
RMP-42(SU-55)	Suisun Bay	38.08827	-122.06836	656
SS-09	Grizzly Bay	38.0631717	-121.95599	596
SS-10	Grizzly Bay	38.0686676	-121.9417	297
SS-12	Grizzly Bay	38.0717285	-121.93335	131
SS-13	Confluence	38.0429619	-121.88112	328
SS-14	Confluence	38.0631098	-121.95613	983
RMP-45(BG-30)	Confluence	38.0228217	-121.80837	190
SP-01	San Pablo Bay	38.0107052	-122.46552	153
SP-02	San Pablo Bay	38.0034436	-122.42778	189
SP-03	San Pablo Bay	38.0418315	-122.46867	146
SP-04	San Pablo Bay	38.0292778	-122.39784	137
SP-05	San Pablo Bay	38.0622673	-122.46358	127
SP-06	San Pablo Bay	38.0834334	-122.4451	146
SP-07	San Pablo Bay	38.0912784	-122.42346	142
SP-08	San Pablo Bay	38.1000385	-122.39007	131
SP-09	San Pablo Bay	38.1037058	-122.36555	130
SP-10	San Pablo Bay	38.0917796	-122.33256	122
SP-11	San Pablo Bay	38.0554726	-122.34303	238
SP-12	San Pablo Bay	38.0750564	-122.30591	134
SP-13	San Pablo Bay	37.9709198	-122.42479	224
SP-14	San Pablo Bay	37.9828936	-122.41481	176
SP-15	San Pablo Bay	37.9865611	-122.40389	179
SP-16	San Pablo Bay	37.9954883	-122.38379	151
SP-17	San Pablo Bay	38.0099063	-122.38504	139
SP-18	San Pablo Bay	38.0142947	-122.35298	129
SP-19	San Pablo Bay	38.0217494	-122.30769	130
SP-20	San Pablo Bay	38.0340086	-122.31689	188
BR-03	Ebb delta (BAR)	37.7515939	-122.62804	3960
BR-05	Ebb delta (BAR)	37.8855012	-122.66374	4280
BR-06	Ebb delta (BAR)	37.8756759	-122.64794	639
BR-07	Ebb delta (BAR)	37.8560764	-122.64926	1290
BR-08	Ebb delta (BAR)	37.8331953	-122.66902	845
BR-09	Ebb delta (BAR)	37.7958027	-122.67988	934
BR-10	Ebb delta (BAR)	37.7769654	-122.68	1350
BR-11	Ebb delta (BAR)	37.7448163	-122.67057	1680
BR-12	Ebb delta (BAR)	37.7185123	-122.65371	745
BR-13	Ebb delta (BAR)	37.6952611	-122.62526	1110
BR-14	Ebb delta (BAR)	37.6807381	-122.59191	844
BR-15	Ebb delta (BAR)	37.6696959	-122.56154	2320
BR-16	Ebb delta (BAR)	37.6661565	-122.53406	2490
BR-17	Ebb delta (BAR)	37.6462116	-122.52993	978
BR-18	Ebb delta (BAR)	37.6271323	-122.53043	2740

APPENDIX 8

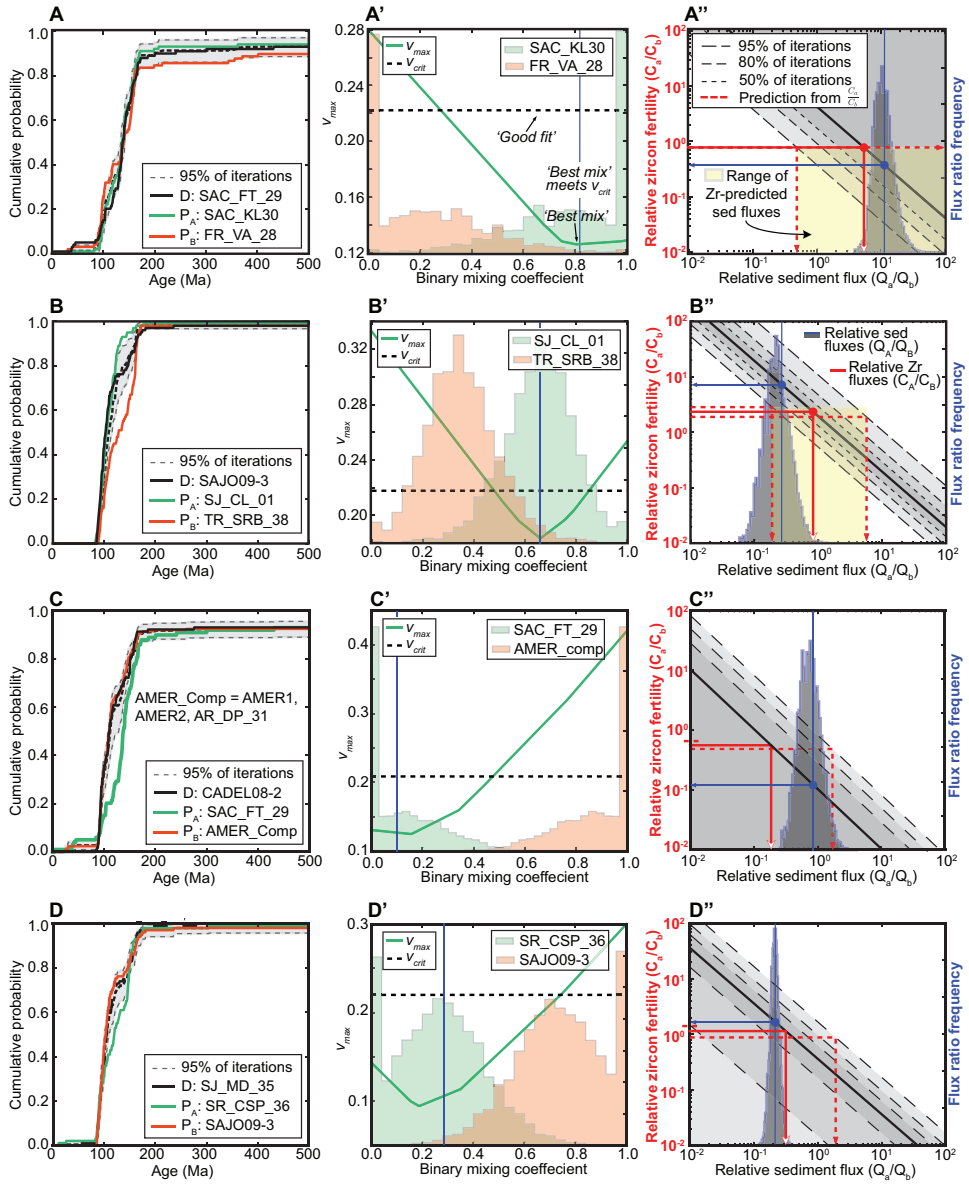

Fig. A8. Results of sediment mixture modeling for all seven trunk-tributary sets. Plots A–D represent the set of mixtures that produce "acceptable" best fits, V_{max} exceeds V_{crit}. Plots E–G represent those that do not produce "acceptable" best fits, V_{max} does not meet V_{crit}. See manuscript figure for legend and more details.

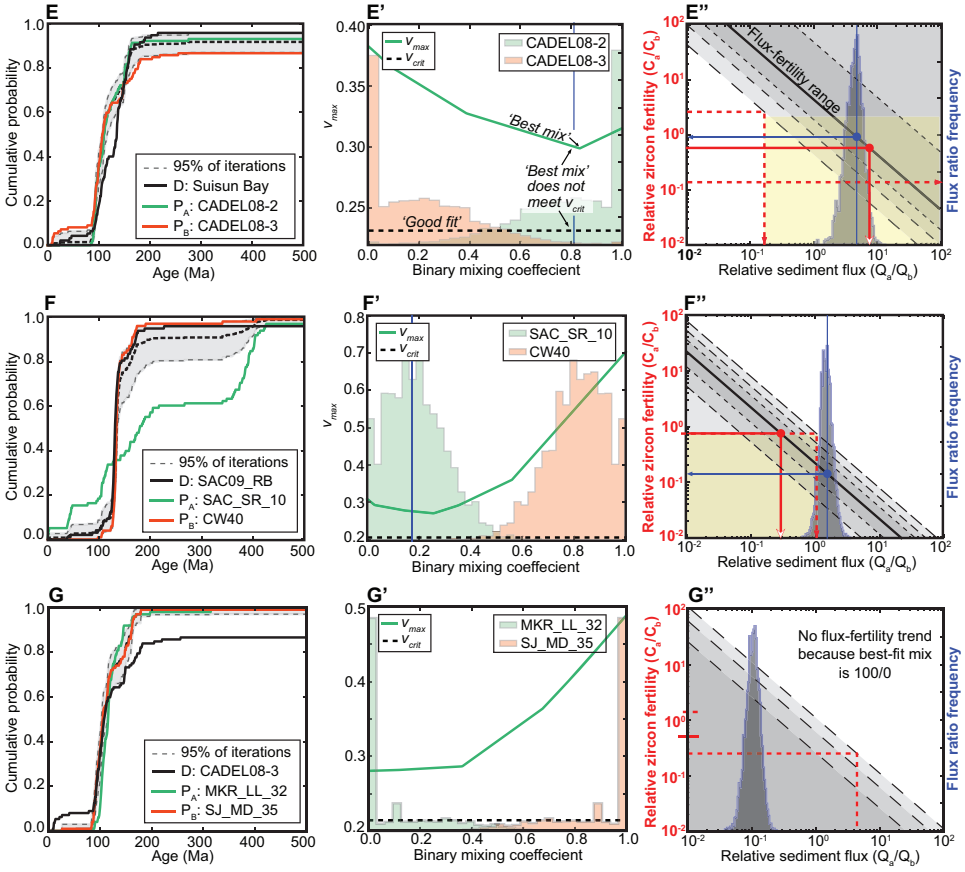
E
Cumulative probability
Age (Ma)
95% of iterations
D: Suisun Bay
P_A: CADEL08-2
P_B: CADEL08-3
E'
V_max
V_crit
CADEL08-2
CADEL08-3
'Best mix'
'Best mix' does not meet V_crit
'Good fit'
Binary mixing coeffecient
E''
Flux-fertility range
Relative zircon fertility (C_a/C_b)
Flux ratio frequency
Relative sediment flux (Q_a/Q_b)
F
95% of iterations
D: SAC09_RB
P_A: SAC_SR_10
P_B: CW40
F'
SAC_SR_10
CW40
F''
G
95% of iterations
D: CADEL08-3
P_A: MKR_LL_32
P_B: SJ_MD_35
G'
MKR_LL_32
SJ_MD_35
G''
No flux-fertility trend because best-fit mix is 100/0

REFERENCES CITED

Ague, J. J., and Brimhall, G. H., 1988, Regional variations in bulk chemistry, mineralogy, and the compositions of mafic and accessory minerals in the batholiths of California: GSA Bulletin, v. 100, n. 6, p. 891–911, https://doi.org/10.1130/0016-7606(1988)100<0891:RVIBCM>2.3.CO;2

Alizai, A., Carter, A., Clift, P. D., VanLaningham, S., Williams, J. C., and Kumar, R., 2011, Sediment provenance, reworking and transport processes in the Indus River by U-Pb dating of detrital zircon grains: Global and Planetary Change, v. 76, n. 1–2, p. 33–55. https://doi.org/10.1016/j.gloplacha.2010.11.008

Alpers, C. N., Hunerlach, M. P., May, J. T., and Hothem, R. L., 2005, Mercury contamination from historical gold mining in California: U.S. Geological Survey Fact Sheet 2005–3014, 6 p. Also available at http://pubs.water.usgs.gov/fs2005-3014.

Amidon, W. H., Burbank, D. W., and Gehrels, G. E., 2005a, U-Pb zircon ages as a sediment mixing tracer in the Nepal Himalaya: Earth and Planetary Science Letters, v. 235, n. 1–2, p. 244–260, https://doi.org/10.1016/j.epsl.2005.03.019

——— 2005b, Construction of detrital mineral populations: Insights from mixing of U–Pb zircon ages in Himalayan rivers: Basin Research, v. 17, n. 4, p. 463–485, https://doi.org/10.1111/j.1365-2117.2005.00279.x

Andersen, T., Kristoffersen, M., and Elburg, M. A., 2016, How far can we trust provenance and crustal evolution information from detrital zircons? A South African case study: Gondwana Research, v. 34, p. 129–148, https://doi.org/10.1016/j.gr.2016.03.003

Atwater, T. M., 1989, Plate tectonic history of the northeast Pacific and western North America, *in* Winterer, E. L., Hussong, D. M., and Decker, R. W., editors, The eastern Pacific Ocean and Hawaii: Boulder, Colorado, Geological Society of America, Geology of North America, v. N, p. 21–72, https://doi.org/10.1130/DNAG-GNA-N.21

Barnard, P. L., Foxgrover, A. C., Elias, E. P., Erikson, L. H., Hein, J. R., McGann, M., Mizell, K., Rosenbauer, R. J., Swarzenski, P. W., Takesue, R. K., Wong, F. L., and Woodrow, D. L., 2013, Integration of bed characteristics, geochemical tracers, current measurements, and numerical modeling for assessing the provenance of beach sand in the San Francisco Bay Coastal System: Marine Geology, v. 336, p. 120–145, https://doi.org/10.1016/j.margeo.2012.11.008

Barth, A. P., Walker, J. D., Wooden, J. L., Riggs, N. R., and Schweickert, R. A., 2011, Birth of the Sierra Nevada magmatic arc: Early Mesozoic plutonism and volcanism in the east-central Sierra Nevada of California: Geosphere, v. 7, n. 4, p. 877–897, https://doi.org/10.1130/GES00661.1

Barth, A. P., Wooden, J. L., Jacobson, C. E., and Economos, R. C., 2013, Detrital zircon as a proxy for tracking the magmatic arc system: The California arc example: Geology, v. 41, n. 2, p. 223–226, https://doi.org/10.1130/G33619.1

Barton, M. D., Girardi, J. D., Kreiner, D. C., Seedorff, E., Zurcher, L., Dilles, J. H., Haxel, G. B., and Johnson, D. A., 2011, Jurassic igneous-related metallogeny of southwestern North America, *in* Steinger, R. L., and Pennell, B., editors, Great Basin Evolution and Metallogeny: Reno, Nevada, Geological Society of Nevada, p. 373–396.

Basu, A., Bickford, M. E., and Deasy, R., 2016, Inferring tectonic provenance of siliciclastic rocks from their chemical compositions: A dissent: Sedimentary Geology, v. 336, p. 26–35, https://doi.org/10.1016/j.sedgeo.2015.11.013

Bateman, P. C., 1992, Plutonism in the central part of the Sierra Nevada batholith, California: U.S. Geologic Survey Professional Paper 1483, 186 p., https://doi.org/10.3133/pp1483

Bea, F., Montero, P., and Ortega, M., 2006, A LA–ICP–MS evaluation of Zr reservoirs in common crustal rocks: Implications for Zr and Hf geochemistry, and zircon-forming processes: Canadian Mineralogist, v. 44, n. 3, p. 693–714, https://doi.org/10.2113/gscanmin.44.3.693

Beinlich, A., Austrheim, H., Mavromatis, V., Grguric, B., Putnis, C. V., and Putnis, A., 2018, Peridotite weathering is the missing ingredient of Earth's continental crust composition: Nature Communications, v. 9, article number 634, https://doi.org/10.1038/s41467-018-03039-9

Bernet, M., and Garver, J. I., 2005, Fission-track analysis of detrital zircon: Reviews in Mineralogy and Geochemistry, v. 58, n. 1, p. 205–237, https://doi.org/10.2138/rmg.2005.58.8

Bernet, M., Brandon, M. T., Garver, J. I., and Molitor, B., 2004, Downstream changes of Alpine zircon fission-track ages in the Rhône and Rhine Rivers: Journal of Sedimentary Research, v. 74, n. 1, p. 82–94, https://doi.org/10.1306/041003740082

Bhatia, M. R., 1983, Plate tectonics and geochemical composition of sandstones: The Journal of Geology, v. 91, n. 6, p. 611–627, https://doi.org/10.1086/628815

Bhatia, M. R., and Crook, K. A. W., 1986, Trace element characteristics of graywackes and tectonic setting discrimination of sedimentary basins: Contributions to Mineralogy and Petrology, v. 92, n. 2, p. 181–193, https://doi.org/10.1007/BF00375292

Brice, J., 1977, Lateral migration of the middle Sacramento River, California: U.S. Geological Survey Water-Resources Investigations Report 77–43, 51 p.

Bullen, T. D., and Clynne, M. A., 1990, Trace element and isotopic constraints on magmatic evolution at Lassen volcanic center: Journal of Geophysical Research- Solid Earth, v. 95, n. B12, p. 19671–19691, https://doi.org/10.1029/JB095iB12p19671

Carrapa, B., Faiz bin Hassim, M., Kapp, P. A., DeCelles, P. G., and Gehrels, G., 2017, Tectonic and erosional history of southern Tibet recorded by detrital chronological signatures along the Yarlung River drainage: GSA Bulletin, v. 129, n. 5–6, p. 570–581, https://doi.org/10.1130/B31587.1

Cassel, E. J., Grove, M., and Graham, S. A., 2012, Eocene drainage evolution and erosion of the Sierra Nevada batholith across northern California and Nevada: American Journal of Science, v. 312, n. 2, p. 117–144, https://doi.org/10.2475/02.2012.03

Cawood, P. A., Nemchin, A. A., Freeman, M., and Sircombe, K., 2003, Linking source and sedimentary basin: Detrital zircon record of sediment flux along a modern river system and implications for provenance studies: Earth and Planetary Science Letters, v. 210, n. 1–2, p. 259–268, https://doi.org/10.1016/S0012-821X(03)00122-5

Cecil, M. R., Ducea, M. N., Reiners, P., Gehrels, G., Mulch, A., Allen, C., and Campbell, I., 2010, Provenance of Eocene river sediments from the central northern Sierra Nevada and implications for paleotopography: Tectonics, v. 29, n. 6, TC6010, 13 p., https://doi.org/10.1029/2010TC002717

Chapman, A. D., Saleeby, J. B., Wood, D. J., Piasecki, A., Kidder, S., Ducea, M. N., and Farley, K. A., 2012, Late Cretaceous gravitational collapse of the southern Sierra Nevada batholith, California: Geosphere, v. 8, n. 2, p. 314–341, https://doi.org/10.1130/GES00740.1

Chaudhry, M. H., 2008, Open-Channel Flow: New York, New York, Springer, p. 528, https://doi.org/10.1007/978-0-387-68648-6

Chen, J. H., and Moore, J. G., 1982, Uranium-lead isotopic ages from the Sierra Nevada Batholith, California: Journal of Geophysical Research-Solid Earth, v. 87, n. B6, p. 4761–4784, https://doi.org/10.1029/JB087iB06p04761

Cina, S. E., Yin, A., Grove, M., Dubey, C. S., Shukla, D. P., Lovera, O. M., Kelty, T. K., Gehrels, G. E., and Foster, D. A., 2009, Gangdese arc detritus within the eastern Himalayan Neogene foreland basin: Implications for the Neogene evolution of the Yalu–Brahmaputra River system: Earth and Planetary Science Letters, v. 285, n. 1–2, p. 150–162, https://doi.org/10.1016/j.epsl.2009.06.005

Clift, P. D., Draut, A. E., Kelemen, P. B., Blusztajn, J., and Greene, A., 2005, Stratigraphic and geochemical evolution of an oceanic arc upper crustal section: The Jurassic Talkeetna Volcanic Formation, south-central Alaska: GSA Bulletin, v. 117, n. 7–8, p. 902–925, https://doi.org/10.1130/B25638.1

Clifton, H. E., and Hunter, R. E., 1987, The Merced Formation and related beds: A mile-thick succession of late Cenozoic coastal and shelf deposits in the sea cliffs of San Francisco, California: Geological Society of America Centennial Field Guide—Cordilleran Section, p. 257–262, https://doi.org/10.1130/0-8137-5401-1.257

Clynne, M. A., 1990, Stratigraphic, lithologic, and major element geochemical constraints on magmatic evolution at Lassen Volcanic Center, California: Journal of Geophysical Research- Solid Earth, v. 95, n. B12, p. 19651–19669, https://doi.org/10.1029/JB095iB12p19651

Clynne, M. A., and Muffler, L. J. P., 2010, Geologic map of Lassen Volcanic National Park and vicinity, California: U.S. Geological Survey Scientific Investigations Map SIM–2899, scale 1: 50,000, https://doi.org/10.3133/sim2899

Coble, M. A., Burgess, S. D., and Klemetti, E. W., 2017, New zircon (U-Th)/He and U/Pb eruption age for the Rockland tephra, western USA: Quaternary Science Reviews, v. 172, p. 109–117, https://doi.org/10.1016/j.quascirev.2017.08.004

Condie, K. C., 1991, Another look at rare earth elements in shales: Geochimica et Cosmochimica Acta, v. 55, n. 9, p. 2527–2531, https://doi.org/10.1016/0016-7037(91)90370-K

Cox, R., Lowe, D. R., and Cullers, R. L., 1995, The influence of sediment recycling and basement composition on evolution of mudrock chemistry in the southwestern United States: Geochimica et Cosmochimica Acta, v. 59, n. 14, p. 2919–2940, https://doi.org/10.1016/0016-7037(95)00185-9

Craddock. W., and Kylander-Clark, A.R.C., 2013, U-Pb ages of detrital zircons from the Tertiary Mississippi River Delta in central Louisiana: Insights into sediment provenance: Geosphere, v. 9, n. 6, p. 1832–1851, https://doi.org/10.1130/GES00917.1

Cullers, R. L., 1994, The chemical signature of source rocks in size fractions of Holocene stream sediment derived from metamorphic rocks in the wet mountains region, Colorado, USA: Chemical Geology, v. 113, n. 3-4, p. 327–343, https://doi.org/10.1016/0009-2541(94)90074-4

Cullers, R. L., Barrett, T., Carlson, R., and Robinson, B., 1987, Rare-earth element and mineralogic changes in Holocene soil and stream sediment: A case study in the Wet Mountains, Colorado, USA: Chemical Geology, v. 63, n. 3–4, p. 275–297, https://doi.org/10.1016/0009-2541(87)90167-7

Davis, G. A., 1969, Tectonic correlations, Klamath Mountains and western Sierra Nevada, California: GSA Bulletin, v. 80, v. 6, p. 1095–1108, https://doi.org/10.1130/0016-7606(1969)80[1095:TCKMAW]2.0.CO;2

Davis, G. A., Ando, C. J., Cashman, P. H., and Goullaud, L., 1980, Geologic cross section of the central Klamath Mountains, California: Summary: GSA Bulletin, v. 91, n. 3, p. 139–142, https://doi.org/10.1130/0016-7606(1980)91<139:GCSOTC>2.0.CO;2

DeCelles, P. G., 1988, Lithologic provenance modeling applied to the Late Cretaceous synorogenic Echo Canyon Conglomerate, Utah: A case of multiple source areas: Geology, v. 16, n. 11, p. 1039–1043, https://doi.org/10.1130/0091-7613(1988)016<1039:LPMATT>2.3.CO;2

DeCelles, P. G., and Graham, S. A., 2015, Cyclical processes in the North American Cordilleran orogenic system: Geology, v. 43, n. 6, p. 499–502, https://doi.org/10.1130/G36482.1

DeGraaff-Surpless, K., Graham, S. A., Wooden, J. L., and McWilliams, M. O., 2002, Detrital zircon provenance analysis of the Great Valley Group, California: Evolution of an arc-forearc system: GSA Bulletin, v. 114, n. 12, p. 1564–1580, https://doi.org/10.1130/0016-7606(2002)114<1564:DZPAOT>2.0.CO;2

DePaolo, D. J., 1981, A neodymium and strontium isotopic study of the Mesozoic calc-alkalic granitic batholiths of the Sierra Nevada and Peninsular Ranges, California: Journal of Geophysical Research-Solid Earth, v. 86, n. B11, p. 10470–10488, https://doi.org/10.1029/JB086iB11p10470

Dhuime, B., Hawkesworth, C. J., Storey, C. D., and Cawood, P. A., 2011, From sediments to their source rocks: Hf and Nd isotopes in recent river sediments: Geology, v. 39, n. 4, 407–410, https://doi.org/10.1130/G31785.1

Dickinson, W. R., 1970, Relations of andesites, granites, and derivative sandstones to arc-trench tectonics: Reviews of Geophysics and Space Physics, v. 8, n. 4, p. 813–860, https://doi.org/10.1029/RG008i004p00813

——— 1970, Interpreting detrital modes of graywacke and arkose: Journal of Sedimentary Research, v. 40, n. 2, p. 695–707, https://doi.org/10.1306/74D72018-2B21-11D7-8648000102C1865D
——— 1971, Plate tectonics in geologic history: Science, v. 174, n. 4005, p. 107–113, https://doi.org/10.1126/science.174.4005.107
——— 2008, Impact of differential zircon fertility of granitoid basement rocks in North America on age populations of detrital zircons and implications for granite petrogenesis: Earth and Planetary Science Letters, v. 275, n. 1–2, p. 80–92, https://doi.org/10.1016/j.epsl.2008.08.003
Dickinson, W. R., and Rich, E. I., 1972, Petrologic intervals and petrofacies in the Great Valley sequence, Sacramento Valley, California: GSA Bulletin, v. 83, n. 10, p. 3007–3024, https://doi.org/10.1130/0016-7606(1972)83[3007:PIAPIT]2.0.CO;2
Dickinson, W. R., Ingersoll, R. V., and Graham, S. A., 1979, Paleogene sediment dispersal and paleotectonics in northern California: GSA Bulletin, Part I, v. 90, n. 10, p. 897–898, https://doi.org/10.1130/0016-7606(1979)90<897:PSDAPI>2.0.CO;2
——— 1979, Paleogene sediment dispersal and paleotectonics in northern California: GSA Bulletin, Part II, v. 90, https://doi.org/10.1130/GSAB-P2-90-1458
Dickinson, W. R., and Hopson, C. A., and Saleeby, J., 1996, Alternate origins of the Coast Range ophiolite (California): Introduction and implications: GSA Today, v. 6, n. 2, p. 1–10.
Dodge, F. C. W., Millard Jr., H. T., and Elsheimer, H. N., 1982, Compositional variations and abundances of selected elements in granitoid rocks and constituent minerals, central Sierra Nevada batholith, California: U.S.G.S. Professional Paper 1248, 24 p., https://doi.org/10.3133/pp1248
Doherty, W., 1989, An internal standardization procedure for the determination of yttrium and the rare earth elements in geological materials by inductively coupled plasma-mass spectrometry: Spectrochimica Acta, Part B, v. 44, n. 3, p. 263–280, https://doi.org/10.1016/0584-8547(89)80031-X
Draut, A. E., and Clift, P. D., 2001, Geochemical evolution of arc magmatism during arc-continent collision, South Mayo, Ireland: Geology, v. 29, n. 6, p. 543–546, https://doi.org/10.1130/0091-7613(2001)029<0543:GEOAMD>2.0.CO;2
Ducea, M., 2001, The California arc: Thick granitic batholiths, eclogitic residues, lithospheric-scale thrusting, and magmatic flare-ups: GSA Today, v. 11, n. 11, p. 4–10, https://doi.org/10.1130/1052-5173(2001)011<0004:TCATGB>2.0.CO;2
Ducea, M. N., and Barton, M. D., 2007, Igniting flare-up events in Cordilleran arcs: Geology, v. 35, n. 11, p. 1047–1050, https://doi.org/10.1130/G23898A.1
Dumitru, T. A., Ernst, W. G., Wright, J. E., Wooden, J. L., Wells, R. E., Farmer, L. P., Kent, A. J. R., and Graham, S. A., 2013, Eocene extension in Idaho generated massive sediment floods into Franciscan trench and into Tyee, Great Valley, and Green River basins: Geology, v. 41, n. 2, p. 187–190, https://doi.org/10.1130/G33746.1
Dumitru, T. A., Ernst, W. G., Hourigan, J. K., and McLaughlin, R. J., 2015, Detrital zircon U–Pb reconnaissance of the Franciscan subduction complex in northwestern California: International Geology Review, v. 57, n. 5–8, p. 767–800, https://doi.org/10.1080/00206814.2015.1008060
Ernst, W. G., 1970, Tectonic contact between the Franciscan mélange and the Great Valley sequence- Crustal expression of a Late Mesozoic Benioff zone: Journal of Geophysical Research, v. 75, n. 5, p. 886–901, https://doi.org/10.1029/JB075i005p00886
Ernst, W. G., Saleeby, J. B., and Snow, C. A., 2007, Guadalupe pluton–Mariposa Formation age relationships in the southern Sierran Foothills: Onset of Mesozoic subduction in northern California?: Journal of Geophysical Research, v. 114, n. B11, https://doi.org/10.1029/2009JB006607
Ernst, W. G., Martens, U., and Valencia, V., 2009, U–Pb ages of detrital zircons in Pacheco Pass metagraywackes: Sierran–Klamath source of mid–Cretaceous and Late Cretaceous Franciscan deposition and underplating: Tectonics, v. 28, n. 6, 20 p., https://doi.org/10.1029/2008TC002352
Fedo, C. M., Nesbitt, H. W., and Young, G. M., 1995, Unraveling the effects of potassium metasomatism in sedimentary rocks and paleosols, with implications for paleoweathering conditions and provenance: Geology, v. 23, n. 10, p. 921–924, https://doi.org/10.1130/0091-7613(1995)023<0921:UTEOPM>2.3.CO;2
Fedo, C. M., Sircombe, K. N., and Rainbird, R. H., 2003, Detrital zircon analysis of the sedimentary record: Reviews in Mineralogy and Geochemistry, v. 53, n. 1, p. 277–303, https://doi.org/10.2113/0530277
Fielding, L., Najman, Y., Millar, I., Butterworth, P., Ando, S., Padoan, M., Barfod, D., and Kneller, B., 2016, A detrital record of the Nile River and its catchment: Journal of the Geological Society, v. 174, n. 2, p. 301–317, https://doi.org/10.1144/jgs2016-075
Fletcher, J. M., Grove, M., Kimbrough, D., Lovera, O., and Gehrels, G. E., 2007, Ridge-trench interactions and the Neogene tectonic evolution of the Magdalena shelf and southern Gulf of California: Insights from detrital zircon U-Pb ages from the Magdalena fan and adjacent areas: GSA Bulletin, v. 119, n. 11–12, p. 1313–1336, https://doi.org/10.1130/B26067.1
Frink, J. W., and Kues, H. A., 1954, Corcoran Clay—A Pleistocene lacustrine deposit in San Joaquin Valley, California: AAPG Bulletin, v. 38, n. 11, p. 2357–2371, https://doi.org/10.1306/5CEAE0A0-16BB-11D7-8645000102C1865D
Gale, A., Dalton, C. A., Langmuir, C. H., Su, Y., and Schilling, J. G., 2013, The mean composition of ocean ridge basalts: Geochemistry, Geophysics, Geosystems, v. 14, n. 3, p. 489–518, https://doi.org/10.1029/2012GC004334
Ganju, N. K., and Schoellhamer, D. H., 2010, Decadal-timescale estuarine geomorphic change under future scenarios of climate and sediment supply: Estuaries and Coasts, v. 33, n. 1, p. 15–29, https://doi.org/10.1007/s12237-009-9244-y
Garver, J. I., and Scott, T. J., 1995, Trace elements in shale as indicators of crustal provenance and terrane accretion in the southern Canadian Cordillera: GSA Bulletin, v. 107, n. 4, p. 440–453, https://doi.org/10.1130/0016-7606(1995)107<0440:TEISAI>2.3.CO;2

Garver, J. I., Royce, P. R., and Smick, T. A., 1996, Chromium and nickel in shale of the Taconic foreland: A case study for the provenance of fine-grained sediments with an ultramafic source: Journal of Sedimentary Research, v. 66, n. 1, p. 100–106, https://doi.org/10.1306/D42682C5-2B26-11D7-8648000102C1865D

Garver, J. I., Brandon, M. T., Roden-Tice, M., and Kamp, P. J., 1999, Exhumation history of orogenic highlands determined by detrital fission-track thermochronology: Geological Society, London, Special Publications, v. 154, n. 1, p. 283–304, https://doi.org/10.1144/GSL.SP.1999.154.01.13

Garzanti, E., and Andò, S., 2007, Heavy mineral concentration in modern sands: Implications for provenance interpretation: Developments in Sedimentology, v. 58, p. 517–545, https://doi.org/10.1016/S0070-4571(07)58020-9

Garzanti, E., Andò, S., and Vezzoli, G., 2009, Grain-size dependence of sediment composition and environmental bias in provenance studies: Earth and Planetary Science Letters, v. 277, n. 3–4, p. 422–432, https://doi.org/10.1016/j.epsl.2008.11.007

Gehrels, G., and Pecha, M., 2014, Detrital zircon U-Pb geochronology and Hf isotope geochemistry of Paleozoic and Triassic passive margin strata of western North America: Geosphere, v. 10, n. 1, p. 49–65, https://doi.org/10.1130/GES00889.1

Gehrels, G. E., Valencia, V., and Pullen, A., 2006, Detrital zircon geochronology by Laser-Ablation Multicollector ICPMS at the Arizona LaserChron Center, *in* Loszewski, T., and Huff, W., editors, Geochronology: Emerging Opportunities, Paleontology Society Short Course: Paleontology Society Papers, v. 11, 10 p.

Gehrels, G. E., Valencia, V. A., and Ruiz, J., 2008, Enhanced precision, accuracy, efficiency, and spatial resolution of U-Pb ages by laser ablation–multicollector–inductively coupled plasma–mass spectrometry: Geochemistry, Geophysics, Geosystems, v. 9, n. 3, Q03017, https://doi.org/10.1029/2007GC001805

Gilbert, G. K., 1917, Hydraulic-mining debris in the Sierra Nevada: Professional Paper 105, 154 p., https://doi.org/10.3133/pp105

Graham, S. A., Ingersoll, R. V., and Dickinson, W. R., 1976, Common provenance for lithic grains in Carboniferous sandstones from Ouachita Mountains and Black Warrior Basin: Journal of Sedimentary Petrology, v. 46, n. 3, p. 620–632, https://doi.org/10.1306/212F7009-2B24-11D7-8648000102C1865D

Graham, S. A., Tolson, R. B., DeCelles, P. G., Ingersoll, R. V., Bargar, E., Caldwell, M., Cavazza, W., Edwards, D. P., Follo, W. F., Handschy, J. W., Lemke, L., Moxon, I., Rice, R., Smith, G. A., and White, J., 1986, Provenance modelling as a technique for analysing source terrane evolution and controls on foreland sedimentation, *in* Allen, P. A., and Homewood, P., editors, Foreland Basins: International Association of Sedimentologists, Special Publication, v. 8, p. 425–436, https://doi.org/10.1002/9781444303810.ch23

Gruau, G., Lecuyer, C., Bernard-Griffiths, J., and Morin, N., 1991, Origin and petrogenesis of the Trinity ophiolite Complex (California): New constraints from REE and Nd isotope data: Journal of Petrology, v. 2, p. 229–242, https://doi.org/10.1093/petrology/Special_Volume.2.229

Gruau, G., Bernard-Griffiths, J., Lécuyer, C., Henin, O., Macé, J., and Cannat, M., 1995, Extreme Nd isotopic variation in the Trinity ophiolite complex and the role of melt/rock reactions in the oceanic lithosphere: Contributions to Mineralogy and Petrology, v. 121, n. 4, p. 337–350, https://doi.org/10.1007/s004100050100

Guffanti, M., and Weaver, C. S., 1988, Distribution of late Cenozoic volcanic vents in the Cascade Range: Volcanic arc segmentation and regional tectonic considerations: Journal of Geophysical Research: Solid Earth, v. 93, n. B6, p. 6513–6529, https://doi.org/10.1029/JB093iB06p06513

Guffanti, M., Clynne, M. A., Smith, J. G., Muffler, L. J. P., and Bullen, T. D., 1990, Late Cenozoic volcanism, subduction, and extension in the Lassen region of California, southern Cascade Range: Journal of Geophysical Research: Solid Earth, v. 95, B12, p. 19453–19464, https://doi.org/10.1029/JB095iB12p19453

Hall, N. T., ms, 1965, Petrology of the type Merced Group, San Francisco Peninsula, California: Berkeley, California, University of California, Berkeley, M.A. thesis, 127 p.

Hamilton, W., 1969, Mesozoic California and the underflow of Pacific mantle: GSA Bulletin, v. 80, n. 12, p. 2409–2430, https://doi.org/10.1130/0016-7606(1969)80[2409:MCATUO]2.0.CO;2

He, M., Zheng, H., and Clift, P. D., 2013, Zircon U–Pb geochronology and Hf isotope data from the Yangtze River sands: Implications for major magmatic events and crustal evolution in Central China: Chemical Geology, v. 360–361, p. 186–203, https://doi.org/10.1016/j.chemgeo.2013.10.020

Hietpas, J., Samson, S., Moecher, D., and Chakraborty, S., 2011, Enhancing tectonic and provenance information from detrital zircon studies: Assessing terrane-scale sampling and grain-scale characterization: Journal of the Geological Society, v. 168, n. 2, p. 309–318, https://doi.org/10.1144/0016-76492009-163

Hildreth, W., 2007, Quaternary magmatism in the Cascades–Geologic perspectives: U.S. Geological Survey Professional Paper 1744, 125 p., https://doi.org/10.3133/pp1744

Horton, B. K., Constenius, K. N., and DeCelles, P. G., 2004, Tectonic control on coarse-grained foreland-basin sequences: An example from the Cordilleran foreland basin, Utah: Geology, v. 32, n. 7, p. 637–640, https://doi.org/10.1130/G20407.1

Ibañez-Mejia, M., Pullen, A., Pepper, M., Urbani, F., Ghoshal, G., and Ibañez-Mejia, J. C., 2018, Use and abuse of detrital zircon U-Pb geochronology—A case from the Río Orinoco delta, eastern Venezuela: Geology, v. 46, n. 11, p. 1019–1022, https://doi.org/10.1130/G45596.1

Iizuka, T., Campbell, I. H., Allen, C. M., Gill, J. B., Maruyama, S., and Makoka, F., 2013, Evolution of the African continental crust as recorded by U–Pb, Lu–Hf and O isotopes in detrital zircons from modern rivers: Geochimica et Cosmochimica Acta, v. 107, p. 96–120, https://doi.org/10.1016/j.gca.2012.12.028

Ingersoll, R. V., 1978a, Submarine fan facies of the Upper Cretaceous Great Valley Sequence, northern and central California: Sedimentary Geology, v. 21, v. 3, p. 205–230, https://doi.org/10.1016/0037-0738(78)90009-X

——— 1978b, Petrofacies and petrologic evolution of the Late Cretaceous fore-arc basin, northern and central California: The Journal of Geology, v. 86, n. 3, p. 335–352, https://doi.org/10.1086/649695
——— 1979, Evolution of the Late Cretaceous forearc basin, northern and central California: GSA Bulletin, v. 90, Part I, p. 813–826, https://doi.org/10.1130/0016-7606(1979)90<813:EOTLCF>2.0.CO;2
——— 1982, Initiation and evolution of the Great Valley forearc basin of northern and central California, U.S.A., *in* Leggett, J. K., editor, Trench-forearc geology: Sedimentation and tectonics on modern and ancient active plate margins: Geological Society, London, Special Publications, v. 10, p. 459–467, https://doi.org/10.1144/GSL.SP.1982.010.01.31
Ingersoll, R. V., 1983, Petrofacies and provenance of late Mesozoic forearc basin, northern and central California: AAPG, v. 67, n. 7, p. 1125–1142., https://doi.org/10.1306/03B5B713-16D1-11D7-8645000102C1865D
——— 1990, Actualistic sandstone petrofacies: Discriminating modern and ancient source rocks: Geology, v. 18, n. 8, p. 733–736, https://doi.org/10.1130/0091-7613(1990)018<0733:ASPDMA>2.3.CO;2
——— 2012, Composition of modern sand and Cretaceous sandstone derived from the Sierra Nevada, California, USA, with implications for Cenozoic and Mesozoic uplift and dissection: Sedimentary Geology, v. 280, p. 195–207, https://doi.org/10.1016/j.sedgeo.2012.03.022
Ingersoll, R. V., and Eastmond, D. J., 2007, Composition of modern sand from the Sierra Nevada, California, U.S.A.: Implications for actualistic petrofacies of continental margin magmatic arcs: Journal of Sedimentary Research, v. 77, n. 9, p. 784–796, https://doi.org/10.2110/jsr.2007.071
Ingersoll, R. V., Kretchmer, A. G., and Valles, P. K., 1993, The effect of sampling scale on actualistic sandstone petrofacies: Sedimentology, v. 40, n. 5, p. 937–953, https://doi.org/10.1111/j.1365-3091.1993.tb01370.x
Ingram, B. L., and Ingle, J. C., 1998, Strontium isotope ages of the marine Merced Formation, near San Francisco, California: Quaternary Research, v. 50, n. 2, p. 194–199, https://doi.org/10.1006/qres.1998.1990
Irwin, W. P., 1981, Tectonic accretion of the Klamath Mountains, *in* Ernst, W. G., editor, The geotectonic development of California: Englewood Cliffs, New Jersey, Prentice-Hall, p. 29–49.
——— 2003, Correlation of the Klamath Mountains and Sierra Nevada: U.S. Geological Survey Open-File Report 2002-490, https://doi.org/10.3133/ofr02490
Irwin, W. P., and Wooden, J. L., 1999, Plutons and accretionary episodes of the Klamath Mountains, California and Oregon: U.S. Geological Survey Open-File Report 99-374, https://doi.org/10.3133/ofr99374
Jacobson, C. E., Grove, M., Pedrick, J. N., Barth, A. P., Marsaglia, K. M., Gehrels, G. E., and Nourse, J. A., 2011, Late Cretaceous–early Cenozoic tectonic evolution of the southern California margin inferred from provenance of trench and forearc sediments: GSA Bulletin, v. 123, n. 3–4, p. 485–506, https://doi.org/10.1130/B30238.1
Jarvis, K. E., 1988, Inductively coupled plasma mass spectrometry: A new technique for therapid or ultra-trace level determination of the rare-earth elements in geological materials: Chemical Geology, v. 68, n. 1–2, p. 31–39, https://doi.org/10.1016/0009-2541(88)90084-8
Jenner, G. A., Longerich, H. P., Jackson, S. E., and Fryer, B. J., 1990, ICP-MS – A powerful tool for high-precision trace-element analysis in Earth sciences: Evidence from analysis of selected U.S.G.S. reference samples: Chemical Geology, v. 83, n. 1–2, p. 133–148, https://doi.org/10.1016/0009-2541(90)90145-W
Johnson, D. M., Hooper, P. R., and Conrey, R. M., 1999, XRF analysis of rocks and minerals for major and trace elements on a single low dilution Li-tetraborate fused bead: Advances in X-Ray Analysis, v. 41, p. 843–867.
Kamphuis, J. W., 1974, Determination of sand roughness for fixed beds: Journal of Hydraulic Research, v. 12, n. 2, p. 193–203, https://doi.org/10.1080/00221687409499737
Kelley, J. C., and Whetten, J. T., 1969, Quantitative statistical analyses of Columbia River sediment samples: Journal of Sedimentary Petrology, v. 39, n. 3, p. 1167–1173, https://doi.org/10.1306/74D71DBB-2B21-11D7-8648000102C1865D
Kimbrough, D. L., Grove, M., Gehrels, G. E., Dorsey, R. J., Howard, K. A., Lovera, O. M., Aslan, A., House, P. K., and Pearthree, P. A., 2015, Detrital zircon U-Pb provenance of the Colorado River: A 5 my record of incision into cover strata overlying the Colorado Plateau and adjacent regions: Geosphere, v. 11, n. 6, p. 1719–1748, https://doi.org/10.1130/GES00982.1
Kistler R. W., and Peterman, Z. E., 1973, Variations in Sr, Rb, K, Na, and initial $^{87}Sr/^{86}Sr$ in Mesozoic granitic rocks and intruded wall rocks in central California: GSA Bulletin, v. 84, n. 11, p. 3489–3512, https://doi.org/10.1130/0016-7606(1973)84<3489:VISRKN>2.0.CO;2
Kistler, R. W., and Champion, D. E., 2001, Rb-Sr whole-rock and mineral ages, K-Ar, $^{40}Ar/^{39}Ar$, and U-Pb mineral ages, and strontium, lead, neodymium, and oxygen isotopic compositions for granitic rocks from the Salinian Composite Terrane, California: U.S. Geological Survey Open-File Report 2001–453, 83 p., https://doi.org/10.3133/ofr01453
Krone, R. B., 1979, Sedimentation in the San Francisco Bay system, *in* Conomos, T. J., editor, San Francisco Bay: The Urbanized Estuary: American Association for the Advancement of Science, San Francisco, p. 85–96.
Lackey, J. S., Valley, J. W., Chen, J. H., and Stockli, D. F., 2008, Dynamic magma systems, crustal recycling, and alteration in the central Sierra Nevada batholith: The oxygen isotope record: Journal of Petrology, v. 49, n. 7, p. 1397–1426, https://doi.org/10.1093/petrology/egn030
Lawrence, R. L., Cox, R., Mapes, R. W., and Coleman, D. S., 2011, Hydrodynamic fractionation of zircon age populations: GSA Bulletin, v. 123, n. 1–2, p. 295–305, https://doi.org/10.1130/B30151.1
Lawton, T. F., 1986, Compositional trends within a clastic wedge adjacent to a fold-thrust belt: Indianola Group, central Utah, USA.: Foreland Basins, p. 411–423, https://doi.org/10.1002/9781444303810.ch22

Li, Y., Clift, P. D., and O'Sullivan, P., 2018, Millennial and centennial variations in zircon U-Pb ages in the Quaternary Indus submarine canyon: Basin Research, v. 31, n. 1, p. 155–170, https://doi.org/10.1111/bre.12313

Lichte, F. E., Meier, A. L., and Crock, J. G., 1987, Determination of the rare-earth elements in geological materials by inductively coupled plasma mass spectrometry: Analytical Chemistry, v. 59, n. 8, p. 1150–1157, https://doi.org/10.1021/ac00135a018

Lindsley-Griffin, N., 1991, The Trinity complex: A polygenetic ophiolitic assemblage, *in* Cooper, J. D., and Stevens, C. H., editors, Paleozoic paleogeography of the United States II: Los Angeles, Pacific Section, Society of Economic Paleontologists and Mineralogists, Book 67 p. 589–607.

Linn, A. M., DePaolo, D. J., and Ingersoll, R. V., 1992, Nd–Sr isotopic, geochemical, and petrographic stratigraphy and paleotectonic analysis: Mesozoic Great Valley forearc sedimentary rocks of California: GSA Bulletin, v. 104, n. 10, p. 1264–1279, https://doi.org/10.1130/0016-7606(1992)104<1264:NSIGAP>2.3.CO;2

Longerich, H. P., Jenner, G. A., Fryer, B. J., and Jackson, S. E., 1990, Inductively coupled plasma-mass spectrometric analysis of geological samples: A critical evaluation based on case Studies: Chemical Geology, v. 83, n. 1–2, p. 105–118, https://doi.org/10.1016/0009-2541(90)90143-U

Malkowski, M. A., and Hampton, B. A., 2014, Sedimentology, U-Pb detrital geochronology, and Hf isotopic analyses from Mississippian–Permian stratigraphy of the Mystic subterrane, Farewell terrane, Alaska: Lithosphere, v. 6, n. 5, p. 383–398, https://doi.org/10.1130/L365.1

Malusà, M. G., Carter, A., Limoncelli, M., Villa, I. M., and Garzanti, E., 2013, Bias in detrital zircon geochronology and thermochronometry: Chemical Geology, v. 359, p. 90–107, https://doi.org/10.1016/j.chemgeo.2013.09.016

Mapes, R. W., ms, 2009, Past and present provenance of the Amazon River drainage basin: Chapel Hill, North Carolina, University of North Carolina, Ph. D. thesis, 195 p., https://doi.org/10.17615/s09s-f385

Mason, C. C., Fildani, A., Gerber, T., Blum, M. D., Clark, J. D., and Dykstra, M., 2017, Climatic and anthropogenic influences on sediment mixing in the Mississippi source-to-sink system using detrital zircons: Late Pleistocene to recent: Earth and Planetary Science Letters, v. 466, p. 70–79, https://doi.org/10.1016/j.epsl.2017.03.001

Mason, C. C., Romans, B. W., Stockli, D. F., Mapes, R. W., and Fildani, A., 2019, Detrital Zircons reveal sea-level and hydroclimate controls on Amazon river to-fan sediment transfer: Geology, v. 47, n. 6, p. 563–567, https://doi.org/10.1130/G45852.1

McLaughlin, R. J., Kling, S. A., Poore, R. Z., McDougall, K., and Beutner, E. C., 1982, Post–middle Miocene accretion of Franciscan rocks, northwestern California: GSA Bulletin, v. 93, n. 7, 595–605, https://doi.org/10.1130/0016-7606(1982)93<595:PMAOFR>2.0.CO;2

McLaughlin, R. J., Ellen, S. D., Blake Jr, M. C., Jayko, A. S., Irwin, W. P., Aalto, K. R., Carver, G. A., and Clarke Jr., S. H., 2000, Geology of the Cape Mendocino, Eureka, Garberville, and southwestern part of the Hayfork 30× 60 minute quadrangles and adjacent offshore area, northern California: U.S. Geological Survey Miscellaneous Field Studies Map MF-2336, 1(100), 000.

McLaughlin, R. J., Powell, II, C. L., McDougall-Reid, K., and Jachens, R .C., 2007, Cessation of slip on the Pilarcitos fault and initiation of the San Francisco Peninsula segment of the (modern) San Andreas Fault, California: American Geophysical Union, Fall Meeting 2007, abstract #T43A-1089

McLennan, S. M., 1989, Rare earth elements in sedimentary rocks: Influence of provenance and sedimentary processes: Reviews in Mineralogy and Geochemistry, v. 21, p. 169–200, https://doi.org/10.1515/9781501509032-010

McLennan, S. M., and Taylor, S. R., 1991, Sedimentary rocks and crustal evolution: Tectonic setting and secular trends: The Journal of Geology, v. 99, n. 1, p. 1–21, https://doi.org/10.1086/629470

McLennan, S. M., Taylor, S. R., McCulloch, M. T., and Maynard, J. B., 1990, Geochemical and Nd-Sr isotopic composition of deep-sea turbidites: Crustal evolution and plate tectonic associations: Geochimica et Cosmochimica Acta, v. 54, n. 7, p. 2015–2050, https://doi.org/10.1016/0016-7037(90)90269-Q

McLennan, S. M., Hemming, S., McDaniel, D. K., and Hanson, G. N., 1993, Geochemical approaches to sedimentation, provenance, and tectonics: GSA Special Papers, v. 284, p. 21–40, https://doi.org/10.1130/SPE284-p21

Metcalf, R. V., Wallin, E. T., Willse, K. R., and Muller, E. R., 2000, Geology and geochemistry of the Trinity terrane, California: Evidence of middle Paleozoic depleted supra-subduction zone magmatism in a proto-arc setting, *in* Dilek, Y., Moores, E. M., Elthon, D., and Nicolas, A., editors, Ophiolites and Oceanic Crust: New Insights from Field Studies and the Ocean Drilling Program: GSA Special Papers, v. 349, p. 403–418, https://doi.org/10.1130/0-8137-2349-3.403

Moecher, D. P., and Samson, S. D., 2006, Differential zircon fertility of source terranes and natural bias in the detrital zircon record: Implications for sedimentary provenance analysis: Earth and Planetary Science Letters, v. 247, n. 3–4, p. 252–266, https://doi.org/10.1016/j.epsl.2006.04.035

Nesbitt, H. W., and Young, G. M., 1982, Early Proterozoic climates and plate motions inferred from major element chemistry of lutites: Nature, v. 299, n. 5885, p. 715–717, https://doi.org/10.1038/299715a0

——— 1984, Prediction of some weathering trends of plutonic and volcanic rocks based on thermodynamic and kinetic considerations: Geochimica et Cosmochimica Acta, v. 48, n. 7, p. 1523–1534, https://doi.org/10.1016/0016-7037(84)90408-3

——— 1989, Formation and diagenesis of weathering profiles: The Journal of Geology, v. 97, n. 2, p. 129–147, https://doi.org/10.1086/629290

Nittrouer, J. A., and Viparelli, E., 2014, Sand as a stable and sustainable resource for nourishing the Mississippi River delta: Nature Geoscience, v. 7, n. 5, p. 350–354, https://doi.org/10.1038/ngeo2142

Ojakangas, R. W., 1968, Cretaceous sedimentation, Sacramento Valley, California: GSA Bulletin, v. 79, n. 8, p. 973–1008, https://doi.org/10.1130/0016-7606(1968)79[973:CSSVC]2.0.CO;2

Papavassiliou, C. T., and Cosgrove, M. E., 1982, The geochemistry of DSDP sediments from Site 223, Indian Ocean: Chemical Geology, v. 37, n. 3–4, p. 299–315, https://doi.org/10.1016/0009-2541(82)90085-7
Parker, G., 1991, Selective sorting and abrasion of river gravel. II: Applications: Journal of Hydraulic Engineering, v. 117, n. 2, p. 150–171, https://doi.org/10.1061/(ASCE)0733-9429(1991)117:2(150)
Paterson, S. R., and Ducea, M. N., 2015, Arc magmatic tempos: Gathering the evidence: Elements, v. 11, n. 2, p. 91–98, https://doi.org/10.2113/gselements.11.2.91
Porterfield, G., Busch, R. D., and Waananen, A. O., 1978, Sediment transport in the Feather River, Lake Oroville to Yuba City, California: U. S. Geological Survey, Water Resources Investigations Report 78–20, 84 p. https://doi.org/10.3133/wri7820
Potter, P. E., Maynard, J. B., and Depetris, P. J., 2005, Mud and mudstones: Introduction and overview: Heidelberg, Springer-Verlag, 297 p., https://doi.org/10.1007/b138571
Press, W. H., Teukolsky, S. A., Vetterling, W. T., and Flannery, B. P., 2007, Numerical Recipes: The Art of Scientific Computing: New York, Cambridge University Press, 1256 p.
Prohoroff, R., Wakabayashi, J., and Dumitru, T. A., 2012, Sandstone matrix olistostrome deposited on intra-subduction complex serpentinite, Franciscan Complex, western Marin County, California: Tectonophysics, v. 568–569, p. 296–305, https://doi.org/10.1016/j.tecto.2012.05.018
Prokopiev, A. V., Toro, J., Miller, E. L., and Gehrels, G. E., 2008, The paleo–Lena River–200 m.y. of transcontinental zircon transport in Siberia: Geology, v. 36, n. 9, p. 699–702, https://doi.org/10.1130/G24924A.1
Quick, J. E., 1981, Petrology and petrogenesis of the Trinity peridotite, An upper mantle diapir in the eastern Klamath Mountains, northern California: Journal of Geophysical Research-Solid Earth, v. 86, n. B12, p. 11837–11863. https://doi.org/10.1029/JB086iB12p11837
Reiners, P. W., Campbell, I. H., Nicolescu, S., Allen, C. M., Hourigan, J. K., Garver, J. I., Mattinson, J. M., and Cowan, D. S., 2005, (U-Th)/(He-Pb) double dating of detrital zircons: American Journal of Science, v. 305, n. 4, p. 259–311, https://doi.org/10.2475/ajs.305.4.259
Rohling, E. J., Fenton, M., Jorissen, F. J., Bertrand, P., Ganssen, G., and Caulet, J. P., 1998, Magnitudes of sea-level lowstands of the past 500,000 year: Nature, v. 394, p. 162–165, https://doi.org/10.1038/28134
Rosenbauer, R. J., Foxgrover, A. C., Hein, J. R., and Swarzenski, P. W., 2013, A Sr–Nd isotopic study of sand-sized sediment provenance and transport for the San Francisco Bay coastal system: Marine Geology, v. 345, p. 143–153, https://doi.org/10.1016/j.margeo.2013.01.002
Ross, G. M., Parrish, R. R., and Winston, D., 1992, Provenance and U-Pb geochronology of the Mesoproterozoic Belt Supergroup (northwestern Unites States): Implications for age of deposition and pre-Panthalassa plate reconstructions: Earth and Planetary Science Letters, v. 113, n. 1–2, p. 57–76, https://doi.org/10.1016/0012-821X(92)90211-D
Ryan, K. M., and Williams, D. M., 2007, Testing the reliability of discrimination diagrams for determining the tectonic depositional environment of ancient sedimentary basins: Chemical Geology, v. 242, n. 1–2, p. 103–125, https://doi.org/10.1016/j.chemgeo.2007.03.013
Sack, P. J., Berry, R. F., Meffre, S., Falloon, T. J., Gemmell, J. B., and Friedman, R. M., 2011, *In situ* location and U-Pb dating of small zircon grains in igneous rocks using laser ablation–inductively coupled plasma–quadrupole mass spectrometry: Geochemistry, Geophysics, Geosystems, v. 12, n. 5, https://doi.org/10.1029/2010GC003405
Saleeby, J., Le Pourhiet, L., Saleeby, Z., and Gurnis, M., 2012, Epeirogenic transients related to mantle lithosphere removal in the southern Sierra Nevada region, California, part I: Implications of thermomechanical modeling: Geosphere, v. 8, n. 6, p. 1286–1309, https://doi.org/10.1130/GES00746.1
Saleeby, J., Saleeby, Z., and Le Pourhiet, L., 2013, Epeirogenic transients related to mantle lithosphere removal in the southern Sierra Nevada region, California: Part II. Implications of rock uplift and basin subsidence relations: Geosphere, v. 9, n. 3, p. 394–425, https://doi.org/10.1130/GES00816.1
Sarna-Wojcicki, A. M., Meyer, C. E., Bowman, H. R., Hall, N. T., Russell, P. C., Woodward, M. J., and Slate, J. L., 1985, Correlation of the Rockland ash bed, a 400,000-year-old stratigraphic marker in northern California and western Nevada, and implications for middle Pleistocene paleogeography of central California: Quaternary Research, v. 23, n. 2, p. 236–257 https://doi.org/10.1016/0033-5894(85)90031-6
Saylor, J. E., and Sundell, K. E., 2016, Quantifying comparison of large detrital geochronology data sets: Geosphere, v. 12, n. 1, p. 203–220, https://doi.org/10.1130/GES01237.1
Schoellhamer, D. H, Wright, S. A., and Drexler, J., 2012, A Conceptual Model of Sedimentation in the Sacramento–San Joaquin Delta: San Francisco Estuary and Watershed Science, 10(3). Retrieved from https://escholarship.org/uc/item/2652z8sq
Schweickert, R. A., and Cowan, D. S., 1975, Early Mesozoic tectonic evolution of the western Sierra Nevada, California: GSA Bulletin, v. 86, n. 10, p. 1329–1336, https://doi.org/10.1130/0016-7606(1975)86<1329:EMTEOT>2.0.CO;2
Sharman, G. R., and Johnstone, S. A., 2017, Sediment unmixing using detrital geochronology: Earth and Planetary Science Letters, v. 477, p. 183–194, https://doi.org/10.1016/j.epsl.2017.07.044
Sharman, G. R., Graham, S. A., Grove, M., and Hourigan, J. K., 2013, A reappraisal of the early slip history of the San Andreas Fault, central California, USA.: Geology, v. 41, n. 7, p. 727–730, https://doi.org/10.1130/G34214.1
Sharman, G. R., Graham, S. A., Grove, M., Kimbrough, D. L., and Wright, J. E., 2015, Detrital zircon provenance of the Late Cretaceous–Eocene California forearc: Influence of Laramide low-angle subduction on sediment dispersal and paleogeography: GSA Bulletin, v. 127, n. 1–2, p. 38–60, https://doi.org/10.1130/B31065.1
Sharman, G. R., Sharman, J. P., and Sylvester, Z., 2018, detritalPy: A Python-based toolset for visualizing and analysing detrital geo-thermochronologic data: The Depositional Record, v. 4, n. 2, p. 202–215, https://doi.org/10.1002/dep2.45
Shervais, J. W., and Kimbrough, D. L., 1985, Geochemical evidence for the tectonic setting of the Coast

Range ophiolite: A composite island-arc–oceanic crust terrane in western California: Geology, v. 13, n. 1, p. 35–38, https://doi.org/10.1130/0091-7613(1985)13<35:GEFTTS>2.0.CO;2
Sircombe, K. N., and Freeman, M. J., 1999, Provenance of detrital zircons on the Western Australia coastline –Implications for the geologic history of the Perth basin and denudation of the Yilgarn: Geology, v. 27, n. 10, p. 879–882, https://doi.org/10.1130/0091-7613(1999)027<0879:PODZOT>2.3.CO;2
Sláma, J., and Košler, J., 2012, Effects of sampling and mineral separation on accuracy of detrital zircon studies: Geochemistry, Geophysics, Geosystems, v. 13, n. 5, 17 p., https://doi.org/10.1029/2012GC004106
Smith, N. D., and Pérez-Arlucea, M., 2008, Natural levee deposition during the 2005 flood of the Saskatchewan River: Geomorphology, v. 101, n. 4, p. 583–594, https://doi.org/10.1016/j.geomorph.2008.02.009
Snow, C. A., Wakabayashi, J., Ernst, W. G., and Wooden, J. L., 2010, Detrital zircon evidence for progressive underthrusting in Franciscan metagraywackes, west-central California: GSA Bulletin, v. 122, n. 1–2, p. 282–291, https://doi.org/10.1130/B26399.1
Somme, T. O., Helland-Hansen, W., Martinsenw, O. J., and Thurmondw, J. B., 2009, Relationships between morphological and sedimentological parameters in source-to-sink systems: A basis for predicting semi-quantitative characteristics in subsurface systems: Basin Research, v. 21, n. 4, p. 361–387, https://doi.org/10.1111/j.1365-2117.2009.00397.x
Spencer, C. J., Kirkland, C. L., and Roberts, N. M. W., 2018, Implications of erosion and bedrock composition on zircon fertility: Examples from South America and Western Australia: Terra Nova, v. 30, n. 4, p. 289–295, https://doi.org/10.1111/ter.12338
Stacey, J. S., and Kramers, J. D., 1975, Approximation of terrestrial lead isotope evolution by a two-stage model: Earth and Planetary Science Letters, v. 26, n. 2, p. 207–221, https://doi.org/10.1016/0012-821X(75)90088-6
Sundell, K. E., and Saylor, J. E., 2017, Unmixing detrital geochronology age distributions: Geochemistry, Geophysics, Geosystems, v. 18, n. 8, p. 2872–2886, https://doi.org/10.1002/2016GC006774
Surpless, K. D., 2014, Geochemistry of the Great Valley Group: An integrated provenance record: International Geology Review, v. 57, n. 5–8, p. 747–766, https://doi.org/10.1080/00206814.2014.923347
Surpless, K. D., and Augsburger, G. A., 2009, Provenance of the Pythian Cave conglomerate, northern California: Implications for mid-Cretaceous paleogeography of the U.S. Cordillera: Cretaceous Research, v. 30, n. 5, p. 1181–1192, https://doi.org/10.1016/j.cretres.2009.05.005
Surpless, K. D., Graham, S. A., Covault, J. A., and Wooden, J. L., 2006, Does the Great Valley Group contain Jurassic strata? Reevaluation of the age and early evolution of a classic forearc basin: Geology, v. 34, n. 1, p. 21–24, https://doi.org/10.1130/G21940.1
Taylor, S. R., and McLennan, S. M., 1985, The Continental Crust: Its Composition and Evolution: Boston, Massachusetts, Blackwell Scientific, 312 p.
——— 1995, The geochemical evolution of the continental crust: Reviews of Geophysics, v. 33, n. 2, p. 241–265, https://doi.org/10.1029/95RG00262
Taylor, S. R., and White, A. J. R., 1966, Trace element abundances in andesites: Bulletin Volcanologique, v. 29, n. 1, p. 177–194, https://doi.org/10.1007/BF02597152
Unruh, J. R., Dumitru, T. A., and Sawyer, T. L., 2007, Coupling of early Tertiary extension in the Great Valley forearc basin with blueschist exhumation in the underlying Franciscan accretionary wedge at Mount Diablo, California: GSA Bulletin, v. 119, n. 11–12, p. 1347–1367, https://doi.org/10.1130/B26057.1
VanderPlas, J., 2016, Python data science handbook: essential tools for working with data: " O'Reilly Media, Inc."
Vermeesch, P., 2012, On the visualisation of detrital age distributions: Chemical Geology, v. 312–313, p. 190–194, https://doi.org/10.1016/j.chemgeo.2012.04.021
Wakabayashi, J., 2015, Anatomy of a subduction complex: Architecture of the Franciscan Complex, California, at multiple length and time scales: International Geology Review, v. 57, n. 5–8, p. 669–746, https://doi.org/10.1080/00206814.2014.998728
Walker, J. D., Martin, M. W., and Glazner, A. F., 2002, Late Paleozoic to Mesozoic development of the Mojave Desert and environs, California, *in* Glazner, A. F., Walker, J. D., and Bartley, J. M., editors, Geologic Evolution of the Mojave Desert and Southwestern Basin and Range: Geological Society of America Memoir 195, p. 1–18, https://doi.org/10.1130/0-8137-1195-9.1
Wallin, E. T., and Metcalf, R. V., 1998, Supra-subduction zone ophiolite formed in an extensional forearc: Trinity terrane, Klamath Mountains, California: The Journal of Geology, v. 106, n. 5, p. 591–608, https://doi.org/10.1086/516044
Whetten, J. T., Kelley, J. C., and Hanson, L. G., 1969, Characteristics of Columbia River sediment and sediment transport: Journal of Sedimentary Petrology, v. 39, n. 3, p. 1149–1166.
Whitmore, G. P., Crook, K. A. W., and Johnson, D. P., 2004, Grain size control of mineralogy and geochemistry in modern river sediment, New Guinea collision, Papua New Guinea: Sedimentary Geology, v. 171, n. 1–4, p. 129–157, https://doi.org/10.1016/j.sedgeo.2004.03.011
Wong, F. L., Woodrow, D. L., and McGann, M., 2013, Heavy mineral analysis for assessing the provenance of sandy sediment in the San Francisco Bay Coastal System: Marine Geology, v. 345, p. 170–180, https://doi.org/10.1016/j.margeo.2013.05.012
Wong, M., and Parker, G., 2006, Reanalysis and correction of bed-load relation of Meyer-Peter and Müller using their own database: Journal of Hydraulic Engineering, v. 132, n. 11, p. 1159–1168, https://doi.org/10.1061/(ASCE)0733-9429(2006)132:11(1159)
Wright, J. E., and Fahan, M. R., 1988, An expanded view of Jurassic orogenesis in the western United States Cordillera: Middle Jurassic (pre-Nevadan) regional metamorphism and thrust faulting within an active arc environment, Klamath Mountains, California: GSA Bulletin, v. 100, n. 6, p. 859–876, https://doi.org/10.1130/0016-7606(1988)100<0859:AEVOJO>2.3.CO;2

Wright, J. E., and Wyld, S. J., 1994, The Rattlesnake Creek terrane, Klamath Mountains, California: An early Mesozoic volcanic arc and its basement of tectonically disrupted oceanic crust: GSA Bulletin, v. 106, n. 8, p. 1033–1056, https://doi.org/10.1130/0016-7606(1994)106<1033:TRCTKM>2.3.CO;2

——— 2007, Alternative tectonic model for Late Jurassic through Early Cretaceous evolution of the Great Valley Group, California, *in* Cloos, M., Carlson, W. D., Gilbert, M. C., Liou, J. G., and Sorenson, S. S., editors, Convergent margin terranes and associated regions: A tribute to W. G. Ernst: GSA Special Papers, v. 419, p. 81–95, https://doi.org/10.1130/2007.2419(04)

Wright, S. A., and Schoellhamer, D. H., 2004, Trends in the sediment yield of the Sacramento River, California, 1957–2001: San Francisco Estuary and Watershed Science, v. 2, n. 2, 14 p., https://doi.org/10.15447/sfews.2004v2iss2art2

——— 2005, Estimating sediment budgets at the interface between rivers and estuaries with application to the Sacramento–San Joaquin River Delta: Water Resources Research, v. 41, n. 9, (W09428), https://doi.org/10.1029/2004WR003753

Wronkiewicz, D. J., and Condie, K. C., 1987, Geochemistry of Archean shales from the Witwatersrand Supergroup, South Africa: Source-area weathering and provenance: Geochimica et Cosmochimica Acta, v. 51, n. 9, p. 2401–2416, https://doi.org/10.1016/0016-7037(87)90293-6

——— 1990, Geochemistry and mineralogy of sediments from the Ventersdorp and Transvaal Supergroups, South Africa: Cratonic evolution during the early Proterozoic: Geochimica et Cosmochimica Acta, v. 54, n. 2, p. 343–354, https://doi.org/10.1016/0016-7037(90)90323-D

Xiao, S., and Grove, M., 2012, Detrital Zircon evaluation of the provenance shift in the Pleistocene Merced Formation, San Francisco: Implications for the timescales of sedimentary processes. Abstract ED31A-0706 presented at 2012 Fall Meeting, AGU, San Francisco, California, 3–7 December.

Xu, J., Stockli, D. F., and Snedden, J. W., 2017, Enhanced provenance interpretation using combined U-Pb and (U-Th)/He double dating of detrital zircon grains from lower Miocene strata, proximal Gulf of Mexico Basin, North America: Earth and Planetary Science Letters, v. 475, p. 44–57. https://doi.org/10.1016/j.epsl.2017.07.024

Zhang, J. Y., Yin, A., Liu, W. C., Wu, F. Y., Lin, D., and Grove, M., 2012, Coupled U-Pb dating and Hf isotopic analysis of detrital zircon of modern river sand from the Yalu River (Yarlung Tsangpo) drainage system in southern Tibet: Constraints on the transport processes and evolution of Himalayan rivers: GSA Bulletin, v. 124, p. 1449–1473, https://doi.org/10.1130/B30592.1